Fundamental investigations on stress engineering of sputtered hard coatings

Dipl.-Ing. Harald Köstenbauer

being a thesis in partial fulfilment of the requirements for the degree of a

Doctor of Montanistic Sciences (Dr.mont.)

at the University of Leoben

Leoben, March 2008

This thesis was supported by the Austrian NANO Initiative via a grant from the Austrian Science Fund FWF within the project “Stress Design” (N401-NAN).

Affidavit

I declare in lieu of oath, that I wrote this thesis and performed the associated research myself, using only literature cited in this volume.

Leoben, March 2008

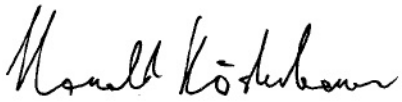

Harald Köstenbauer

Acknowledgements

My sincerest gratitude is due to my supervisor Christian Mitterer, head of the Thin Films Group at the Department of Physical Metallurgy and Materials Testing, and to Jozef Keckes leader of the “Stress Design” Project giving me the opportunity to carry out this work and for their guidance and support.

I am very grateful to my scientific supervisor and friend Gerardo Fontalvo for his advice and all the insightful discussions during and besides the work.

Furthermore, I would like to thank Christian Teichert, Gregor Hlawacek and Thomas Klünsner for their contribution to this work.

Special thanks to my diploma student Anna Hofer for her work being a part of this thesis. I am also very grateful to all the people of the Thin Films Group and of the Department of Physical Metallurgy and Materials Testing as well as all fellow students of materials science from the year 1998.

I would like to express my sincere gratitude to my office mates Nazanin, Martin and Thomas for the pleasant atmosphere and all the fun we had during the last years.

Content

1 Introduction 1

2 Coating synthesis 3

2.1 General 3

2.2 Magnetron Sputtering 4

2.3 Structure evolution during film growth 7

3 Stresses in thin films 13

3.1 Origins of film stress 13

3.2 Growth stress in polycrystalline films 13

3.2.1 Non-energetic particle deposition 13

3.2.2 Stress generation in sputtering deposition 15

3.3 Stress characterisation 17

3.3.1 Substrate curvature 17

3.3.2 The $\sin^2 \psi$ method 19

4 Thermally activated processes 21

4.1 Diffusion 21

4.2 Recovery and stress relaxation 22

4.3 Recrystallization and grain coarsening 23

5 Material selection and design 25

6 Coating characterisation 31

6.1 Atomic force- and scanning electron microscopy 31

6.2 Transmission electron microscopy 32

6.3 X-ray diffraction 33

6.4 Biaxial stress-temperature measurement 34

6.5 Nanoindentation 36

6.6 Tribology 36

7 Summary and conclusions 39

8 References 43

9 Publications 49

9.1 List of included papers 49

9.2 Publications related to this thesis 49

9.3 My contribution to the included papers 50

Paper I 51

Paper II 61

Paper III 72

Paper IV 85

Paper V 102

1 Introduction

Surface engineering, or more general interfacial engineering, has become one of the most important technologies to affect a demonstrable improvement in lifetime and performance of many components. This embraces all interfaces in materials such as grain or phase boundaries and the conjunction of the material to the environment, the surface. Thus, interfacial engineering gives rise to enhanced material properties of both the bulk material with e.g. increased toughness and strength as well as the surface coating with e.g. high hardness, corrosion and wear resistance by applying such important discoveries like the size effects in materials [1]. Due to surface modification techniques, the lifetime of components or tools could be increased by a factor of more than 10 for certain applications. The most commonly used techniques in industry to deposit coatings on tools are chemical vapour deposition (CVD) and physical vapour deposition (PVD) where the coating is synthesized from a vapour phase on a substrate [2].

Nowadays, transition metal nitride coatings are widely used to improve lifetime and performance of tools. Due to their bond structure, a mixture of covalent, metallic and ionic components, this type of coatings show high hardness, chemical inertness, good electrical conductivity and excellent wear resistance. One of the first materials used in industry to coat tools, and hence, one of the best-known and investigated ones is titanium nitride (TiN). TiN with its face-centered cubic structure was, and still is, the base for further development of advanced coatings such as (Ti,Al)N [3]. Another possibility to improve coating properties apart from alloying is the combination of different materials in the coating using several ways such as multilayer arrangements [4] or nanocomposites [5]. In both cases, different goals like very high hardness and toughness or the combination of high wear resistance and low friction can be achieved.

The requirements on coated tools and components in industry are permanently increasing. A general trend for cutting tools goes towards higher cutting speeds and consequently higher temperatures. Also the working temperature of components is steadily increasing since it allows better performance, less pollution and energy losses. The performance of a coated surface is determined, among others, by its structure and residual stresses, particularly when it comes to thermal loads. Stresses and strains in the coating and the substrate due to mechanical and thermal loads are thus of interest to prevent failure. Residual stresses are composed of an intrinsic part resulting from growth defects and a

thermal part caused by the mismatch of the thermal expansion coefficients of the coating and the substrate [6]. For a further increase of lifetime, it is of major importance to understand how the structure of a coating, coating architecture and residual stresses might be influenced by thermal processes [7]. Then, it should be possible to increase the performance of protective coatings which are subjected to thermal cycles by designing coating architectures (multi-layers or nanocomposites) with optimized deposition parameters resulting in reduced mismatch of mechanical properties and thermal expansion.

The aim of this thesis was to investigate stresses and stress relaxation in several model systems. The starting point of this investigation was to study the influence of the coating thickness on stresses and stress relaxation in a single-phase transition metal nitride hard coating (TiN). Special emphasize was placed on the question how film structure is related to the resulting stress and stress relaxation behavior. Once having a basic understanding of the processes present in a single layer, model systems based upon a multilayer arrangement consisting of TiN and a soft metallic phase (Ag, Cu) were investigated. A soft metallic phase was chosen in order to obtain adequate differences in material properties for a more explicit determination of the influence on the system. In a last step, nitride-metal combinations were deposited as a nanocomposite to achieve a structure of increased complexity with less defined interfaces compared to the multilayer, and the results were elucidated on the basis of the findings from the less complex systems. Additionally to the main work dealing with the structure and the stresses of the model coatings, a few tribological tests were conducted on the Ag-alloyed nanocomposite coatings and correlations between structure and Ag content on the tribological respond of the coatings at room temperature as well as at elevated temperatures were determined.

2 Coating synthesis

2.1 General

A general classification system for deposition processes divides the processes into the three following categories: gaseous state processes like CVD and PVD, solution state processes like electrochemical deposition and molten or semi-molten state processes like thermal spraying. Two important characteristic parameters for the coating processes are the thickness of the coating that can be achieved and the deposition temperature. The typical range of coating thicknesses and deposition temperatures are 0.1 µm to 10 mm and room temperature up to ~1000°C, respectively [8,9]. By selecting a suitable deposition technique and process parameters, a wide range of coating properties can be realized [3].

The deposition of thin, hard, ceramic coatings is mainly based on CVD and PVD techniques [9,10]. The characteristic feature of CVD and PVD processes is the state of matter of the used material. In these processes, a solid reaction product nucleates and grows on a substrate. These reactions need an activation energy which is obtained by e.g. heat or plasma. CVD processes are working with materials in gaseous state which chemically react. Therefore, high activation energies, and consequently high temperatures (>900°C), are usually needed to grow hard coatings [10]. The main advantage of the CVD process is the possibility to coat components with complex geometry and various sizes. Limitations are e.g. the high deposition temperature that the substrates have to withstand or the types of possible reactions [11]. In PVD processes, one or more components are evaporated from a solid or liquid source. In contrast to CVD, the PVD processes are extremely versatile, enabling deposition of any metal, alloy or compound. The deposition temperatures can be low, and therefore, a wide range of substrate materials can be used [9,12,13].

The basic PVD processes can be distinguished in two general categories which differ in their vapour generation: evaporation and sputtering. Generally, all PVD processes contain the steps of evaporating a condensed phase, transport of the vapour to the substrate and finally the condensation on the substrate surface followed by film nucleation and growth. Usually, this process takes place in a vacuum chamber to ensure minimal collisions during the transport of the vaporized coating material and avoiding involuntary reactions. For deposition of compounds, which may be introduced as gases into the PVD chamber, a

reaction occurs between their components, mainly at the substrate surface. These processes are termed reactive [10,11]. For this work magnetron sputtering was used, thus it is described in detail in the following chapter.

2.2 Magnetron Sputtering

A fast particle of suitable kinetic energy, usually from an inert gas, e.g. an Ar ion, may eject an atom or cluster from the surface of the deposition material (target) by a momentum transfer process. The ignition of a plasma is necessary to provide ions for this momentum transfer. To initiate a glow discharge, an inert gas is inserted to the chamber with a typical working gas pressure between 0.2 and 1 Pa. If a voltage of several hundreds or thousand Volts is applied between target and substrate, a glow discharge will be established. The evaporated target material consists mainly of neutrals, only ~1% is ionized. An arrangement like this with the substrates or the chamber wall acting as anode is called diode system. Such systems can be powered by direct current (DC), where the target material has to be conductive, or by radio frequency (RF), which allows the deposition of non-conductive material [14, 15].

Applying magnetic fields to the target increases the efficiency of the ionisation close to the target with respect to the diode system. The applied magnetic field parallel to the cathode concentrates the electrons near the target, minimising the loss of energy (Figure 2.1a). They collide mostly with gas atoms, hence the ionisation efficiency is increased. The increased ion density results in higher ion current and higher sputtering rate. The magnetic field has a low strength, and thus it only influences the electrons but not the ions [10,16].

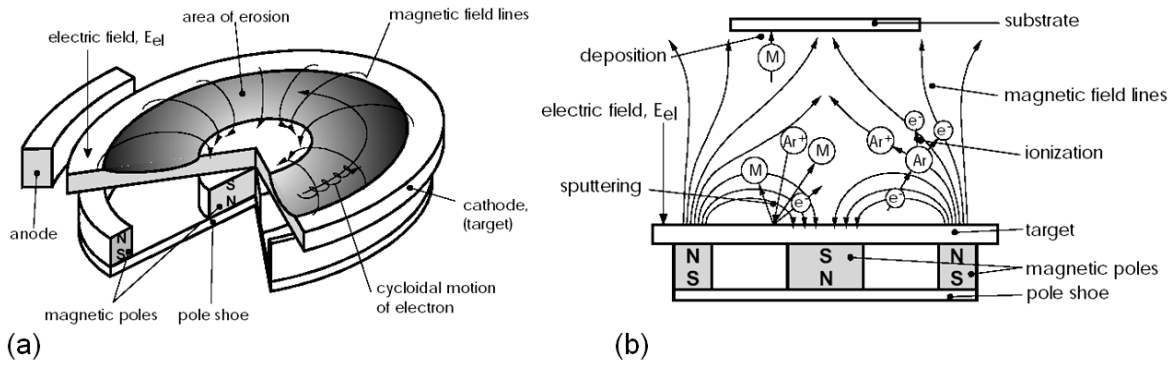

Figure 2.1: Planar magnetron configuration (a) balanced magnetron, (b) unbalanced magnetron (modified by [20] after [18]).

The applied magnetic field, and consequently the ion concentration, result in non uniform erosion of the target and the formation of the so called “race track” (Figure 2.1a). In an idealized situation, all of the magnetic field lines loop between the outer and inner magnets of the planar magnetron configuration. These types of magnetrons are called conventional balanced magnetrons (CBM) as shown in Figure 2.1a. Consequently, the bombardment of the growing film at the distant substrate by energetic particles is minimal [17]. Nevertheless, ion bombardment during film growth is a suitable tool for improving several coating properties. For such purposes, Window and Savvides [17] developed a new magnetron system based upon an unbalanced magnetic arrangement which can be obtained by a stronger central or stronger outer magnet (Figure 2.1b). Such magnetrons are called unbalanced magnetrons (UBM`s). The main advantage is that this new planar magnetron additionally provides an ion flux to the growing film. The intensity of this ion flux can be adjusted by changing the magnetic field configuration of the magnetrons [17-19]. The energy of the ion flux can be adjusted by varying the magnetic field or by a potential applied to the substrate called bias voltage [21].

In this work, non-reactive and reactive magnetron sputtering with N_2 as reactive gas was used. TiN films (paper I) of different thicknesses were deposited onto silicon (100) substrates by reactive sputtering from a Ti target (∅ 75×6 mm^3) in an Ar+N_2 atmosphere using the laboratory-scale unbalanced DC magnetron sputtering system shown in Figure 2.2 [22]. There, the substrates are stationary positioned in a distance of about 6 cm above the target. The substrate temperature and the total pressure were 550°C and 0.25 Pa, respectively. To influence the residual stresses in the as-deposited state, different negative bias voltages were used.

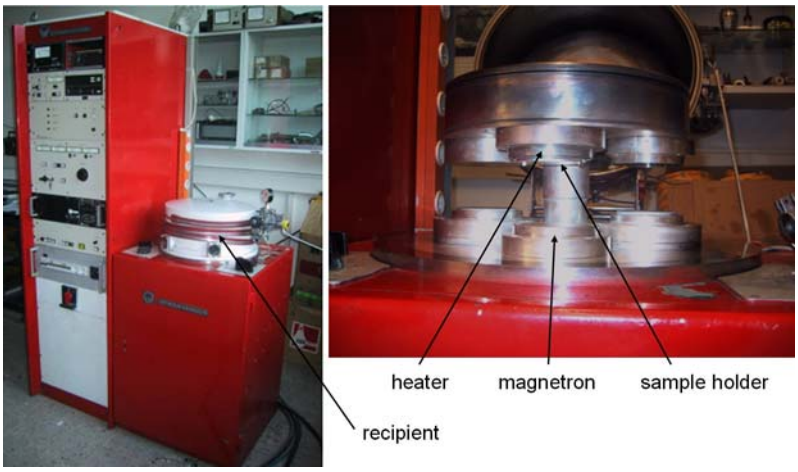

Figure 2.2: Modified sputtering system Leybold Z400.

TiN/Me (Me=Ag, Cu) multilayer films (paper II+V) were deposited onto Si (100) and austenitic stainless steel substrates. The total thickness of the multilayers was kept constant, while the bilayer thickness Λ was varied with the ratio of Me to TiN layer thickness held constant. The layers were deposited by unbalanced DC magnetron sputtering from one Me and two Ti targets (∅ 50.8×6.35 mm^3) (see Figure 2.3(c)) by sputtering in Ar in case of Me and reactive sputtering in Ar+N_2 in case of TiN. The substrates were positioned parallel to the targets in a distance of 7 cm and rotated during deposition (Figure 2.3(b)). The substrate temperature and the total pressure were 150°C and 0.25 Pa in case of the TiN/Ag coatings and 550 °C and 0.25 Pa in case of the TiN/Cu coatings, respectively. TiN/Ag coatings were deposited at floating potential, whereas for the TiN/Cu coatings a bias voltage of -80 V was used.

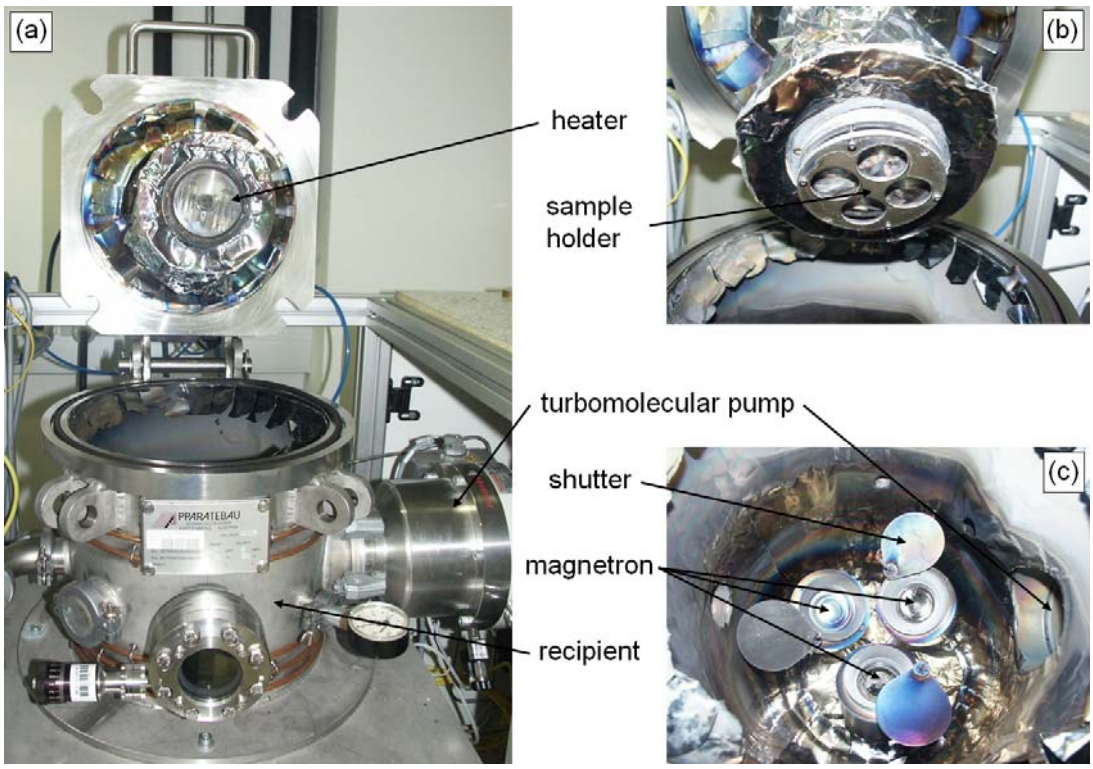

Figure 2.3: Laboratory scale high-vacuum sputtering system with rotating sample holder (b) and three magnetron cluster flange (c).

TiN/Me nanocomposite films (paper III-V) were deposited onto Si (100) and high-speed steel substrates. The layers were deposited by reactive unbalanced DC magnetron co-sputtering in an Ar+N_2 atmosphere from one Me and two Ti targets using the sputtering system shown in Figure 2.3. The Me content in the film was varied by changing the

sputtering power at the Me target. Six different Me target power settings were chosen to deposit films with different Me content. To improve adhesion, a 50 nm thick TiN interlayer was deposited directly after substrate etching. The same substrate temperatures and total pressure like for the multilayer coatings were used. TiN/Ag nanocomposite coatings were deposited at floating potential, whereas for the TiN/Cu nanocomposite coatings a bias voltage of -50 V was used.

2.3 Structure evolution during film growth

The properties of coatings prepared by the condensation from the vapour phase may be completely different to those of their bulk material. In this regard, the structure and properties of coatings are determined by the phenomena occurring during nucleation and film growth.

In general, the substrate has a different chemical nature than the coating material. Thus, deposition atoms can not immediately condense at the substrate surface [23]. The fundamental reactions occurring at the substrate surface are schematically shown in Figure 2.4.

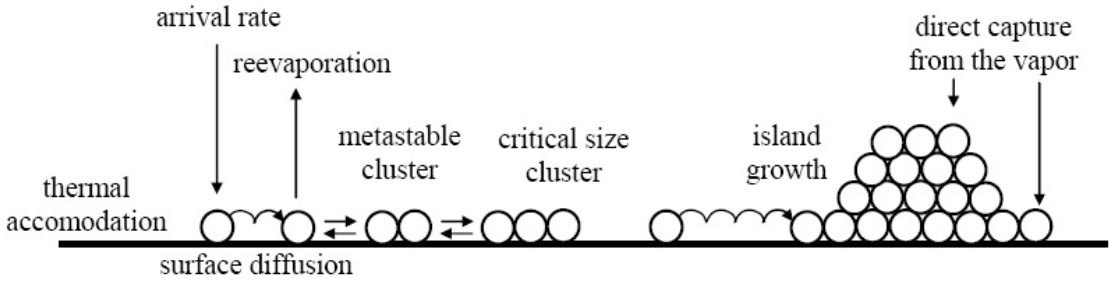

Figure 2.4: Schematic representation of processes leading to three-dimensional nucleation and film growth [24,25].

Atoms from the gas phase are impinging on the surface with a specific arrival rate, and they can be adsorbed or directly reflected. On the surface they can diffuse a certain distance and interact with other atoms or desorb again (re-evaporation). For very small impingement rates, an equilibrium between adsorption and desorption can be established, characterized by such a small coverage that no nucleation can take place. High impingement rates can cause the formation of metastable and stable clusters, which can grow by binding of diffusing atoms or by a direct capture of atoms from the vapour [24,25]. The incorporated atoms readjust their positions within the lattice by bulk diffusion

processes. Larger clusters may grow in expense of neighbouring smaller clusters by Ostwald ripening. When clusters meet, either by growth or by motion, they combine. This coalescence continues and forms a network of connected clusters. Next, the remaining voids are filled and eventually a film with full coverage is formed [26].

Three basic types of film growth take place as schematically illustrated in Figure 2.5. Two-dimensional layer-by-layer growth (Frank-Van der Merwe) occurs when the binding between adatoms at the surface is equal to or less than that between film atoms and substrate (Figure 2.5(a)). During three-dimensional island growth (Volmer-Weber), small clusters are nucleated directly at the substrate surface. They grow into islands which in turn coalesce to form a continuous film (Figure 2.5(b)). In this case the film atoms are more strongly bound to each other than to the substrate surface. The combination of the first two growth modes results in combined layer + island growth (Stranski-Krastanow) (Figure 2.5(c)). In this case, after forming one to several monolayers, layer-by-layer growth becomes unfavourable and islands are formed. The transition from layer to island growth is not completely understood, but can be driven by the release of elastic energy stored in the film due to film/substrate lattice mismatch [24].

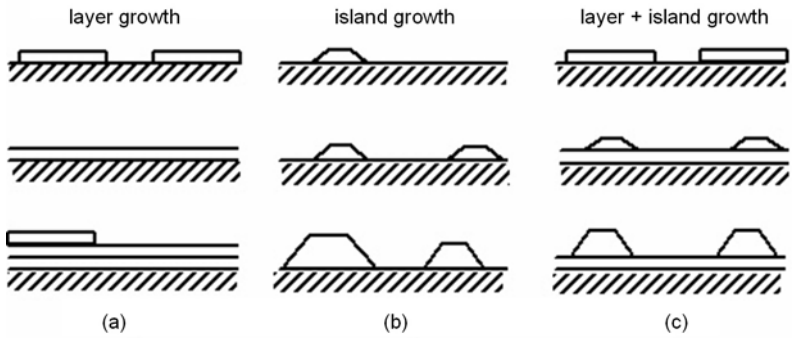

Figure 2.5: Schematic representation of three modes of film growth on substrates (a) layer growth, (b) island growth, (c) layer + island growth [24,25,27].

Which growth mode prevails, depends mainly on the affinity of the film material to the substrate, the activation energy of diffusion and the binding energies between the film atoms and between the film and the substrate [25,26].

When the films grow thicker, they develop a structure which may depend on nucleation and/or growth kinetics. Thus, structure zone models (SZM) were established. The

phenomenological description correlates the structure with the physical processes and deposition parameters.

Generally, nucleation and growth of coatings involves several basic processes such as shadowing, desorption, surface diffusion, bulk diffusion and recrystallization. Shadowing results from a geometric interaction between the roughness of the growing surface and the angular directions of the arriving coating atoms [28]. These processes can be quantified in terms of the characteristic roughness of the coating surface, the activation energies for surface and bulk diffusion, and the sublimation energy. For many pure metals, these energies are related and proportional to the melting point (T_m). Thus, many of the basic processes can be expected to dominate over different ranges of the substrate temperature (T_s). Therefore, the homologous temperature (T_s/T_m) is the basis of several SZM`s.

First Movchan and Demchisin [29] defined three structure zones in evaporated films depending on the homologous temperature. At low temperatures ($T_s/T_m<0.3$), a porous structure of free-standing columnar crystals is formed (Zone 1). Such a structure is caused by the shadowing effect when the surface diffusion is negligible. At higher temperatures, diffusing atoms can fill the voids and a dense structure consisting of columnar grains is formed (Zone 2). At very high temperatures ($T_s/T_m>0.45$) recrystallization processes can occur already during the film deposition and a dense coarse grained structure is observed (Zone 3).

The Movchan-Demchisin model was modified by Thornton [30] considering the sputtering atmosphere as additional parameter (Figure 2.6a). Thornton introduced a new zone (Zone T), consisting of densely packed fibrous grains, between Zone 1 and Zone 2 (see Figure 2.6a). The adsorption of impurities from the sputtering atmosphere seems to reduce the surface mobility of adatoms, hence, the structure zones are shifted to higher temperatures. Intense ion bombardment during deposition, e.g. bias sputtering, strongly reduces the development of the open structure of Zone 1. Thornton`s model was modified by Messier et al. in order to show the influence of the energy of the incidence ions [31]. The transition zone T is widened to lower temperatures at the expense of Zone 1 which is caused by an ion bombardment induced mobility of the surface atoms (Figure 2.6b).

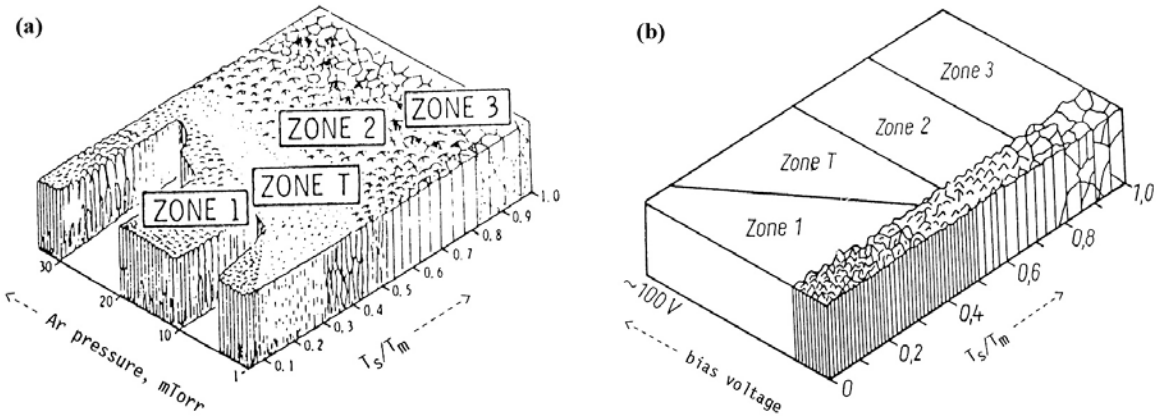

Figure 2.6: (a) Structure zone model (SZM) after Thornton [30], (b) modified SZM by ion assisted vapour deposition after Messier et al. [31].

The different SZM`s are based on various conditions such as the impingement rate and the substrate temperature. Generally, the growth of coatings starts at discrete nuclei. Figure 2.7a shows the case of zero surface diffusion and a unity condensation coefficient (every atom sticks where it lands). Since no crystal surface discrimination exists, the initial nuclei are spherical. The coating flux is normal, with some side scattering, resulting in the formation of a dense columnar structure which corresponds to Zone T. The coating exhibits a relatively smooth surface [28].

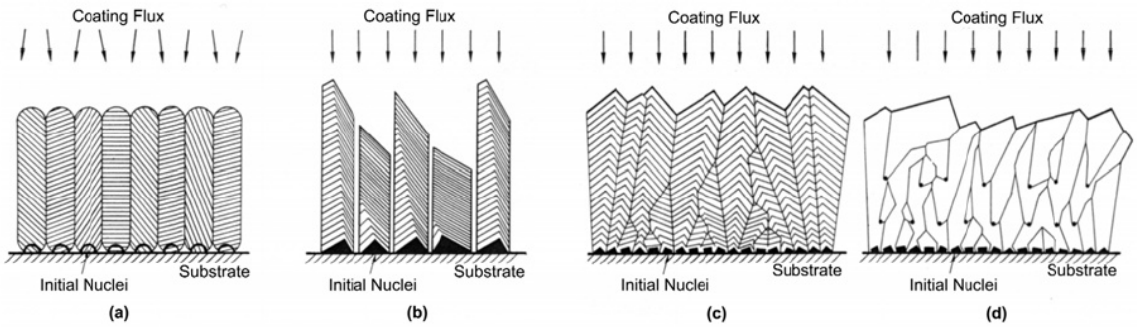

Figure 2.7: Two-dimensional growth structures for several extreme cases of adatom surface diffusion. (a) Zero surface diffusion, unity condensation coefficient. (b) Zero surface diffusion, condensation coefficient dependent on crystallographic surface. (c) Infinite surface diffusion. (d) Infinite surface diffusion with periodic renucleation [28].

Figure 2.7b shows the case of zero diffusion on crystal surfaces having different surface energies and condensation coefficients. As the coating flux is normal, the resulting

structure is open and relatively rough which corresponds to Zone 1. If the temperature is increased, the surface diffusion redistributes the coating flux and removes any dependence on the condensation coefficient. The growth rate is assumed to be the same on all crystal planes. Dense structures with a relatively smooth but facetted surface are formed which corresponds to Zone 2 (Figure 2.7c). If repeated nucleation occurs, a structure corresponding to Figure 2.7d is observed [25,28]. Grovenor et al. [32] studied the dependence of this structure on the homologous temperature. For $T_s/T_m<0.2$ the grains are small and equiaxed. The effect of a recurrent nucleation, which is necessary for the formation of equiaxed grains, is highly valid for the deposition of multi-component coatings [33]. Depending on the amount of the impurity, the different zones in the SZM belong to different temperatures. The higher the impurity concentration is, the less changes of the zones due to diffusion processes take place. Thus, Zone 1 is widened to higher temperatures at the expense of Zone T and Zone 2 [33].

Ion bombardment during film growth at low temperatures, e.g. bias sputtering, is a useful tool to increase the density and to modify the morphology of the films [34]. The effects of impinging energetic ions with a solid are illustrated schematically in Figure 2.8a, and possible generated lattice defects are shown in Figure 2.8b.

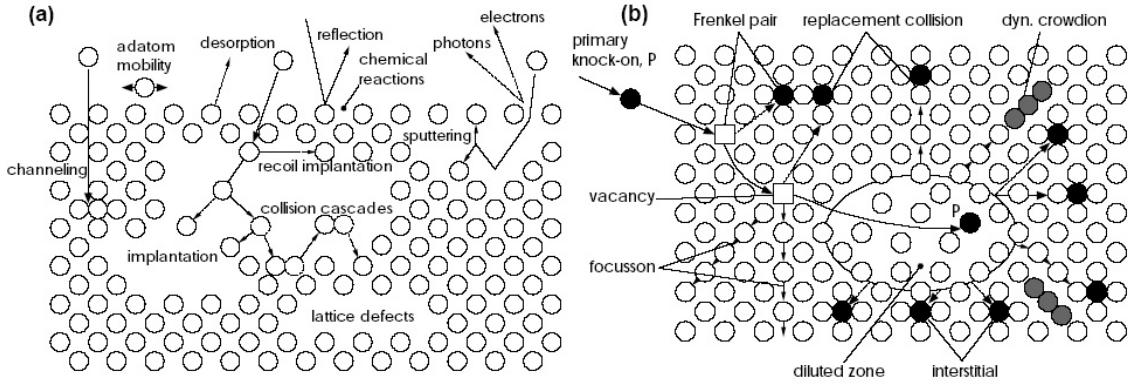

Figure 2.8: (a) Effects of an ion bombardment on a growing film [26,34]. (b) Schematic view of possible lattice defects by an impinging energetic atom, primary knock on atom (P) [35].

When the incoming ions or knock-on atoms possess enough kinetic energy, they will knock atoms out of their lattice position and develop, due to secondary collisions, a collision cascade (Figure 2.8a). The primary knocked atom absorbs most of the energy.

The resulting strong atomic motion along the trajectory of the ions leads to a rearrangement of the lattice [26]. As the energy of the impinging ions increases, atomic displacement produced in the collision cascade result in an increasing number of interstitials and vacancies (Figure 2.8b). In addition to defect generation, ion bombardment during growth influences adatom mobility and, hence, the defect density and the crystallographic orientation, too [24,26]. If a deposited film is bombarded during deposition by energetic gaseous particles, they may be incorporated into the growing film. The incorporated gas content depends on the particle energy, substrate temperature, film material and bombarding species [34].

3 Stresses in thin films

3.1 Origins of film stress

In general, residual stresses refer to the internal stress distribution present in a material system when all external boundaries of the system are free of applied traction. Virtually any thin film bonded to a substrate supports some state of residual stress. The presence of residual stress implies that, if the film would be relieved of the constraint of the substrate, it would change its in-plane dimension and/or would become curved. Some residual stress distribution will remain under these conditions, if the internal strain distribution is incompatible to a stress free state [36].

Film stresses are usually divided into two categories: growth stresses also commonly called intrinsic stresses and externally induced stresses called extrinsic stresses. Growth stresses are strongly dependent on the materials involved, the substrate temperature during deposition, the growth flux and the growth chamber conditions. Usually, growth stresses are reproducible for a given process and persist at room temperature for a long time following growth [36,37].

3.2 Growth stress in polycrystalline films

3.2.1 Non-energetic particle deposition

For many film-substrate material combinations, films grow in the Volmer-Weber mode. Following the initial nucleation of islands of film material, successive stages typically include: island growth, island-to-island contact and coalescence, large area contiguity and filling in of the remaining gaps to form a continuous film [36].

The evolution of volume-average film stress versus film thickness during steady deposition is schematically shown in Figure 3.1. First, the volume-average stress becomes compressive, then tensile and then compressive again. The compressive stress early in the deposition process, prior to island coalescence, is usually attributed to surface and/or interface stress. The lattice spacing in a very small isolated crystallite is smaller than the spacing in a bulk crystal of the same material. Crystallites forming on the growth surface become attached to the substrate resulting in a force action of the surface and the interface

stresses causing the compressive stress. Upon further growth of the islands, the internal strain in the crystallites tend to relax and consequently the compressive stresses decrease [6,36].

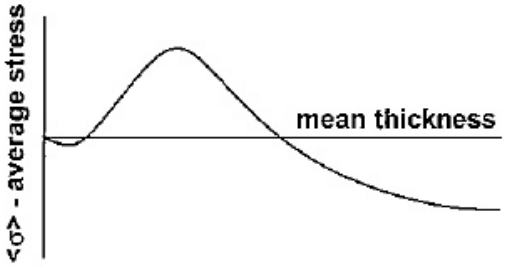

Figure 3.1: Schematic diagram of volume-average film stress versus mean film thickness during growth with a steady state deposition flux for high mobility materials [36].

The most widely adopted mechanistic model for the origin of tensile stress is that small gaps between adjacent grains could be closed by forming grain boundaries. The energy released through reduction in surface area could be converted to elastic deformation of the participating grains as a result of the deformation needed to close the gap. These strains consequently induce tensile stresses in the growing film [36,38]. It was shown that only across the regions where neighbouring columns are separated by less than 1.7 Å, the adhesive interaction between neighbouring surfaces can lead to a tensile strain in these columns [37]. Nix and Clemens [39] improved this model schematically shown in Figure 3.2. They imagined the island boundaries to be rounded surfaces. During growth each island makes contact at a single point to its adjacent islands. The coalescence process in this case is the reverse of the propagation of an elastic crack. The system can lower its net free energy by closing up this crack. In the course of "zipping up" the interface, the islands become strained elastically [6,36,39].

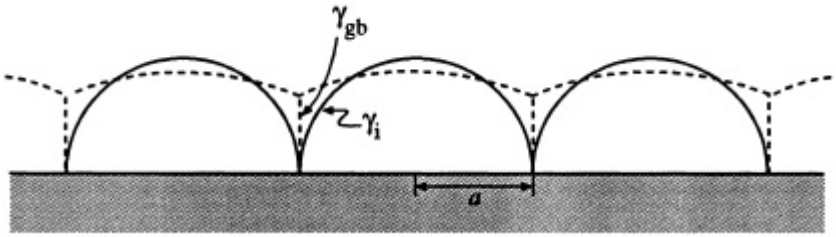

Figure 3.2: Illustration of the Nix-Hoffman mechanism for generating tensile stresses by coalescence of individually nucleated islands [6].

For high mobility materials, such as Cu or Ag, the average tensile stress in the film decreases until it becomes compressive again. The compressive average stress approaches a steady value for a fixed growth flux (Figure 3.1). If the growth is interrupted while the stress magnitude is at its plateau value, the stress magnitude falls off rapidly. Upon resumption of the deposition flux, the falloff is fully reversed [40]. Due to the fact that the stresses become compressive only in polycrystalline material, it can be deduced that the grain boundaries play an additional important role. It is assumed that the presence of a deposition flux and the presence of grain boundaries lead to an excess number of atoms comprising the film, thus causing compressive stresses. Spaepen [6] showed that only a small number of excess atoms is necessary to cause these compressive stresses. The driving force for introducing additional excess grain boundary atoms decreases with increasing compressive stress, leading eventually to a steady-state balance between these effects [36].

3.2.2 Stress generation in sputtering deposition

The deposition of thin films by sputtering processes leads predominantly to compressive stresses. Two features of importance are the relatively high kinetic energy of the arriving atoms at the surface and the inert gas atmosphere in the deposition chamber. Bombardment of the growing surface by energetic atoms can lead to the generation of excess interstitials in the near surface region as described in chapter 2.3. The amount of damage induced at the surface depends on both the energy of the arriving atoms and the background pressure of the inert gas [36,41].

Results of average film stress multiplied by film thickness are shown in Figure 3.3a. Large compressive stresses evolve in these materials at argon pressures typical for sputter deposition processes. It was found that the occurrence of compressive stresses correlates with the presence of entrapped argon in the film [36,41]. As seen in Figure 3.3a, low sputtering pressure leads to compressive stresses. The SZM [30] reveals that the formation of columnar grains is restricted at low gas pressures. Lower gas pressure during flight of the target atoms leads to less energy losses through collisions, and thus, to higher energy of arriving atoms. On this basis the “atomic-peening” or “ion-peening” process, first postulated by d`Heurle [42], which induces damage at the surface, is the primary cause of

compressive intrinsic stress during sputter deposition [25,36,43,44]. Argon entrapment is believed to contribute to the intrinsic stress build-up but it is not the principal mechanism.

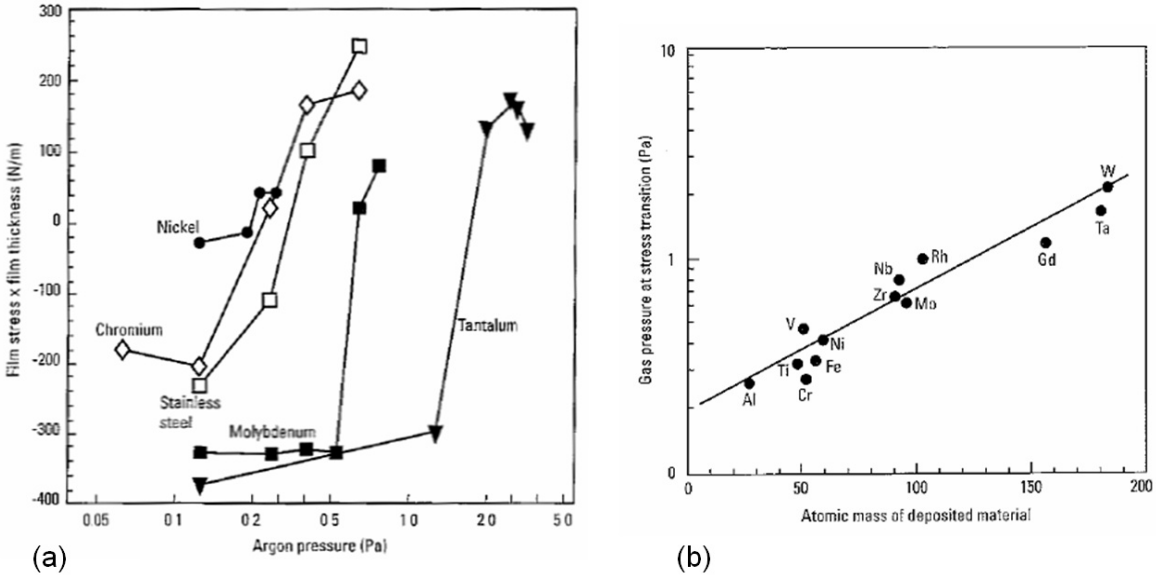

Figure 3.3: (a) Average internal stress versus argon pressure in sputter deposited films. (b) The variation of critical gas pressure at which the intrinsic stresses change from compressive to tensile, as a function of the atomic mass of the deposited material [36].

The inert gas pressure at which the transition from compressive to tensile intrinsic stresses occurs directly correlates with the atomic mass of the deposited material (Figure 3.3b). With increasing atomic mass, and thus momentum transfer, the gas pressure at which the stress changes is increased [36].

There are several additional mechanisms which can cause intrinsic stresses in the coating such as reduction in grain boundary area or texture evolution during growth which are of inferior interest for this work [36]. Another important mechanism is stress due to phase transformation [37] which can be neglected because the materials used in this work show no phase transformation in the investigated temperature region.

3.3 Stress characterisation

3.3.1 Substrate curvature

Stresses in a film attached to a flexible not too thick substrate will induce a bending of that substrate. These residual stresses consist of an intrinsic part, discussed in chapter 3.2, and extrinsic (thermal) stresses. As a result of the difference between the coefficient of thermal expansion of the coating and the substrate, the extrinsic stresses vary with temperature. When the coating-substrate composite cools down from deposition temperature to room temperature, the extrinsic stresses increase [45].

Figure 3.4 shows schematically a bended coating-substrate composite where l_x is the length, l_y the width and t_s and t_c the thickness of the substrate and the coating. The stress components are indicated by σ_{xx}, σ_{yy} and σ_{zz}.

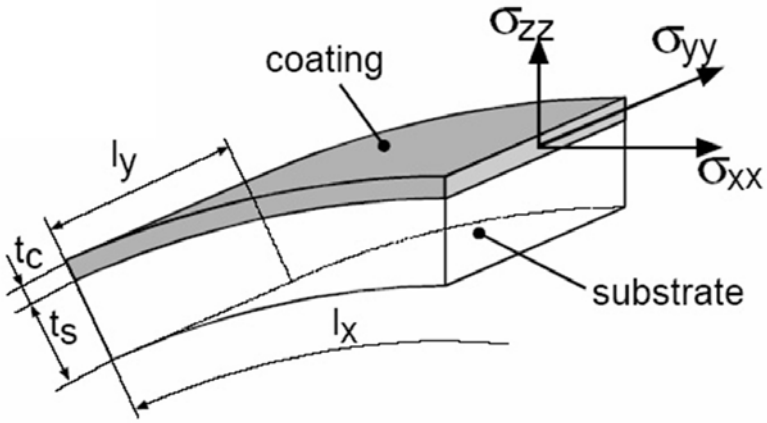

Figure 3.4: Schematic of a bended coating-substrate composite due to the residual stress [46] (modified by [20]).

If the coating is thin compared with the substrate, $t_c << t_s$, the mismatch strain ε^* is related to the curvature of the specimen κ as [47]:

$$\varepsilon^* = -\frac{1}{6} \cdot \frac{E_S \cdot (1-\nu_C)}{E_C \cdot (1-\nu_S)} \cdot \frac{t_S^{\,2}}{t_C} \cdot \kappa \qquad \textbf{(1)}$$

where E_s and ν_s are the Young`s modulus and the Poisson`s ratio of the substrate and E_c and ν_c are the Young`s modulus and the Poisson`s ratio of the coating.

For the plate geometry, the stress state is equi-biaxial (the normal stress σ_{zz} can be neglected), the specimen is deformed into spherical shape with the curvature $\kappa_x = \kappa_y = \kappa$, where κ_x is the curvature in x-direction and κ_y is the curvature in y-direction [47]. Expressing the strain by stress and elastic properties gives the frequently used modified Stoney formula [48], Eq. (2), which relates the curvature to the residual stress level in the thin coating, without knowing the elastic properties of the coating [49].

$$\sigma = \frac{1}{6} \cdot \left[\frac{E_S}{1-\nu_S} \right] \cdot \frac{t_S^{\,2}}{t_C} \cdot \frac{1}{R} \qquad \textbf{(2)}$$

In this equation, *1/R* is the curvature of the coating-substrate composite and σ denotes the biaxial stress.

For the used thin film approximation in Eq. (1) to be valid, t_c/t_s has to be small enough. A commonly used rule of thumb is that for approximately equal elastic properties the limit is $t_c/t_s < 1/100$. However, for cases $E_s<E_c$ an even smaller thickness ratio is needed [49]. The influence of the layer thickness ratio on the evolution of the curvature for different biaxial modulus ratios is shown in Figure 3.5. The figure illustrates the thickness ratios for which the thin film approximation, Eq. (1), can be applied [49].

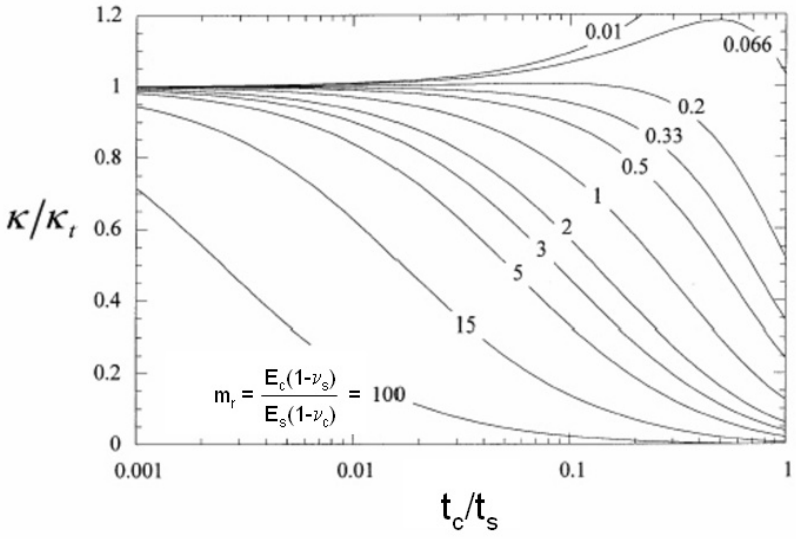

Figure 3.5: Normalised curvature as a function of thickness ratio for different biaxial moduli ratios. κ_t is the curvature obtained by the thin film approximation (modified after [49]).

3.3.2 The $\sin^2 \psi$ method

Another important method to characterize the stresses in a material is the so called $\sin^2\psi$ method. This method was not used within this work but should be described briefly due to its importance.

The orthogonal coordinate systems used are shown in Figure 3.6. The axes S_i define the surface of the specimen, with S_1 and S_2 in this surface. The laboratory system L_i is defined such that L_3 is in the direction of the normal to the family of planes (hkl) whose spacing is measured. L_2 is in the plane defined by S_1 and S_2 and makes an angle ϕ with S_2. Once the lattice spacing $d_{\phi\psi}$ is obtained from the position of the diffraction peak for a given reflection hkl, the strain along L_3 may be calculated by the use of the unstressed lattice spacing d_0. This strain may be expressed in terms of the strains in the sample coordinate system by a tensor transformation. Once the strains are obtained, the stresses in the S_i coordinate system may be calculated from the general form of Hooke`s law [50].

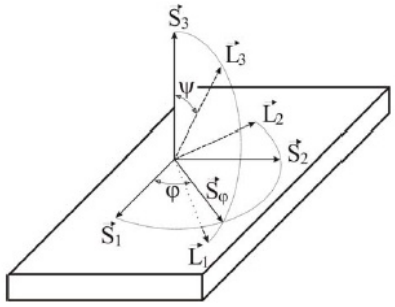

Figure 3.6: Definition of the laboratory coordinate system L_i, simple coordinate system S_i, and the angles ϕ, ψ [50].

In polycrystalline materials, three basic types of $d_{\phi\psi}$ vs. $sin^2\psi$ behaviour are observed which are shown in Figure 3.7.

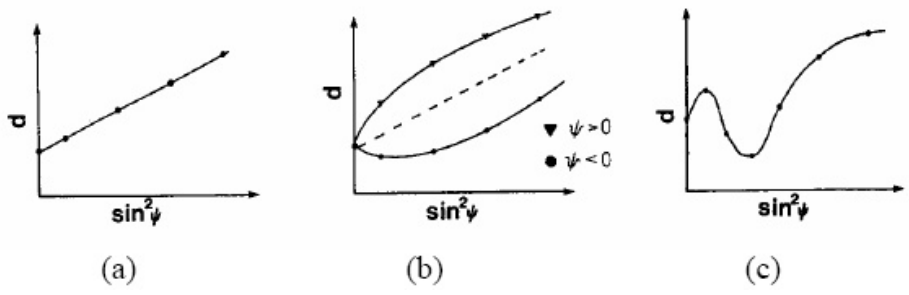

Figure 3.7: Types of d vs. $sin^2\psi$ plots from polycrystalline materials. (a) and (b) show regular behaviour whereas (c) shows oscillatory non-regular behaviour [50].

Figure 3.7a,b depict regular $d_{\phi\psi}$ vs. $sin^2\psi$ behaviour where Figure 3.7a shows the ideal, linear curve progression. Figure 3.7b shows non-linear behaviour where d measured at positive and negative Ψ will be different. This effect is called Ψ-splitting and is assigned to the elastic anisotropy. Data exhibiting regular behaviour can be analyzed by methods based on the basic equation [50]. On the other hand Figure 3.7c shows oscillatory non-regular behaviour which can not be analyzed by using the basic equation of the $sin^2\psi$ method without further modification [50].

4 Thermally activated processes

4.1 Diffusion

Many reactions and processes that are important in materials rely on the transport of mass. This is necessarily accomplished by diffusion. Diffusion is the stepwise migration of atoms from one lattice site to another. For one atom to make such a move, two conditions must be met. First there must be an empty adjacent site, and second the atom must have sufficient energy to break bonds with its neighbour atoms and then cause some lattice distortion during the displacement. The capability for diffusion increases with increasing temperature [51].

The two dominant mechanisms for diffusion in solids are shown in Figure 4.1. The first type of diffusion (Figure 4.1a) involves atoms that migrate via interstitial positions. The so called interstitial diffusion is mainly found for small impurities such as H, C, N and O. In most solids, interstitial diffusion occurs much more rapidly than diffusion by the vacancy mechanism (Figure 4.1b), since the interstitial atoms are typically smaller, and thus more mobile [51,53].

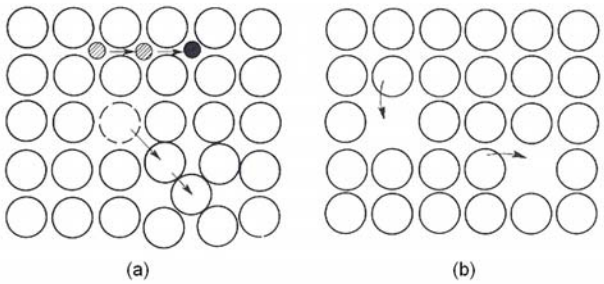

Figure 4.1: Schematic representation of (a) interstitial diffusion and (b) vacancy diffusion (modified from [52]).

During vacancy diffusion (Figure 4.1b), the atoms interchange from a normal lattice position to an adjacent vacancy. This process necessitates the presence of vacancies and thus strongly depends on the vacancy concentration [51,53]. Since these mechanisms need thermal activation, the occurrence of a diffusion process as well as the vacancy concentration are proportional to $e^{-Q/kT}$ where Q is the enthalpy of the formation and motion of a vacancy. Q has the absolute lowest value for the described vacancy mechanism

compared to all other possible mechanism in a substitutional solid solution and is thus the most likely process [53].

Most PVD processes employ ion bombardment to modify the structure of the film, as described in chapter 2, which results in high defect densities, such as vacancies or interstitials, giving rise to different driving forces for diffusion in the films [54].

4.2 Recovery and stress relaxation

All defects in materials which are not in a thermodynamical equilibrium tend to heal, provided that the energy, or respectively the temperature, is high enough. During recovery, crystal defects heal in several stages according to their thermodynamical stability. Recovery starts with the recombination of vacancies and interstitial atoms or their diffusion to interfaces, e.g. grain boundaries [55,56]. At higher temperatures, the stored energy within the material can also be lowered by dislocation movement. This results in annihilation of dislocations and rearrangement of dislocations in low energy configurations. Both processes are achieved by glide, climb and cross slip of dislocations. Therefore, recovery depends on the stacking fault energy of a material which determines the rate of dislocation climb and cross slip (materials with high stacking fault energy show high amounts of recovery). Hence, in physical metallurgy, recovery is defined as interaction of dislocations due to their long range stress fields [53].

PVD hard coatings show high defect densities due to the ion bombardment during deposition (see chapter 2.3). Such coatings often exhibit a nanocrystalline structure, especially in the case of a nanocomposite, which makes it necessary to consider size effects in the material [1]. In the case of nanometer size grains, the so called Hall-Petch relation [57], which is based on dislocation pile-up at the grain boundaries, is of importance. In case of very small grains, there is only space for a small number of dislocations in one grain. Due to the fact that hard coatings normally possess a high melting temperature, the mobility of dislocations, even at higher temperatures, is also low and the point defects act as obstacles for dislocation movement. Therefore, the definition of recovery as interaction of dislocations does not hold for such hard coatings. Only the first steps of recovery, the annealing of different point defects, take place during heating of this type of materials.

Another thermally activated process of interest is stress relaxation, defined as the decrease in stresses over time at constant strain [55]. In case of coatings, stress relaxation is referred to the relaxation of the lattice due to migration, redistribution or annihilation of stress-active lattice defects [54]. Thus, a decrease in compressive residual stresses after annealing can be observed. The point defect density and therefore the residual stresses itself act as additional driving force for defect annihilation, and consequently, stress relaxation. The higher the stresses or annealing temperatures are, the higher is the stress relaxation observed [58-61] (see paper I). It should be noted that stress relaxation in coatings is not necessary connected to constant strain. Particularly, in the way stresses have been measured in this work as function of temperature, the composite coating/substrate bends during heating, at the same time as stress relaxation is taking place.

4.3 Recrystallization and grain coarsening

Recrystallization involves the formation of new strain-free grains in certain parts of the specimen [62]. The microstructure at any time is divided in recrystallized or non-recrystallized regions, and the recrystallized fraction increases as the transformation proceeds. The process characterised by nucleation and growth is called primary recrystallization. Recrystallization occurs if the thermal activation and the driving force are sufficient [53,61]. The driving force for recrystallization is mainly provided by the dislocation density within the material. Regions of higher dislocation density and interfaces may act as nucleation sites for recrystallization. The fraction of recrystallized material rises rapidly with time until the recrystallized volumes meet each other and thus the rate of recrystallization will decrease [53].

Besides temperature and time, the recrystallization process is influenced also by the material, its stored energy (defect density) and density of interfaces. The recrystallization process occurs at lower temperatures if the stored energy is increased which provides the driving force for the process [53].

When primary recrystallization is complete, further growth of recrystallized grains may occur, since the structure is not yet stable. The driving force for grain growth and coarsening of the microstructure is the reduction of interfacial energy. In nanostructured materials, an extremely high interfacial energy is stored due to the high amount of grain and phase boundaries [61,63].

Nanostructured PVD hard coatings exhibit high defect densities and high interfacial energies due to their small grain size. In such small grains, especially in a two phase structure, the density of dislocations which can interact may be assumed to be low [64]. When a nanostructured coating is exposed to elevated temperatures, most of the point defects anneal out during the preceding stress relaxation, and consequently, only interfacial energy remains as driving force. Therefore, it is much more likely that grain coarsening occurs without the step of recrystallization in such materials. Low deformed metals show similar behaviour if the driving force for nucleation is too low and the grain boundaries start to move, which is called “strain induced grain boundary motion”. In this case, the grains with lower defect density grow on expense of the grains with higher defect density. This process and grain coarsening are often included in the term of recrystallization in literature [53].

5 Material selection and design

Transition metal nitrides and carbides have been the most studied and investigated compounds since the beginning of the use of hard coatings to improve the performance of tools and mechanical components [65]. Due to their bond structure, a mixture of covalent, metallic and ionic components, this type of coatings show a high hardness, chemical inertness, good electrical conductivity and excellent wear resistance. One of the first materials used in industry to coat tools was TiN. TiN with its face-centered cubic structure was, and still is, the base for further development of advanced coatings. It is obvious that, whenever new situations were envisaged for application of hard coatings, there were new demands which could not be satisfied with the existing, e.g. Ti-based, compounds [3,65].

The first approach to improve the properties of hard coatings is to control and influence the microstructure. There are many possibilities to achieve this goal by changing the deposition parameters as described in chapter 2.3. Using the simple way of applying ion bombardment during deposition, the density of the structure and the compressive stresses in the coating, and consequently the hardness, can be increased. In general, compressive stresses are most advantageous since they can hinder the formation of cracks or their growth [66]. On this account, the first step of the present study was to analyze in detail the influence of coating thickness on stresses and stress relaxation of TiN coatings in order to get a basic understanding how theses properties are related to the film structure (see paper I). Previously, stress investigations were conducted by Janssen et al. on metal films up to 6 µm thick where tensile residual stresses caused by grain boundary shrinkage obey a power law dependence on coating thickness [67,68]. For sputtered TiN hard coatings above 1 µm thickness, a slight stress-thickness dependence was found [69,70]. According to Kamminga et al. [69], it can be assumed that in sputtered TiN films point defects determine the growth stress. Not only residual stresses but also stress relaxation due to defect annihilation at elevated temperatures is of vital importance for high-temperature applications. Only a few investigations have been published on stress relaxation of hard coatings [58,59,70,], and essentially nothing was known about thickness-dependent stress relaxation at elevated temperatures (see paper I).

Nanostructured coatings offer another possibility to improve the coating properties. Nanostructured materials are solids composed of structural elements with a characteristic

size, in at least one direction, of a few nanometers. The various types may be classified as shown in Figure 5.1 [71].

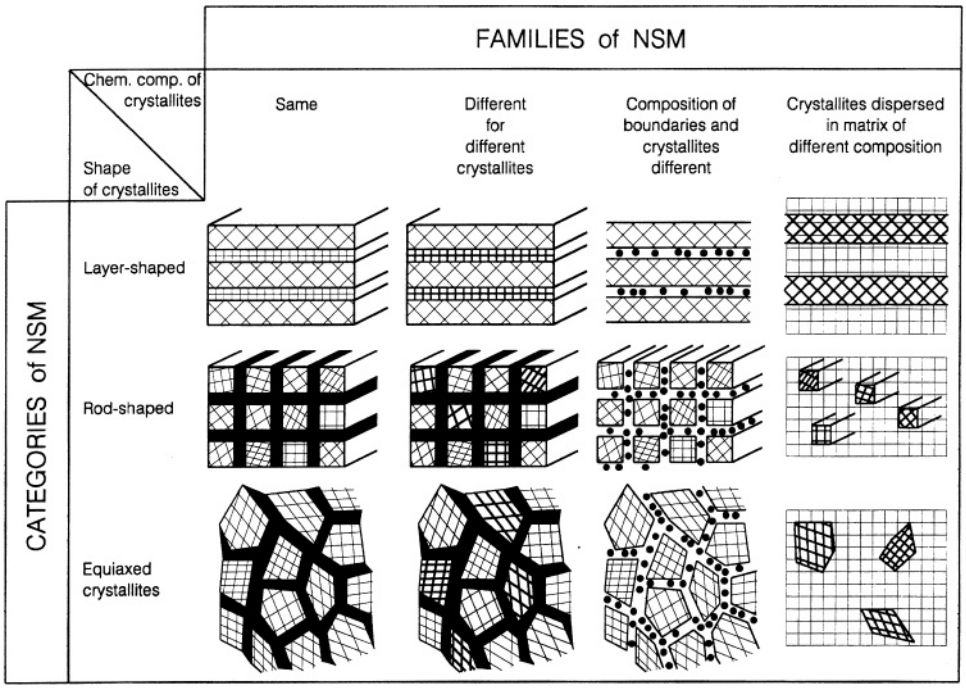

Figure 5.1: Classification scheme for nanostructured materials according to their chemical composition and the dimensionality (shape) of the crystallites (structural elements) forming the nanostructured material [71].

According to the shape of the crystallites, three categories of nanostructured materials may be distinguished: layer-shaped, rod-shaped and equiaxed nm-size crystallites. Depending on the chemical composition of the crystallites, the categories may be grouped into four families [71]. In the most simple case (first family, Figure 5.1), all crystallites and interfacial regions have the same chemical composition. The second family of nanostructured materials consists of crystallites of different chemical composition. If the compositional variation occurs primarily between crystallites and the interfacial region, the third family of nanostructured materials is obtained. In this case, one type of atoms segregates preferentially to the interfacial regions so that the structural modulation is coupled to the local chemical modulation [63,71].

Additionally, nanostructured materials are known in which one or all constituents are non-crystalline (fourth family, Figure 5.1) [63,71] such as metal nitrides in an amorphous Si_3N_4 matrix [72].

For the investigations in this thesis, model systems should be defined which can be useful to understand the residual stresses and the stress relaxation in multiphase systems. Hence, the first family of nanostructured materials is unfeasible due to the fact that the chemical composition of the crystallites is the same. On the other hand, amorphous phases are not useful because phase transitions during heating, such as crystallization, are undesirable. Therefore, the fourth family of nanostructured materials is also unemployable. For this reason, only model systems which belong to the second and third family of nanostructured materials are useful.

Concerning that the second phase should show adequate differences in material properties for a more explicit determination of the influence on the system, a pure metal was chosen. Since the deposition process takes place in a reactive atmosphere, the metal should be chemical inert. Hence, noble metals have to be considered and Ag was chosen as second phase.

In a first step a multilayer arrangement of TiN/Ag was investigated (paper II). Figure 5.2a shows a TEM micrograph of a as deposited film with a porous structure of the Ag layers. Due to sintering processes the film exhibits a densified structure after annealing (Figure 5.2b).

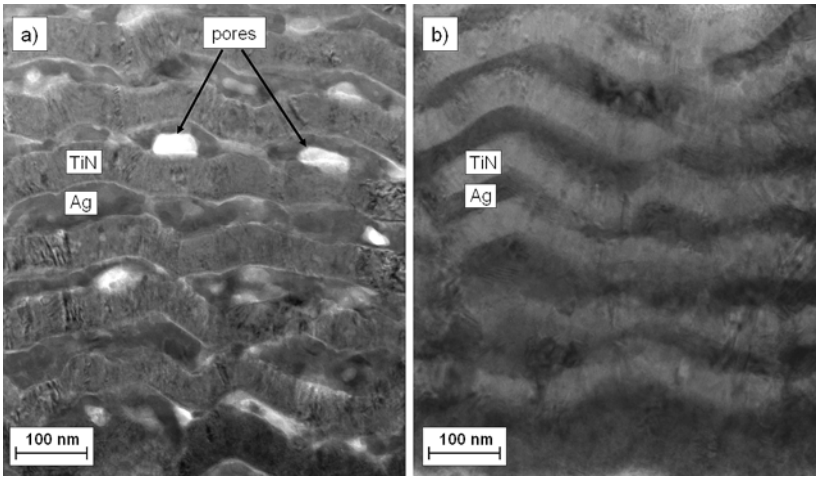

Figure 5.2: TEM images of TiN/Ag multilayer coatings (a) before and (b) after annealing [paper II].

From literature it is known that metallic interlayers are frequently used to increase adhesion of hard transition metal nitride coatings to the surface of tools or engineering components. Often, these interlayers improve the performance of a hard coating, e.g. TiN

with a metallic Ti interlayer [73,74]. Stresses and structure of the hard layer are highly influenced by the soft metallic interlayer, both in bilayer [75-77] and multilayer arrangements [78-80]. An important parameter is the plasticity of the soft layer since higher plasticity usually leads to better adhesion [81]. Besides the relation between the structure arrangement and stress in hard nitride / soft metal multilayers, their thermal stability is of importance. It has been shown that elevated temperatures give rise to stress relaxation due to defect annihilation (often referred to as recovery [82]) and grain coarsening in nitride coatings [58,59,70 and paper I]. To illuminate the role of soft metallic interlayers on residual stress and thermal stability of hard coatings, TiN/Ag multilayers of various bilayer thickness Λ is studied in paper II.

To increase the complexity of the system, the materials combination TiN/Ag was deposited as a nanocomposite. It has been shown in literature that a low fraction of a metallic component which segregates at the grain boundaries of a nitride can be used to realize hard and superhard coatings [83] like ZrN/Cu [84,85] or TiN/Cu [86-88]. The addition of a soft metal phase into a hard coating offers also the possibility to improve coating toughness by influencing e.g. intrinsic stresses and structure [89-93]. Very limited information exists about stress relaxation in hard nitride / soft metal nanocomposite coatings at elevated temperatures as function of metal content. The effect of the metal content of magnetron sputtered TiN/Ag nanocomposite films on structure and residual stresses as well as stress relaxation at elevated temperatures is investigated in paper III.

The friction coefficient of most of the transition metal nitride coatings, e.g. TiN or CrN, is fairly high and the tribological effectiveness, especially at elevated temperatures, is insufficient [94]. In recent years, several investigations have been published which deal with new concepts for friction and/or wear reducing hard coatings. One possibility to reduce friction is to form nanocomposite or superlattice structures which combine solid lubricants like graphite, DLC, MoS_2 or WS_2 with hard phases [95-99]. The incorporation of elements, like V, which are able to form lubricious oxides on the surface during high temperature exposure, can also lead to enhanced tribological properties [100-102]. However, these oxides are only formed under certain environmental conditions, i.e. oxygen containing atmosphere and elevated temperature. In addition to these lubricious oxides, combining a soft metal phase with a hard compound has been reported as a promising approach to improve coating performance. These soft metal phases give rise to improved tribological properties over a wide temperature range due to their low shear strength. For

this purpose, preferably Au and Ag, due to their chemical inertness, are used in combination with oxides [103-106], nitrides [99,107-109] and carbides [110], where reduction of friction and/or wear have been reported. In previous investigations, it was found that the addition of Ag to transition metal nitride coatings only reduces the friction coefficient at room temperature (RT) when a relatively high Ag content is used [107-109]. For high Ag contents, Endrino et al. reported about a considerably reduced friction coefficient in vacuum also for the systems WC/Ag and TiC/Ag [110]. Also by adding Au to yttria-stabilized zirconia, a strong decrease of the friction coefficient with increasing Au content was obtained at RT [103]. Due to the above stated improvements in tribological behaviour reported in literature also tribological test were conducted on the TiN/Ag nanocomposite system. Particularly, the influence of the Ag content on the tribological response of a TiN/Ag composite film at RT and elevated temperatures is investigated in paper IV. The friction coefficients decrease with increasing temperature due to the lubricious properties of the Ag phase (Figure 5.3).

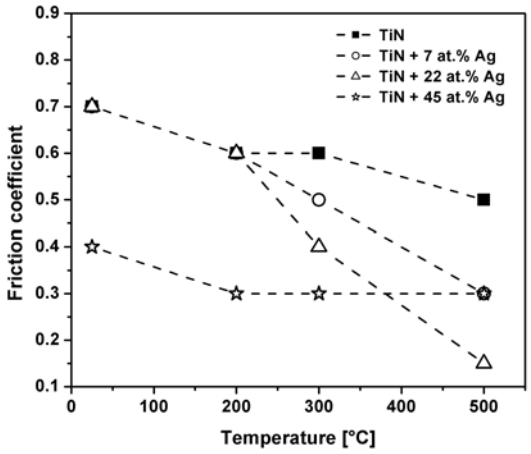

Figure 5.3: Friction coefficient dependent on temperature and Ag content of TiN/Ag nanocomposite coatings (paper IV).

Despite the beneficial properties of Ag, working with this element is connected to some difficulties; e.g. the high surface mobility of the Ag atoms results in clustering and liquid-like coalescence [111]. Consequently, the surface roughness of the multilayers increases with layer thickness [112] (paper II), and initial porosity in the multilayer as well as the nanocomposite leads to sintering effects during annealing, all of which influences the stress development significantly (paper II and III). To minimize these problems, a metal

with lower surface mobility (Cu) was chosen to design a comparative study, being arranged in the form of TiN/Cu multilayers and nanocomposites (paper V). Significant differences could be observed by changing the metal (Figure 5.4).

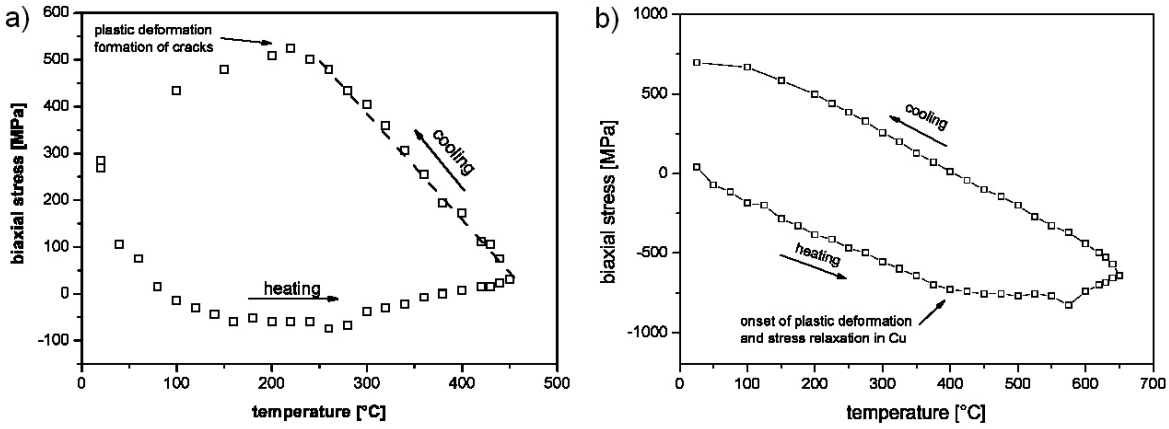

Figure 5.4: Stress-temperature behaviour of (a) TiN nanocomposite coatings with 7 at.% Ag and (b) TiN nanocomposite coatings with 7 at.% Cu.

Figure 5.4a shows the stress-temperature behaviour of the TiN/Ag nanocomposite coating with 7 at.% Ag. The curve reaches a plateau in compressive stresses at a temperature of 150°C. This plateau in stresses can be related to the fact that all further stresses which appear are relieved plastic deformation of the Ag phase. Above 280°C the stresses become tensile which can be explained by sintering effects and the densification of the coating, as it is shown for the structure of a TiN/Ag multilayer coating in Figure 5.2. For the coating with 7 at.% Cu (Figure 5.4b) the plastic deformation is less pronounced. This is related to the increased strength of the TiN/Cu nanocomposite. Since, the Cu atoms have a lower mobility compared to the Ag atoms, the TiN/Cu nanocomposite coating shows no sintering effects which may also be related to a low initial porosity. However, during cooling TiN/Ag as well as TiN/Cu nanocomposites exhibit linear thermoelastic behaviour.

6 Coating characterisation

Morphology, structure, thermal behaviour and tribological properties of the coatings investigated in this work were characterized using several common methods. The different experimental techniques are briefly explained in the following chapters.

6.1 Atomic force- and scanning electron microscopy

Atomic force microscopy (AFM), also called scanning force microscopy (SFM), is a real-space imaging technique that can produce topographic images of a surface in all three dimensions, ideally with atomic resolution. Normally, the lateral resolution of AFM is about 1 nm [113]. Atomic force microscopes can measure the force between a sample surface and a very sharp probe tip mounted on a cantilever beam. When the tip comes within a few Å of the sample`s surface, repulsive van der Waals forces between the atoms on the tip and those on the sample surface cause a deflection of the cantilever. The magnitude of the deflection depends on the tip to sample distance. To scan the tip across the sample, a raster scanning motion controlled by piezoelectric tubes is applied and a feedback loop operates on the scanner to obtain a constant separation between the tip and the surface. The most common method for monitoring the deflection is with an optical detection system. A laser beam is reflected from the back side of the cantilever into a position-sensitive photo diode. A given cantilever deflection will then correspond to a specific position of the laser beam on the detector. Since the position-sensitivity of the photo diode is very high, the vertical resolution is sub-Å [113]. There are two basic modes of operation, the contact mode, described above, and the non-contact mode. In the non-contact AFM mode, the cantilever is located tens to hundreds of Å from the specimen surface. To prevent surface contact, a stiff cantilever is used which vibrates typically at 100 to 400 kHz. Changes in vibrational amplitude or resonant frequency are then detected. The main advantages of the non-contact AFM are the ability to probe soft or elastic materials and minimization of surface contamination and tip degradation [114].

In this work, the film surface of selected nanocomposite coatings was characterized using AFM with conventional Si-tips in tapping mode, according to the procedure described in [115]. The tapping mode is similar to the non-contact mode using larger vibration

amplitudes which are controlled and held constant with the difference that the tip touches the surface.

Scanning electron microscopy (SEM) [114,116] was used to investigate the morphology of the films on cross-sections and the surface. Additionally, the wear tracks after room temperature and high temperature tribological tests were studied.

Energy-dispersive X-ray (EDX) analysis [114] (in the SEM) was used to identify the chemical composition of the nanocomposite films. The atomic percentages presented in this work are calculated by [Me]/([Me]+2[Ti]) without considering impurities which corresponds to [Me]/([Me]+[Ti]+[N]) assuming that the formed TiN is nearly stoichiometric to correct the measurement errors of light elements like N.

6.2 Transmission electron microscopy

For transmission electron microscopy (TEM) investigations, thin foils of thickness 5 to 500 nm (depending on the material and type of investigation) have to be prepared. With these foils it is possible to visualize structures in the nm range. In comparison, the resolution of the SEM is lower by about an order of magnitude [114,116].

TEM can be used not only for imaging but also for diffraction studies. It is one great advantage that the area of diffraction can be very small. This type of diffraction is called selected area electron diffraction (SAED). The combination of diffraction with imaging offers new imaging modes. If the image is constructed by the light of the 0^{th} order diffraction it is called bright field (BF) imaging or also conventional TEM. This is done by placing suitable sized apertures in the back focal plane of the objective lens. If only one of the diffracted beams is chosen, it is called dark field (DF) imaging. This is realized by an aperture which blocks both the 0^{th} order diffraction and the other diffracted beams [114,116].

In this work, film cross-sections were used for TEM investigations. A couple of samples were prepared using tripod polishing with final Ar ion milling. Samples which could not prepared by tripod polishing due to their poor mechanical properties were prepared using focused ion beam (FIB) technique. A Ga ion beam is used to cut (ion milling) a specimen out of a bigger sample [114]. An example for a FIB prepared sample is shown in Figure 5.2 where TEM was used to compare the structure of coatings before and after annealing.

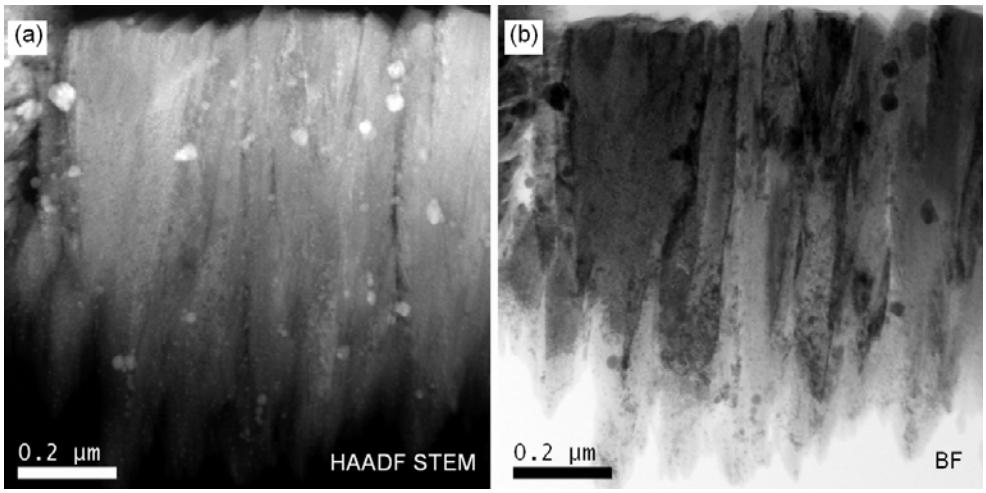

Figure 6.1: DF (a) and corresponding BF (b) TEM image of a TiN nanocomposite coating with 7 at.% Ag.

Figure 6.1 shows TEM cross-sectional micrographs of a coating with 7 at.% Ag as used for the investigations described in paper III and IV. The differences of DF, which provides mass contrast images, and BF are visible. The bright spots in the DF micrograph (Figure 6.1a) represent Ag particles as confirmed by EDX measurements.

6.3 X-ray diffraction

X-ray diffraction (XRD) is a non-destructive technique to address all issues related to the crystal structure of solids including lattice constants and crystallography, identification of unknown materials, preferred orientation of polycrystals, stress analysis and the determination of grain size. In the symmetrical Bragg-Brentano geometry used for this work, only the diffraction from crystallographic planes with the plane normal parallel to the diffraction vector are investigated [116,117].

The width of a diffraction line is determined by the number of elementary waves which are added coherently to build-up the interference pattern, and hence, by the average grain size of crystals of which the material is composed [116]. The XRD profiles of the coatings investigated were fitted with a Pseudo-Voigt function, which is a linear combination of a Cauchy and a Gaussian function. The Cauchy function corresponds to the domain size of coherently diffracting domains whereas the Gaussian function corresponds to the strain [118]. The broadening of the diffraction peaks expressed by the integral breadth β was used to calculate the size of the coherently diffracting domains $\langle D \rangle$ in the films [119,120].

The parameter <*D*> corresponds to the average length of crystalline domains in the direction of the diffraction vector and represents the crystalline regions possessing no planar defects [120].

In the case of nanocomposite coatings, two pseudo-Voigt functions were used to fit the overlapping TiN and Me peaks, if they are present, as shown in Figure 6.2.

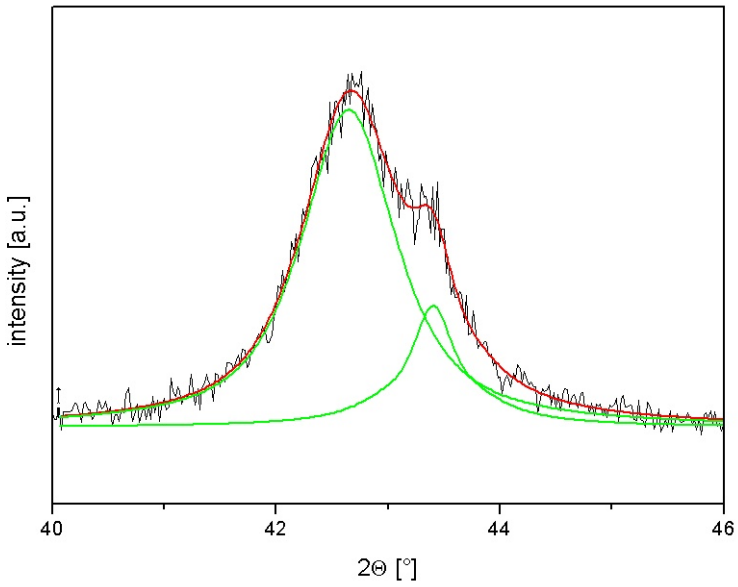

Figure 6.2: Two overlapping peaks of a XRD-pattern of a TiN/Cu nanocomposite coating with 19 at.% Cu. The greene curves are the two fitted Pseudo-Voigt functions, red is the cummulative curve of the fit.

Additionally, the texture coefficient according to Harris [121] was calculated for a couple of samples (paper I and II). This gives a rough idea if preferred crystallographic orientations exist by comparing the peak areas or heights with the powder standard.

6.4 Biaxial stress-temperature measurement

To characterize the as deposited stresses and the stress relaxation of the different coatings, stress-temperature measurements (STM) were conducted using a home-made unit. The measured stresses are biaxial since plate geometry was used for the samples (see chapter 3.3.1). Therefore, the used method is also called biaxial stress-temperature measurement (BSTM). The samples used were Si (100) plates with 20x7 mm^2 and different thicknesses.

During BSTM, the films were subjected to a thermal cycle in vacuum ($p \leq 10^{-3}$ Pa) at a heating and cooling rate of 5 K min^{-1}. The maximum annealing temperature was dependent on the material combination and design. Two parallel laser beams were used to measure the variation of substrate curvature during annealing. The biaxial film stress was calculated from the substrate-curvature radius, which was calculated from the distance d_1, using the modified Stoney equation [48] (see chapter 3.3.1). The measurement setup is shown in Figure 6.3 where d_0 is the parallel distance of the two laser beams.

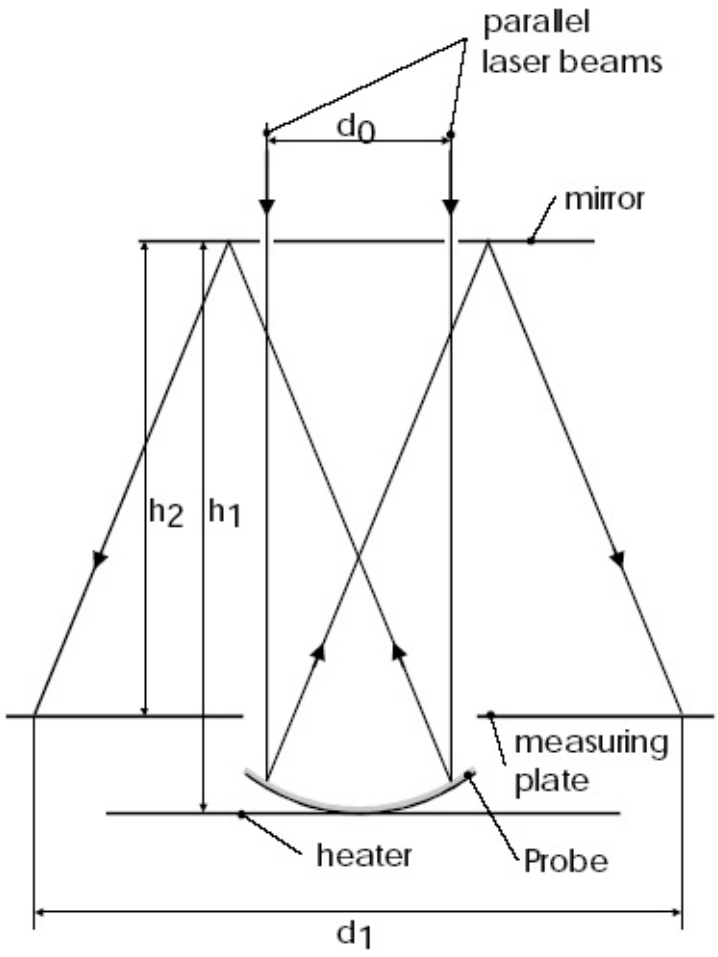

Figure 6.3: Principle of the curvature measurement via two parallel laser beams [20].

To ensure a large total distance L ($L = h_1+h_2$) between the specimen and the measuring plate, which is necessary to minimize experimental errors, the laser beam is reflected by a mirror. L can be adjusted by a parallel movement of the mirror between 2 and 5 m. The specimens are placed with the coated side on a heating plate. Temperatures up to 700°C can be reached which are controlled by a thermocouple placed on a silicon reference sample on the heating plate. To prevent oxidation of the samples during annealing, the

specimen and the heater are placed in a vacuum recipient. Representative results are shown in Figure 5.4.

6.5 Nanoindentation

The coating hardness and Young`s modulus were determined by nanoindentation [122] using a Berkovich indenter according to the Oliver and Pharr method [123]. The coatings were tested before and after high-temperature tribometer tests. After calibrating the device, hardness measurements were conducted at maximum loads between 2 and 50 mN with 2 mN steps. The values of film hardness H were then plotted against the penetration depth h_t, and only those values which belong to a plateau in the values of H, where no influence of the substrate can be guaranteed, were taken for calculating the average hardness of the film. Additionally the upper 20% of the elastic unloading curve were used to calculate the Young`s modulus of the coatings. Additional information on the principles of nanoindentation can be found in Ref. [124].

6.6 Tribology

Due to the variety of possible mechanisms operating during tribological contact, there are many different configurations available to test the friction and wear behaviour of coated surfaces. The pin-on-disk and ball-on-disk tests are by far the most widely used measurement setups [125]. Thus, a high temperature ball-on-disk tribometer was used to perform tribological tests for the different nanocomposite coatings used in this work. Alumina balls were used as counterpart. The ball is pressed onto the rotating sample, a coated steel disc, with a defined load causing wear. Representative friction curves recorded during tests at different temperatures are shown in Figure 6.4. In this example, the friction coefficient decreases with increasing testing temperature due to the lubricious properties of the Ag phase.

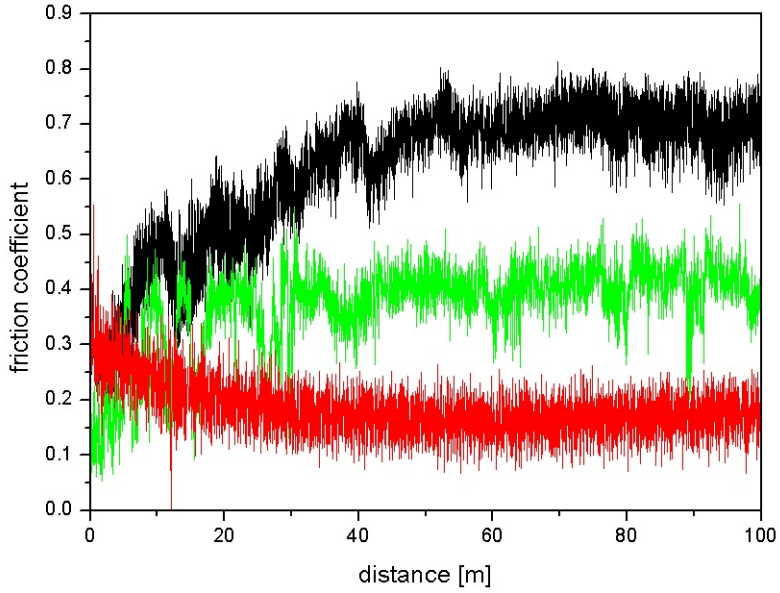

Figure 6.4: Friction coefficients of TiN/Ag nanocomposite coatings with 22 at.% Ag vs. sliding distance at different temperatures (black = RT, green = 300°C, red = 500°C).

Friction is defined as the resistance encountered by one body in moving over another. Due to this definition, there are two important classes of relative motion: sliding and rolling. The ratio between friction force and normal load (load on the ball) is known as friction coefficient [126]. The three basic mechanisms of sliding friction are adhesion of asperities in contact, ploughing by wear particles and hard asperities and deformation of surface asperities [125]. In the used ball-on-disc tribometer, the counterpart is fixed and is sliding over the surface of the sample.

Wear is defined as the removal of material from solid surfaces as a result of relative motion between two contacting surface [8]. Wear can be classified in four different wear mechanisms. These are adhesive wear, abrasive wear, surface fatigue and tribochemical reactions.

Adhesive wear occurs due to the formation and breaking of interfacial adhesive bonds, e.g. cold-welded junctions [127]. Abrasive wear is the displacement of material caused by hard particles or protuberances [128], and can be classified into the two processes two body and three-body abrasion. In two-body abrasion, the abrasive material is fixed to one of the surfaces in contact whereas in three body abrasion the abrasive material can move freely between the two surfaces [127]. Surface fatigue is a result of the formation of cracks in the surface and subsurface regions due to stress cycles in tribological contacts that result in the formation of wear particles [127]. When wear particles are formed, due to the reaction of

the surfaces in contact with the environment during the relative motion, the wear mechanism is known as tribochemical reaction. This occurs when the sliding process takes place in an oxidative or corrosive environment. Frictional heating in the contact is able to accelerate or promote these chemical reactions [127].

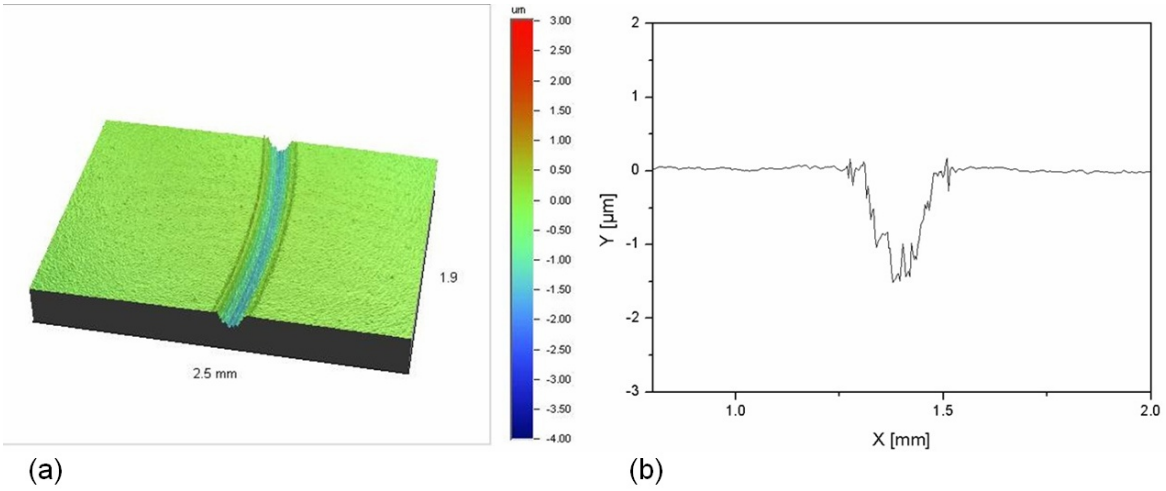

Figure 6.5: (a) 3D image and (b) corresponding 2D cross section of a wear track after room temperature ball-on-disc test for a TiN nanocomposite coating with 7 at.% Ag.

In contrast to the friction coefficient, wear is not recorded directly during the test. To characterize the wear track, a white-light profilometer was employed which uses interferometry to record a three-dimensional (3D) image of the wear track and the coating surface as shown in Figure 6.5a. A two-dimensional (2D) cross-section through the 3D image is shown in Figure 6.5b. The morphology of the wear tracks helps identifying the wear mechanisms present during the test.

7 Summary and conclusions

Transition metal nitride coatings are widely used to improve the performance of tools or components due to their high hardness, chemical inertness, good electrical conductivity and excellent wear resistance. The performance of a coated surface is determined, among others, by its structure and residual stresses, particularly when it comes to thermal loads. Since the requirements in industry are permanently increasing, e.g. higher cutting speeds, the working temperatures consequently increase. Stresses and strains in the coating and the substrate due to mechanical and thermal loads are thus of interest to prevent failure. For a further increase of performance and lifetime, it is of major importance to understand how the structure of a coating, coating architecture and residual stresses might be influenced by high temperature exposure.

The first approach in this work was to describe correlations between residual stresses and stress relaxation as function of coating thickness for a basic model coating, i.e. sputtered TiN (see paper I). Residual stress, the amount as well as the onset temperature of stress relaxation for films deposited at different bias voltages were related to a thickness-dependent gradient in point defect density. This gradient is caused by the structural evolution during film growth as described in the structure zone models and is supposed to be the determining factor for stresses in the coatings. Thinner films, consisting of equiaxed polycrystals formed during early film growth, exhibit high average defect densities which result in high compressive stresses. These high defect densities represent high driving forces for relaxation phenomena; consequently, thinner films show high amounts and low onset temperatures of stress relaxation. In contrast, the competitive growth stage which determines the structure of thicker films results in lower average defect densities. Thus, thicker films show lower compressive stresses and the connected lower driving force leads to higher onset temperatures for stress relaxation. The increasing compressive stresses with decreasing film thickness in the TiN coatings are contrary to those found for CrN [43]. It is yet not clear why these two systems show different behavior, particularly when it is assumed that the structure as described in the structure zone models is the determining factor for the stresses, and both grow as Zone T coatings. However, these differences have been confirmed in the meantime by other authors [43].

The next step of the present work was to investigate a more complex system consisting of a multilayer arrangement of TiN and Ag. The goal was to elucidate the correlations between

film structure and stress development during thermal cycling for sputtered TiN/Ag multilayer films of different bilayer thickness Λ. SEM and TEM investigations revealed a porous nature of the Ag layers where layer porosity, and consequently also coating roughness, increases with increasing Λ. Above a critical annealing temperature, sintering takes place which yields a densification of the Ag layers. The more pronounced this densification is, the more tensile stresses are induced, and as a consequence, the slope of the biaxial stress temperature curves changes at higher temperature. After reaching a certain temperature (aprox. 380°C), biaxial stresses of all coatings reach a plateau, since any further stress which appears above this temperature is relieved by plastic deformation of the Ag interlayers (see paper II). A multilayer arrangement consisting of TiN and Cu was also investigated (paper V). In contrast to TiN/Ag, no significant sintering effects could be found. The stresses change from tensile to slightly compressive during annealing, and reach a plateau like in the case of the TiN/Ag coatings. During cooling, all TiN/Me multilayer coatings exhibit linear thermoelastic behaviour.

To increase further the complexity of the system, the material combination TiN/Me was also deposited as nanocomposites. Correlations between film structure and stress development during thermal cycling as function of the Ag content are described in paper III. The coatings exhibit a columnar structure with Ag crystallites of 3 to 50 nm size within the columns. Additionally, a layered structure within the columns was observed for higher Ag contents, which originates from the sample rotation during deposition. During annealing, films with high Ag contents show a zero stress level from deposition temperature up to the maximum annealing temperature due to stress relieve by plastic deformation of the Ag phase. Due to their higher strength, films with lower Ag contents show a slightly compressive stress plateau above deposition temperature. However, once a critical annealing temperature is reached, the stress changes from compressive to slightly tensile. This change in slope of the stress-temperature curve is mainly related to stress relaxation of the TiN phase. Stress relaxation of TiN is also present in the films containing more Ag but is overruled by plastic deformation of the soft Ag phase. In the system TiN/Cu (see paper V), the coatings also show a columnar structure. Neither bigger Cu particles nor layers from the sample rotation could be found. A change in the preferred orientation of TiN between 7 and 14 at.% Cu could be observed which causes an increase in the as-deposited stresses, as well as a structural relation between the two phases. However, if a critical amount of Cu in the coating is exceeded, the stresses decrease

significantly. This can be related to the relieve of stresses via plastic deformation and stress relaxation in Cu during deposition. Due to their increased strength, the nanocomposite coatings with lower Cu content show a stronger increase in compressive stresses during heating than the coatings with higher Cu content. The onsets of plastic deformation and stress relaxation in Cu ocurrs at a certain temperature. 50°C above deposition temperature, the onset of stress relaxation in TiN causes a second change in the slope of the stress-temperature curves. The TiN/Me nanocomposite coatings exhibit linear thermoelastic behavior during cooling, where the slopes are steeper the lower the Me content is.

Soft metal phases give also rise to improved tribological properties over a wide temperature range due to their low shear strength. Therefore, correlations between Ag content and tribological properties were investigated for sputtered TiN/Ag nanocomposite films (see paper IV). At room temperature, wear increases with increasing Ag content due to the concomitant softening of the coatings. However, coatings with very high Ag content show low wear, presumably due to the increased elasticity of the coating and energy dissipation by elasto-plastic deformation during the tribological test. Friction seems to be determined by shearing of the coatings for Ag contents higher than 30 at.%, and by the interaction of wear debris with the surfaces in contact for lower Ag contents. At elevated temperatures, Ag segregates to the surface and acts as a solid lubricant which reduces friction and wear, particularly when a continuous Ag tribolayer is formed.

In the present work, it has been shown how the intrinsic stresses of a film might be influenced in the as-deposited state and during thermal cycling by selecting a defined structure. The findings on the stress-temperature behaviour of TiN might be applicable for designing the stresses in coated tools or components, provided that the coating shows a similar behaviour like TiN. For example, it could be advantageous to have low compressive stresses at the interface, and increasing compressive stresses towards the surface, since they are favourable to prevent cracks. These stresses can be lowered by a decreased ion bombardment at the beginning of the deposition process to increase the adhesion of the film, and then be increased by increasing the ion bombardment with proceeding film growth. The addition of a soft second phase in different coating architectures results in decreased compressive or slightly tensile stresses after deposition. This type of coatings may be used as interlayer to lower the overall stresses in coatings, e.g. when delamination might occur as it is the case for very thick coatings. Both architectures, multilayer and nanocomposite, are beneficial for this application but a

nanocomposite coating is superior due to the less sharp interface, and thus, higher interfacial strength between the interlayer and the “bulk” coating. However, in the systems with the soft second phase, mainly tensile stresses appear which are normally disadvantageous in application due to easy crack formation. The onset of plastic deformation at relatively low temperatures, which causes the tensile stresses after annealing, is in that case an unfavourable effect. Therefore, such coatings have potential for applications at lower temperatures or loads for which the present tensile stresses are subcritical. Additionally, the soft metal could be also useful for certain applications, e.g. components, where it acts as a solid lubricant at low and medium temperatures provided that the mechanical load is not too high.

There are still some interesting structures that should be investigated in future work. In the first place, there is an open question concerning the different thickness dependent stress behaviour of CrN and TiN. It might also be of interest how growth stresses and point defect density of a single phase material with solid solution like TiAlN determine its thickness dependent stresses and stress-temperature behaviour, particularly when precipitation occurs. This is of high interest since one of the strategies in coating development is the introduction of additional elements into single phase coatings which might decrease its thermal stability.

8 References

1 E. Arzt, Acta Mater. 46 (1998) 5611.

2 E.D. Hondros in W. Gissler, H.A. Jehn (eds.), Advanced Techniques for Surface Engineering, Kluwer Academic Publishers, Dortrecht, 1992, 1.

3 S. PalDey, S.C. Deevi, Mater. Sci. Eng. A342 (2003) 58.

4 W.D. Sproul, Surf. Coat. Technol. 86-87 (1996) 170.

5 S. Veprek, J. Vac. Sci. Technol. A 17 (1999) 2401.

6 F. Spaepen, Acta Mater. 48 (2000) 31.

7 C. Mitterer, P.H. Mayrhofer, J. Musil, Vacuum 71 (2003) 279.

8 K. Holmberg, A. Matthews, Coatings Tribology, Properties, Techniques and Applications in Surface Engineering, Elsevier, Amsterdam, 1994.

9 A. Matthews in J.S. Burnell-Gray, P.K. Datta (eds.), Surface Engineering Casebook, Woodhead Publishing Ltd., Cambridge, 1996, 23.

10 R.F. Bunshah in R.F. Bunshah, G.M. McGuire, S.M. Rossnagel (eds.), Handbook of Hard Coatings, Noyes Publications, New Jersey, 2001, 4.

11 M.G. Hocking, V. Vasantasree, P.S. Sidky, Metallic and Ceramic Coatings, Wiley, New York, 1989.

12 B. Rother, J. Vetter, Plasmabeschichtungsverfahren und Hartstoffschichten, Deutscher Verlag für Grundstoffindustrie, Leibzig, 1992.

13 W.D. Münz, D. Hofmann, Metalloberfläche, 37/7 (1983) 279.

14 H. Frey, Vakuumbeschichtung 1, Plasmaphysik – Plasmadiagnostik – Analytik, VDI – Verlag, Düsseldorf, 1995.

15 R.H. Haefer, Oberflächen- und Dünnschichttechnologie, Teil 1, Beschichtung von Oberflächen, Springer, Wien, 1987.

16 H. Fischmeister, H.-A. Jehn, Hartstoffschichten zur Verschleißminderung, DGM Informationsgesellschaft Verlag, Oberursel, 1987.

17 B. Window, N. Savvides, J. Vac. Sci. Technol. A 4 (1986) 453.

18 J. Ganz, Metalloberfläche 45 (1991) 11.

19 B. Window, Surf. Coat. Technol. 81 (1996) 92.

20 P.H. Mayerhofer, Materials Science Aspects of Nanocrystalline PVD Hard Coatings, PhD Thesis, University of Leoben, 2001.

21 I. Petrov, F. Adibi, J.E. Greene, W.D. Sproul, W.-D. Münz, J. Vac. Sci. Technol. A10 (1992) 3283.

22 K. Kutschej, P.H. Mayrhofer, M. Kathrein, P. Polcik, R. Tessadri, C. Mitterer, Surf. Coat. Technol. 200 (2005) 2358.

23 C.A. Neugebauer, in L.I. Maissel (eds.), Handbook of Thin Film, McGraw-Hill, New York, 1983.

24 J.E. Greene, in D.T.J. Hurle (eds.), Handbook of Crystal Growth, Vol. 1, Elsevier, Amsterdam, 1993, 640.

25 H.A. Jehn, in W. Gissler, H.A. Jehn (eds.), Advanced Techniques for Surface Engineering, Kluwer Academic Publishers, Dordrecht, 1992, 5.

26 W. Ensinger, Nucl. Instr. Meth. Phys. Res. B 127/128 (1997) 796.

27 J.A. Venables, G.D.T Spiller, M. Hanbücken, Rep. Prog. Phys. 47 (1984) 399.

28 J.A. Thornton, Ann. Rev. Mater. Sci. 7 (1977) 239.

29 B.A. Movchan, A.V. Demchisin, Phys. Metals Metallogr. 28 (1969) 83.

30 J.A. Thornton, J. Vac. Sci. Technol. 11 (1974) 666.

31 R. Messier, A.P. Giri, R.A. Roy, J. Vac. Sci. Technol. A 2 (1984) 500.

32 C.R.M. Grovenor, H.T.G. Hentzell, D.A. Smith, Acta Metall. 32 (1984) 773.

33 P.B. Barna, M. Adamik, in Y. Pauleau, P.B. Barna (eds.), Protective Coatings and Thin Films, Kluwer Academic Publishers, Dordrecht, 1997, 279.

34 D.M. Mattox, J. Vac. Sci. Technol. A 7 (1989) 1105.

35 P. Haasen, Physical Metallurgy, Cambridge University Press, London, 1978.

36 L.B. Freund, S. Suresh, Thin Film Materials, Stress, Defect Formation and Surface Evolution, Cambridge University Press, Cambridge, 2003.

37 E.S. Machlin, Materials Science in Microelectronics, Giro Press, New York, 1995, 157.

38 R.W. Hoffman, Thin Solid Films 34 (1976) 185.

39 W.D. Nix, B.M. Clemens, J. Mater. Res. 14 (1999) 3467.

40 A.L. Shull, F. Spaepen, J. Appl. Phys. 80 (1996) 6243.

41 J.A. Thornton, D.W. Hoffman, J. Vac. Sci. Technol. 18 (1981) 203.

42 F.M. d`Heurle, Metall. Trans. 1 (1970) 725.

43 G.C.A.M. Janssen, Thin Solid Films 515 (2007) 6654.

44 P.R. Guduru, E. Chason, L.B. Freund, J. Mech. Phys. Solids 51 (2003) 2127.

45 W.D. Nix, Metallurg. Trans. A 20 (1988) 2217.

46 A. Brenner, S. Senderoff, Journal of Research 42 (1949) 105.

47 G.G. Stoney, Proc. Roy. Soc. Lond. A82 (1909) 172.

48 J.D. Wilcock, D.S. Campbell, Thin Solid Films 3 (1969) 3.

49 J. Gunnars, U. Wiklund, Mater. Sci. Eng. A336 (2002) 7.

50 I.C. Noyan, J.B. Cohen, Residual Stress, Measurement by Diffraction and Interpretation, Springer, New York, 1987.

51 W.D. Callister, Materials Science and Engineering, Wiley, New York, 2000.

52 W. Schatt, H. Worch, Werkstoffwissenschaft, Deutscher Verlag für Grundstoffindustrie, Stuttgart, 1996.

53 G. Gottstein, Physikalische Grundlagen der Materialkunde, Springer, Berlin, 2001.

54 L. Hultman, Vacuum 57 (2000) 1.

55 H.J. Bargel, G. Schulze, Werkstoffkunde, Springer, Berlin, 2004.

56 E. Hornbogen, Werkstoffe, Springer, Berlin, 2002.

57 N.J. Petch, J. Iron Steel Inst. 174 (1953) 25.

58 C. Mitterer, P.H. Mayrhofer, J. Musil, Vacuum 71 (2003) 279.

59 P.H. Mayrhofer, F. Kunc, J. Musil, C. Mitterer, Thin Solid Films 415 (2002) 151.

60 H. Oettel, R. Wiedemann, S. Preissler, Surf. Coat. Technol. 74 (1995) 273.

61 L. Hultman, C. Mitterer in A. Cavaleiro, J.Th.M. De Hosson (eds.), Nanostructured Coatings, Springer, New York, 2006.

62 J.W. Martin, R.D. Doherty, Stability of Microstructure in Metallic Systems, Cambridge University Press, Cambridge, 1976.

63 H. Gleiter, Acta Mater. 48 (2000) 1.

64 H. Hahn, K.A. Padmanabhan, Nanostructured Materials 6 (1995) 191.

65 A. Cavaleiro, B. Trindade, M.T. Vieira in A. Cavaleiro, J.Th.M. De Hosson (eds.), Nanostructured Coatings, Springer, New York, 2006.

66 S.J. Bull, D.S. Rickerby, Mat. Res. Soc. Symp. Proc. 188 (1990) 337.

67 G.C.A.M. Janssen, A.J. Dammers, V.G.M Sivel, W.R. Wang, Appl. Phys. Lett. 83 (2003) 3287.

68 S.Yu. Grachev, F.D. Tichelaar, G.C.A.M. Janssen, J. Appl. Phys. 97 (2005) 073508.

69 J.-D. Kamminga, Th.H. de Keijser, R. Delhez, E.J. Mittemeijer, J. Appl. Phys. 88 (2000) 6332.

70 M. Bielawski, Surf. Coat. Technol. 200 (2006) 3987.

71 H. Gleiter, Nanostruct. Mater. 6 (1995) 3.

72 S. Veprek, P. Nesladek, A. Niederhofer, F. Glatz, M. Jilek, M. Sima, Surf. Coat. Technol. 108-109 (1998) 138.

73 U. Helmersson, B.O. Johansson, J.-E. Sundgren, H.T.G. Hentzell, P. Billgren, J. Vac. Sci. Technol. A 3 (1985) 308.

74 G.S. Kim, S.Y. Lee, J.H. Hahn, B.Y. Lee, J.G. Han, J.H. Lee, S.Y. Lee, Surf. Coat. Technol. 171 (2003) 83.

75 J.H. Huang, C.H. Ma, H. Chen, Surf. Coat. Technol. 200 (2006) 5937.

76 J.H. Huang, C.H. Ma, H. Chen, Surf. Coat. Technol. 201 (2006) 3199.

77 T.K. Schmidt, T.J. Balk, G. Dehm, E. Arzt, Scripta Mater. 50 (2004) 733.

78 A. Misra, H. Kung, T.E. Mitchell, M. Nastasi, J. Mater. Res. 15 (2000) 756.

79 M.A. Phillips, B.M. Clemens, W.D. Nix, Acta Mater. 51 (2003) 3171.

80 E. Bemporad, M. Sebastiani, C. Pecchio, S. De Rossi, Surf. Coat. Technol. 201 (2006) 2155.

81 M.J. Cordill, N.R. Moody, D.F. Bahr, Acta Mater. 53 (2005) 2555.

82 J.D. Verhoeven, Fundamentals of Physical Metallurgy, Wiley, New York, 1975.

83 J. Musil, Surf. Coat. Technol. 125 (2000) 322.

84 J. Musil, P. Zeman, H. Hruby, P.H. Mayrhofer, Surf. Coat. Technol. 120-121 (1999) 179.

85 P. Zeman, R. Cerstvy, P.H. Mayrhofer, C. Mitterer, J. Musil, Mater. Sci. Eng. A289 (2000) 189.

86 K.P. Andreasen, T. Jensen, J.H. Petersen, J. Chevallier, J. Bottiger, N. Schell, Surf. Coat. Technol. 182 (2004) 268.

87 H.S. Myung, H.M. Lee, L.R. Shaginyan, J.G. Han, Surf. Coat. Technol. 163-164 (2003) 591.

88 Z.G. Lee, S. Miyake, M. Kumagai, H. Saito, Y. Muramatsu, Surf. Coat. Technol. 183 (2004) 62.

89 M. Jirout, J. Musil, Surf. Coat. Technol. 200 (2006) 6792.

90 J. Musil, M. Jirout, Surf. Coat. Technol. 201 (2007) 5148.

91 S. Zhang, D. Sun, Y. Fu, H. Du, Surf. Coat. Technol. 198 (2005) 2.

92 S. Zhang, D. Sun, Y. Fu, Y.T. Pei, J.Th.M. De Hosson, Surf. Coat. Technol. 200 (2005) 1530.

93 A.A. Voevodin, J.S. Zabinski, Thin Solid Films 370 (2000) 223.

94 T. Polcar, T. Kubart, R. Novak, L. Kopecky, P. Siroky, Surf. Coat. Technol. 193 (2005) 192.

95 V. Derflinger, H. Brändle, H. Zimmermann, Surf. Coat. Technol. 113 (1999) 286.

96 A.A. Voevodin, J.P. O`Neill, J.S. Zabinski, Surf. Coat. Technol. 116-119 (1999) 36.

97 S. Carrera, O. Salas, J.J. Moore, A. Woolverton, Surf. Coat. Technol. 167 (2003) 25.

98 J.-P. Hirvonen, J. Koskinen, J.R. Jervis, M. Nastasi, Surf. Coat. Technol. 80 (1996) 139.

99 K.J. Ma, C.L. Chao, D.S. Liu, Y.T. Chen, M.B. Shieh, J. Mater. Proc. Technol. 127 (2002) 182.

100 N. Fateh, G.A. Fontalvo, G. Gassner, C. Mitterer, Wear 262 (2007) 1152.

101 G. Gassner, P.H. Mayrhofer, K. Kutschej, C. Mitterer, M. Kathrein, Tribol. Lett. 17 (2004) 751.

102 K. Kutschej, P.H. Mayrhofer, M. Kathrein, P. Polcik, C. Mitterer, Surf. Coat. Technol. 188-189 (2004) 358.

103 A.A. Voevodin, J.J. Hu, T.A. Fitz, J.S. Zabinski, Surf. Coat. Technol. 146-147 (2001) 351.

104 C. Muratore, J.J. Hu, A.A. Voevodin, Thin Solid Films 515 (2007) 3638.

105 J.J. Hu, C. Muratore, A.A. Voevodin, Compos. Sci. Technol. 67 (2007) 336.

106 C. Muratore, A.A. Voevodin, J.J. Hu, J.S. Zabinski, Wear 261 (2006) 797.

107 C.P. Mulligan, D. Gall, Surf. Coat. Technol. 200 (2005) 1495.

108 K. Abourayak, S. Fayeulle, L. Vincent, C. Ribeiro, A. Cavaleiro, M.T. Vieira, Surf. Coat. Technol. 80 (1996) 171.

109 K. Kutschej, C. Mitterer, C.P. Mulligan, D. Gall, Adv. Eng. Mater. 11 (2006) 1125.

110 J.L. Endrino, J.J. Nainaparampil, J.E. Krzanowski, Scripta Mater. 47 (2002) 613.

111 P.B. Barna in L. Eckertová, T. Ruzicka (eds.), Diagnostics and Applications of Thin Films, Institute of Physics Publishing, Bristol, 1992, 295.

112 Y.Y.Tse, D. Babonneau, A. Michel, G. Abadias, Surf. Coat. Technol. 180-181 (2004) 470.

113 R.S. Howland, M.D. Kirk in C.R. Brundle, C.A. Evans, S. Wilson (eds.), Encyclopedia of Materials Characterization, Manning Publications, Greenwich, 1992, 85.

114 M. Ohring, Materials Science of Thin Films, Academic Press, San Diego, 2002.

115 C. Teichert, Phys. Rep. 365 (2002) 335.

116 W. Gissler, J. Haupt in W. Gissler, H.A. Jehn (eds.), Advanced Techniques for Surface Engineering, Kluwer Academic Publishers, Dordrecht, 1992, 313.

117 V. Valvoda in Y. Pauleau, P.B. Barna (eds.), Protective Coatings and Thin Films, Kluwer Academic Publishers, Dordrecht, 1997, 299.

118 J.I. Langford, J. Appl. Cryst. 11 (1978) 10.

119 B.E. Warren, X-ray Diffraction, Dover Publications, New York, 1990.

120 R. Delhez, Th.H. de Keijser, E.J. Mittemeijer, Z. Fresenius Anal. Chem. 312 (1982) 1.

121 G.B. Harris, Phil. Mag. 43 (1952) 113.

122 K.H. Taube in W. Gissler, H.A. Jehn (eds.), Advanced Techniques for Surface Engineering, Kluwer Academic Publishers, Dordrecht, 1992, 275.

123 W.C. Oliver, G.M. Pharr, J. Mater. Res. 7 (1992) 1564.

124 A.C. Fischer-Cripps, Vacuum 58 (2000) 569.

125 A. Matthews, K. Holmberg in W. Gissler, H.A. Jehn (eds.), Advanced Techniques for Surface Engineering, Kluwer Academic Publishers, Dortrecht, 1992, 295.

126 I.M. Hutchings, Tribology: Friction and Wear of Engineering Materials, Edward Arnold, London, 1992.

127 K.H. Zum Gahr, Microstructure and Wear of Materials, Elsevier, Amsterdam, 1987.

128 M. Moore in D. Rigney (ed.), Fundamentals of Friction and Wear, Edward Arnold, London, 1992, 77.

9 Publications

9.1 List of included papers

[I] Annealing of intrinsic stresses in sputtered TiN films: The role of thickness-dependent gradients of point defect density, H. Köstenbauer, G.A. Fontalvo, M. Kapp, J. Keckes, C. Mitterer, Surface and Coatings Technology 201 (2007) 4777.

[II] Intrinsic stresses and stress relaxation in TiN/Ag multilayer coatings during thermal cycling, H. Köstenbauer, G. A. Fontalvo, J. Keckes, C. Mitterer, Thin Solid Films 516 (2008) 1920.

[III] Structure, stresses and stress relaxation of TiN/Ag nanocomposite films, H. Köstenbauer, G.A. Fontalvo, C. Mitterer, G. Hlawacek, C. Teichert, J. Keckes, Journal of Nanoscience and Nanotechnology, accepted.

[IV] Tribological properties of TiN/Ag nanocomposite coatings, H. Köstenbauer, G.A. Fontalvo, C. Mitterer, J. Keckes, Tribology Letters 30 (2008) 53.

[V] Structure, stresses and stress relaxation of TiN/Cu multilayer and nanocomposite coatings, H. Köstenbauer, A.M. Hofer, G.A. Fontalvo, J. Keckes, C. Mitterer, submitted for publication.

9.2 Publications related to this thesis

[VI] Rapid determination of stress factors and absolute residual stresses in thin films, K.J. Martinschitz, E. Eiper, S. Massl, H. Köstenbauer, R. Daniel, G. Fontalvo, C. Mitterer, J. Keckes, Journal of Applied Crystallography 39 (2006) 777.

[VII] High-temperature residual stresses in thin films characterized by x-ray diffraction substrate curvature method, J. Keckes, E. Eiper, K.J. Martinschitz, H. Köstenbauer, R. Daniel, C. Mitterer, Review of Scientific Instruments 78 (2007) art. no. 036103.

[VIII] Experimental design to minimize errors of stress distributions determined by means of the ion beam layer removal method, S. Massl, H. Köstenbauer, J. Keckes, R. Pippan, Thin Solid Films, submitted.

9.3 My contribution to the included papers

	Conception and Planning*	Experiments	Analysis and Interpretation	Manuscript Preparation*
Paper I	100	90	100	90
Paper II	100	90	100	100
Paper III	100	80	90	90
Paper IV	100	100	100	100
Paper V	100	10	20	100

* Supervision is not included

Paper I

Annealing of intrinsic stresses in sputtered TiN films: The role of thickness-dependent gradients of point defect density

H. Köstenbauer, G.A. Fontalvo, M. Kapp, J. Keckes, C. Mitterer

Surface and Coatings Technology 201 (2007) 4777

Annealing of intrinsic stresses in sputtered TiN films: The role of thickness-dependent gradients of point defect density

Harald Köstenbauer [a], Gerardo A. Fontalvo [a], Marianne Kapp [b,c], Jozef Keckes [b,c], Christian Mitterer [a]

[a] *Department of Physical Metallurgy and Materials Testing, University of Leoben, A-8700 Leoben, Austria*

[b] *Erich Schmid Institute of Materials Science, Austrian Academy of Sciences, A-8700 Leoben, Austria*

[c] *Materials Center Leoben, A-8700 Leoben, Austria*

Abstract

Morphology, structure and thermal behavior of magnetron sputtered TiN thin films with the thickness in the range 100-2900 nm are characterized. The films are thermally cycled and the relationship between film thickness, defect density and the intrinsic stress relaxation is analyzed. The results indicate that the residual stresses in the as-deposited films and the amount of stress relaxation depend decisively on the specific depth gradient of point defects originating from film evolution during growth. The compressive stresses, representing different driving forces and the amount of stress relaxation decrease, while the onset temperature of stress relaxation increases with increasing film thickness.

Keywords: Defects; Reactive sputtering; Titanium nitride; Stress relaxation.

1. Introduction

Understanding residual stresses in hard coatings is a pre-requisite for stress engineering, which could be a powerful tool to increase the lifetime of wear-protecting coatings on e.g. tools or engineering components. These stresses are composed of an intrinsic part resulting from growth defects and a thermal part caused by the mismatch in thermal expansion coefficients of coating and substrate. Previously, stress investigations were conducted on metal films up to 6 µm thickness where tensile residual stresses caused by grain boundary shrinkage obey a power law dependence on coating thickness [1,2]. For sputtered TiN hard coatings above 1 µm thickness a slight stress-thickness dependence was found [3,4]. The

authors related this effect to the formation of point defects like implanted sputter gas atoms, self-interstitials, vacancies, line defects like dislocations [5], where the thickness influence was explained by an increasing coating porosity [4]. According to Kamminga et al. [3], it can be assumed that in sputtered TiN films point defects determine the growth stress. Not only residual stresses but also stress relaxation due to defect annihilation at elevated temperatures (often referred to as recovery), is of vital importance for high-temperature applications. Only a few investigations have been published on stress relaxation of hard coatings [4,6,7], and essentially nothing is known about thickness-dependent stress relaxation at elevated temperatures.

Thus, it is the aim of this work to investigate the effect of thickness-dependent gradients of point defect densities present in sputtered TiN films in the thickness range between 100 and 2900 nm on residual stress and stress relaxation at elevated temperatures.

2. Experimental details

TiN films of thicknesses between 100 and 2900 nm were deposited onto silicon (100) substrates (20×7 mm^2, thicknesses: 200, 300 and 450 µm) by reactive sputtering from a Ti target (∅ 75×6 mm^3) in an Ar+N_2 atmosphere using a laboratory-scale unbalanced DC magnetron sputtering system [8]. There, the substrates are stationary positioned in a distance of about 6 cm above the target. The substrate temperature and the total pressure were 550°C and 0.25 Pa, respectively. To influence the residual stresses in the as-deposited state, different bias voltages U_s were used.

The films were characterized using atomic force microscopy (AFM), transmission electron microscopy (TEM), X-ray diffraction (XRD) in Bragg-Brentano geometry using Cu Kα radiation, and biaxial stress temperature measurements (BSTM). The average surface roughness R_a was also determined using AFM. During BSTM, the films were subjected to a thermal cycle from 25°C to 700°C in vacuum ($p \leq 10^{-3}$ Pa) at a heating and cooling rate of 5 K min^{-1}. Two parallel laser beams were used to measure the variation of substrate curvature during annealing. The biaxial film stress was calculated from the substrate-curvature radius using the modified Stoney equation [9].

3. Results and discussion

3.1. Film structure

All films deposited exhibit a dense structure, as evidenced by TEM cross-sections. The AFM images in Fig. 1 show the effect of film thickness on the surface topography. The phenomena of film growth, as described in the structure-zone models [10,11], show a strong correlation with the resulting surface morphology. Films of 100 nm thickness show a smooth fine-grained surface (Fig. 1(a)) which is typical for equiaxed polycrystals formed in the early film growth stage [12]. With increasing thickness, the surface roughness also increases (Fig. 1(b-c)). This is related to the onset of competitive growth of crystals with preferred growth orientation and increased coarsening [13].

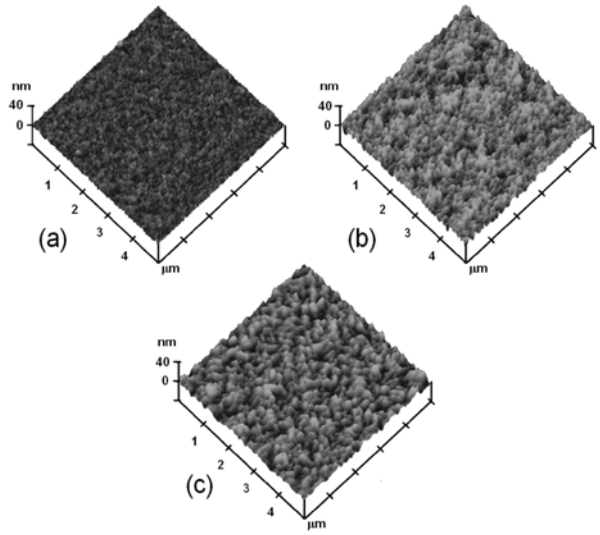

Fig. 1. AFM micrographs of the surface of TiN films grown on Si substrates at a bias voltage Us of -50 V with different thickness t: (a) t=100 nm with a roughness Ra of about 1.1 nm; (b) t=300 nm, Ra~2.5 nm; (c) t=2700 nm, Ra~2.4 nm.

XRD measurements were conducted to calculate the texture coefficient according to Harris [14] for the crystallographic orientations (111), (200) and (220). For the thinner films (i.e. ≤ 300 nm), a random orientation was found. With increasing thickness the texture coefficients for the (111) and (200) peaks are increasing, while the (220) coefficient is decreasing. These observations support the described strong correlation between surface morphology and crystal growth of the films and are also in good agreement with the results obtained by TEM investigations. The broadening of the (111) diffraction peaks expressed by the integral breadth β was used to calculate the size of the coherently diffracting

domains <*D*> in the films [15,16]. The parameter <*D*> corresponds to the average length of crystalline domains in the direction of the diffraction vector and represents the crystalline regions possessing no planar defects [16]. The results in Fig. 2(a) indicate that <*D*> increases for thicker films and agree, thus, well with the AFM results.

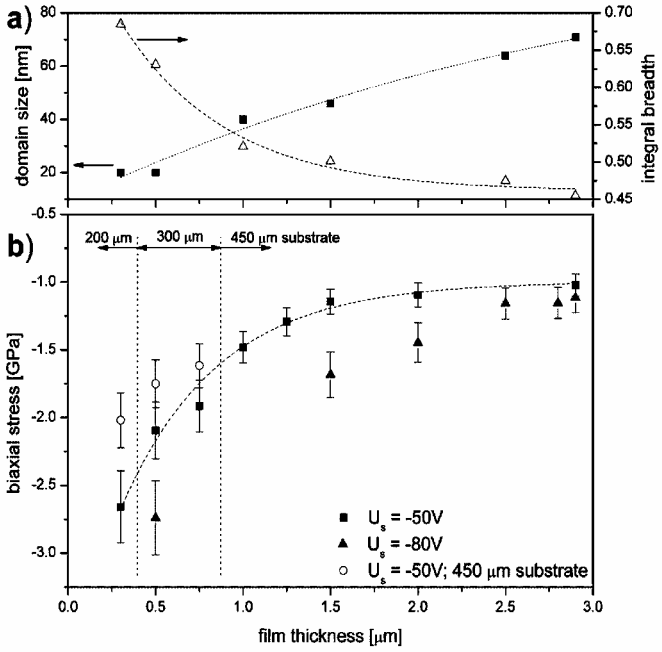

Fig. 2. (a) Integral breadth β of TiN (111) reflections obtained for TiN films deposited on Si substrates at a bias voltage U_s of -50 V vs. film thickness. The results indicate a significant gradient of the size of coherently diffracting domains <D> across the films. (b) As-deposited biaxial stress of TiN films deposited at different bias voltages U_s on Si substrates of different thickness as a function of film thickness. In addition, three films with supercritical substrate thickness (as described in the text) are shown.

3.2. As-deposited film stresses

With varying film thickness, different stress levels are obtained as shown in Fig. 2(b). Using the wafer-curvature method [17], thinner silicon substrates (i.e., 200 and 300 µm) had to be used for the thinner films to obtain sufficient bending. The decreasing compressive biaxial stresses with increasing film thickness for as-deposited films thinner than 1500 nm can be related to the decreasing contribution of point defects formed in the initial growth stage on the total residual stress. This dependence is opposite to findings on sputtered Cr films [1,2] where grain boundary shrinkage due to formation of open-voided grain boundaries during early film growth - and not the defect density - has been discussed as the determining factor. This difference might thus be attributed to differences in the density of the Cr investigated in refs. [1,2] and our TiN films. For thicknesses above 1500

nm, the residual stress decreases only slightly. Kamminga et al. [3,18] found the same dependency for sputtered TiN films. It should be noted that the stress-thickness relation shown in Fig. 2(b) corresponds well to the transition from equiaxed grain growth with high defect densities and thus high compressive stress [7,12] to the competitive crystal growth with reduced stress levels, i.e. the average stress decreases with increasing volume fraction of columnar crystals.

For the higher bias voltage U_s of -80 V, higher compressive stresses are measured. The higher stresses are the result of increasing Ar implantation and increasing defect density [12]. A few stress values obtained for films on thicker Si substrates (450 µm) are added to Fig. 2(b) to show the limit of the modified Stoney equation. When exceeding a critical ratio of substrate to film thickness, in our case approximately 650, the bending of the samples is insufficient to obtain accurate stress values, thus yielding incorrect results.

3.3. Annealing experiments

Figure 3 shows BSTM curves for films deposited at a bias voltage U_s of -50V.

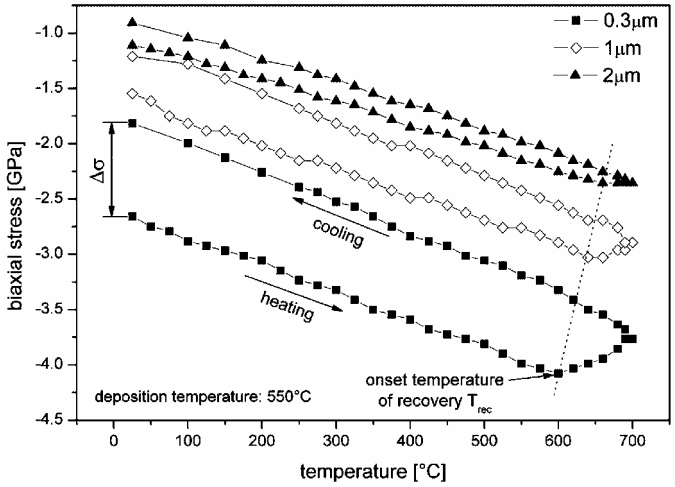

Fig. 3. BSTM cycles of TiN films grown on Si substrates at a bias voltage U_s of -50 V with three different thicknesses up to a maximum temperature of 700°C.

During heating, compressive stresses increase because of the higher thermal expansion coefficient of the film compared to the substrate. A further increase of the temperature results in stress relaxation due to defect annihilation [6,7]. During cooling, the stress-temperature curve shows again linear thermoelastic behavior. No evidence for interdiffusion between Si substrate and the TiN films during these temperature cycles was

found, as described earlier [7]. This is also supported by ref. [5], where no Si diffusion was observed in dense TiN films annealed at 700°C for 20 hours. Thus, interface effects due to interdiffusion can be excluded as a contribution to the bending observed during BSTM. The BSTM curves are shifted to higher compressive stresses with decreasing film thickness (see Fig. 3). In addition, a decrease of the onset temperature of stress relaxation with decreasing film thickness can be observed. This is related to higher average defect densities representing higher driving forces for defect annihilation [6,7] compared to thicker films.

Figure 3 also shows a strong effect of the film thickness, i.e. the compressive stress in the as-deposited state, on the amount of stress relaxation $\Delta\sigma$. Figure 4 presents the dependency between $\Delta\sigma$ and film thickness in more detail. In agreement with the observed structural and stress evolution, a decrease of $\Delta\sigma$ with increasing film thickness can be observed. For films with a thickness above 1500 nm, the $\Delta\sigma$ values reach a plateau. Films deposited at the higher bias voltage U_s of -80 V suffer more pronounced stress relaxation and do not reach this plateau in the investigated film thickness range. This is related to the more intense ion irradiation during film growth and the consequently higher defect density, also for the competitive growth regime [12]. To eliminate the influence of different stress magnitudes in the as-deposited state, the dimensionless ratio of stress relaxation $\Delta\sigma$ to the as-deposited stress is also shown in Fig. 4, yielding the same dependency on film thickness. Thus, the amount of stress relaxation is not only an effect of the magnitude of stresses but is also influenced by the gradient in defect density.

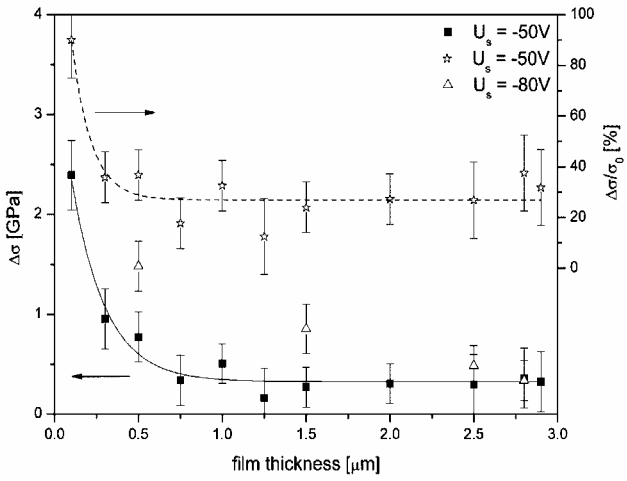

Fig. 4. Amount of stress relaxation $\Delta\sigma$ of TiN films on Si substrates as a function of film thickness for different bias voltages U_s. Displayed are the absolute (solid line) and relative (dashed line) amount of stress relaxation.

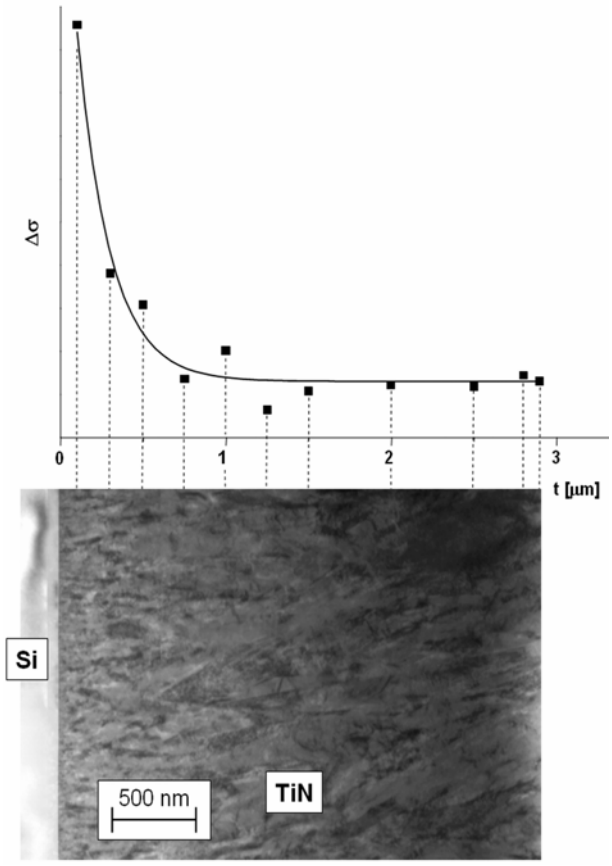

Fig. 5. Bright field TEM cross-sectional micrograph of a 2900 nm thick TiN film grown on a Si substrate at a bias voltage U_s of -50 V, where the structural evolution is related to the amount of stress relaxation $\Delta\sigma$. Every data point represents a film of the respective thickness.

In summary, Fig. 5 shows the correlation between structural evolution and amount of stress relaxation $\Delta\sigma$ on the film thickness. The structural evolution is illustrated by a bright field TEM cross-section of a 2900 nm thick TiN film grown at a bias voltage U_s of -50 V. Every data point displays $\Delta\sigma$ of a film with the respective thickness, with high amounts of stress relaxation for the equiaxed polycrystals obtained in the early state of film growth and lower values for higher film thicknesses.

4. Conclusions

Within this work, correlations between residual stresses and stress relaxation were described for sputtered TiN films of different thicknesses. Residual stress, the amount as well as the onset temperature of stress relaxation for films deposited at different bias voltages were related to a thickness-dependent gradient in point defect density. This

gradient is caused by the structural evolution during film growth and is supposed to be the determining factor for stresses in the coatings. Thinner films, consisting of equiaxed polycrystals formed during early film growth, exhibit high average defect densities which result in high compressive stresses. These high defect densities represent high driving forces for relaxation phenomena; consequently, thinner films show high amounts and low onset temperatures of stress relaxation. In contrast, the competitive growth stage which determines the structure of thicker films results in lower average defect densities. Thus, thicker films show lower compressive stresses and the connected lower driving force leads to higher onset temperatures for stress relaxation.

Acknowledgement

This work was financially supported by the Austrian NANO Initiative via a grant from the Austrian Science Fund FWF (project N401-NAN).

References

[1] G.C.A.M. Janssen, A.J. Dammers, V.G.M Sivel, W.R. Wang, Appl. Phys. Lett. 83 (2003) 3287.

[2] S.Yu. Grachev, F.D. Tichelaar, G.C.A.M. Janssen, J. Appl. Phys. 97 (2005) 073508.

[3] J.-D. Kamminga, Th.H. de Keijser, R. Delhez, E.J. Mittemeijer, J. Appl. Phys. 88 (2000) 6332.

[4] M. Bielawski, Surf. Coat. Technol. 200 (2006) 3987.

[5] L. Hultman, Vacuum 57 (2000) 1.

[6] C. Mitterer, P.H. Mayrhofer, J. Musil, Vacuum 71 (2003) 279.

[7] P.H. Mayrhofer, F. Kunc, J. Musil, C. Mitterer, Thin Solid Films 415 (2002) 151.

[8] K. Kutschej, P.H. Mayrhofer, M. Kathrein, P. Polcik, R. Tessadri, C. Mitterer, Surf. Coat. Technol. 200 (2005) 2358.

[9] J.D. Wilcock, D.S. Campbell, Thin Solid Films 3 (1969) 3.

[10] J.A. Thornton, J. Vac. Sci. Technol. 11 (1974) 5072.

[11] R. Messier, A.P. Giri, R.A. Roy, J. Vac. Sci. Technol. A2 (1984) 500.

[12] I. Petrov, P.B. Barna, L. Hultman, J.E. Greene, J. Vac. Sci. Technol. A21 (2003) 117.

[13] B.W. Karr, I. Petrov, P. Desjardins, D.G. Cahill, J.E. Greene, Surf. Coat. Technol. 94-95 (1997) 403.

[14] G.B. Harris, Phil. Mag. 43 (1952) 113.

[15] B.E. Warren; X-ray diffraction, Dover Publications, New York, 1990.

[16] R. Delhez, Th.H. de Keijser, E.J. Mittemeijer, Z. Fresenius, Anal. Chem. 312 (1982) 1.

[17] P.A. Flinn, D.S. Gardner, W.D. Nix, IEEE Trans. Electron. Devices ED-34 (1987) 689.

[18] J.-D. Kamminga, Th.H. de Keijser, R. Delhez, E.J. Mittemeijer, Thin Solid Films 317 (1998) 169.

Paper II

Intrinsic stresses and stress relaxation in TiN/Ag multilayer coatings during thermal cycling

H. Köstenbauer, G.A. Fontalvo, J. Keckes, C. Mitterer

Thin Solid Films 516 (2008) 1920

Intrinsic stresses and stress relaxation in TiN/Ag multilayer coatings during thermal cycling

H. Köstenbauer [a,b], G. A. Fontalvo [a], J. Keckes [b,c], C. Mitterer [a]

[a] *Department of Physical Metallurgy and Materials Testing, University of Leoben, A-8700 Leoben, Austria*

[b] *Department of Materials Physics, University of Leoben, A-8700 Leoben, Austria*

[c] *Erich Schmid Institute of Materials Science, Austrian Academy of Sciences, A-8700 Leoben, Austria*

Abstract

Morphology, structure and thermal behavior of magnetron sputtered TiN/Ag multilayer thin films deposited at 150°C with a bilayer thickness Λ in the range of 75-600 nm are characterized. The films are thermally cycled and the relationship between bilayer thickness Λ, film structure and stress development is analyzed. The results indicate that the residual stresses in the as-deposited films and the behavior during heating are determined by the morphology and the mechanical properties of the Ag interlayers. The increasing crystallite size of Ag with increasing Λ and the initial porosity in the Ag layer are the reason for significant changes in the stress-temperature behavior. While coatings with Λ = 75 nm behave like a single-phase coating up to 380°C, coatings with higher Λ show a different behavior when exceeding the deposition temperature, which is related to the densification of the Ag layers. During cooling, all coatings exhibit linear thermo-elastic behavior, where the slope of the stress-temperature curves also depends on Λ.

Keywords: Silver; Titanium nitride; Multilayers; Stress

1. Introduction

Understanding residual stresses in multilayer coatings is a pre-requisite for stress engineering and could be a powerful tool to increase the lifetime of wear-protecting coatings on e.g. tools or engineering components. Residual stresses are composed of an intrinsic part resulting from growth defects and a thermal part caused by the mismatch of the thermal expansion coefficients of the different materials in the multilayer system and

between coating and substrate [1]. Metallic interlayers are frequently used to increase adhesion of hard transition metal nitride coatings to the surface of tools or engineering components. Often, these interlayers improve the performance of a hard coating, e.g. TiN with a metallic Ti interlayer [2,3]. Stresses and structure of the hard layer are highly influenced by the soft metallic interlayer, both in bilayer [4-6] and multilayer arrangements [7-9]. An important parameter is the plasticity of the soft layer since higher plasticity usually leads to better adhesion [10]. Besides the relation between the structure arrangement and stress in hard nitride / soft metal multilayers, their thermal stability is of vital importance. Recently, it has been shown that elevated temperatures give rise to stress relaxation due to defect annihilation (often referred to as recovery [11]) and grain coarsening in nitride coatings [12-15]. However, essentially nothing is known about the interaction of stress relaxation, plastic deformation and grain coarsening in metal multilayers consisting of hard and soft layers. To illuminate the role of soft metallic interlayers on residual stress and thermal stability of hard coatings, TiN/Ag multilayers of various bilayer thickness Λ have been studied, serving as model system for a hard nitride / soft metal combination.

2. Experimental details

TiN/Ag multilayer films were deposited onto Si (100) substrates with a thickness of 200 µm and austenitic stainless steel substrates with a thickness of 250 µm. The substrates were ultrasonically pre-cleaned in acetone and ethanol and thermally cleaned at 750°C before deposition. The total thickness of the multilayer was kept constant at about 600 nm, while the bilayer thickness Λ varied from 75 to 600 nm, with the ratio of Ag to TiN layer thickness held constant at about 1:2. The layers were deposited by unbalanced DC magnetron sputtering from one Ag and two Ti targets (∅ 50.8×6.35 mm^3) by sputtering in Ar in case of Ag and reactive sputtering in $Ar+N_2$ in case of TiN. In all cases, the layer sequence started with an Ag layer grown on the substrate materials and ended with a TiN top layer. The substrates were positioned parallel to the targets in a distance of 7 cm and rotated with a rotation speed of approximately 10 rpm during deposition. The substrate temperature T_D and the total pressure were 150°C and 0.25 Pa, respectively. All coatings were deposited at floating potential.

The films were characterized using scanning electron microscopy (SEM) (10 kV), transmission electron microscopy (TEM) (200 kV) of film cross-sections prepared by focused ion beam (Milling: 30 kV / 20 nA Ion Beam Current – 0,10 nA IBC, Final Milling 5 kV / 70 pA IBC), X-ray diffraction (XRD) in Bragg-Brentano geometry using Cu Kα radiation, and biaxial stress temperature measurements (BSTM). During BSTM, the films were subjected to a thermal cycle from 25 to 400 and 500°C in vacuum ($p \leq 10^{-3}$ Pa) at a heating and cooling rate of 5 K min^{-1}. Two parallel laser beams were used to measure the variation of the substrate curvature during annealing. The biaxial film stress was calculated from the substrate-curvature radius using the modified Stoney equation [16].

3. Results and discussion

3.1 Film structure

Fig. 1 shows the SEM cross-section of the coating with bilayer thickness Λ = 150 nm on Si (100) substrates. The coating is very rough, and the comparison of the SEM micrographs of all coatings deposited indicates that roughness increases with increasing Λ. The rough surface originates presumably from the Ag interlayers, since a single TiN layer exhibits a smooth surface when deposited using the same deposition parameters [15]. Similar findings have been reported by Tse et al. where the interface roughness of TiN/Ag multilayer coatings was discussed [17].

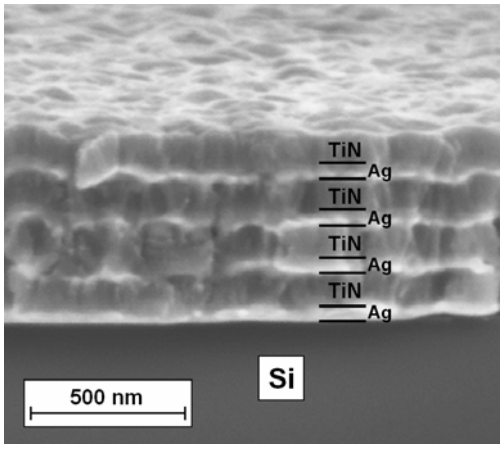

Fig. 1. SEM cross-sectional micrograph of a TiN/Ag multilayer with bilayer thicknesses Λ = 150 nm.

Fig. 2 shows XRD patterns for the multilayer coating with Λ = 75 nm on Si (100) and austenitic stainless steel substrate. In case of the Si substrate, the TiN and Ag peaks at

lower diffraction angles are separated with the exception of the overlapping Ag (311) and TiN (222) peaks. In case of the steel substrate, the TiN (311) peak is overlapped by a substrate peak. Therefore, only the peaks of the (111), (200) and (220) orientations were used for further structural investigations. Texture coefficients were calculated for the crystallographic orientations (111), (200) and (220) according to Harris [18]. The TiN and the Ag layers of all coatings show a preferred (111) orientation, which is more pronounced for multilayer coatings deposited on Si (100) than on austenitic stainless steel, and is independent from the bilayer thickness. Dobrev reports that sputtered Ag coatings tend to grow with a (111) orientation, and this orientation changes to (110) with more intense ion bombardment [19]. However, according to Tse et al. there is no crystallographic growth correlation between TiN and Ag [17] which could lead to a preferred texture in such thin polycrystalline films. TiN itself shows a preferred (111) orientation when deposited under weak ion bombardment conditions [20,21]. In a previous study [15], the authors found that competitive growth for TiN coatings deposited under the same conditions as in the present study starts for a film thickness of about 500 nm, giving rise to formation of highly textured columnar crystals. Since our films are essentially composed of equiaxed polycrystals which are typically formed in the early film growth stage [22], we assume that there is no direct correlation between the orientations of TiN and Ag layers for the investigated bilayer thickness range.

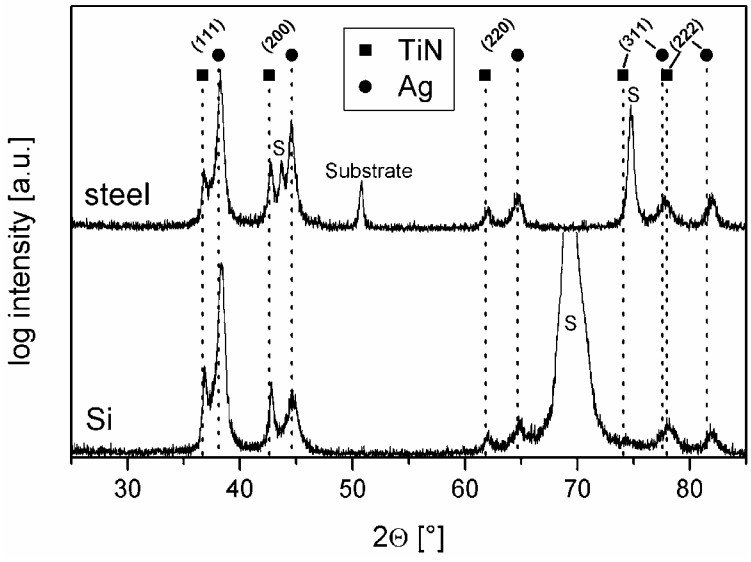

Fig. 2. XRD patterns of the multilayer with Λ = 75 nm on Si (100) and austenitic stainless steel substrates. The position of the substrate peaks is marked with an S.

The broadening of the (111) diffraction peaks, expressed by the integral breadth β, was used to calculate the size of the coherently diffracting domains <*D*> in the films [23,24]. The parameter <*D*> corresponds to the average length of crystalline domains in the direction of the diffraction vector and represents the crystalline regions possessing no planar defects [24]. The results in Fig. 3 indicate that <*D*> increases with increasing bilayer thickness, and thus, agree well with the structure zone models [25,26]. Although the Ag layer is approximately half as thick as the TiN layer, the Ag domain size is significantly larger and in the range of the film thickness. It can be assumed that the formation of these big crystallites is the reason for the observed high surface roughness.

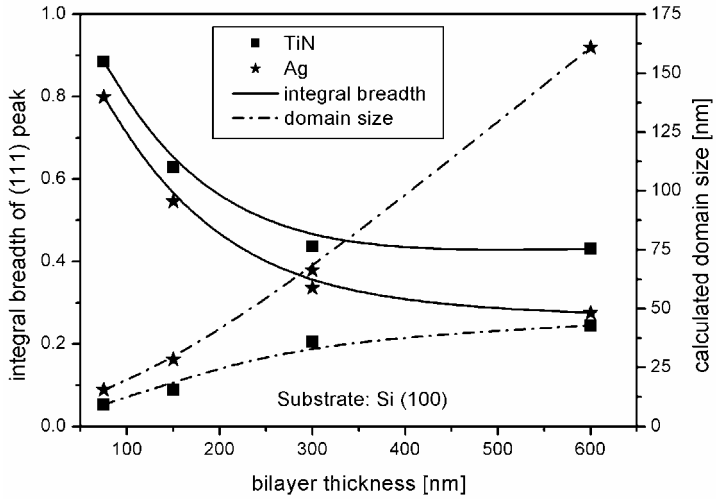

Fig. 3. Integral breadth β of TiN and Ag (111) reflections obtained for TiN/Ag multilayers deposited on Si substrates vs. bilayer thickness Λ.

The TEM cross-sections shown in Fig. 4 display the differences between the as-deposited (Fig. 4a) and annealed multilayer coating (Fig. 4b) with Λ = 75 nm. Both samples exhibit a well defined layered structure with TiN layers of constant thickness of about 50 nm before and after annealing at 500°C. However, the morphology of the Ag layers changed significantly. In the as-deposited state, a high density of pores can be observed which results in a high overall roughness of the interfaces as well as coating surface. Additionally, the Ag layers show droplet-shaped crystallites which also increase roughness. According to Barna [27], it is assumed that these droplets are formed by liquid-like coalescence of the high-mobility Ag [1]. Both, porosity and crystallite size increase with increasing Λ.

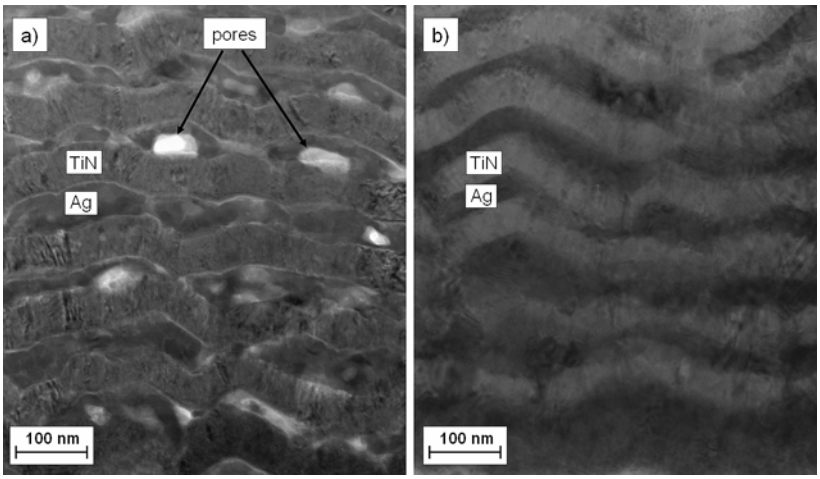

Fig. 4. Bright-field TEM cross-sectional micrographs of multilayer coatings with Λ = 75 nm in the (a) as-deposited state and (b) after annealing at 500°C.

After annealing, the multilayer exhibits a dense structure (see Fig. 4b). The droplet-shaped Ag crystallites and the high porosity and interface roughness of the Ag layers are replaced by dense Ag layers with a more homogeneous thickness, due to sintering phenomena like coalescence of the droplet-shaped crystallites and the out-annealing of pores. Diffusion effects through the TiN layers can be excluded because of their dense structure. Therefore, sintering only occurs in the individual Ag layers.

3.2 Stresses and stress development

Fig. 5 shows BSTM curves for films with different bilayer thickness Λ deposited on Si (100) and measured to a maximum temperature of 400°C. All films investigated show total tensile stresses in the as-deposited state, which is obviously an effect of the Ag layer constrained between the TiN layers showing compressive stresses [15] and its high thermal expansion coefficient. The tensile stresses in the as-deposited state increase with decreasing bilayer thickness. This should be attributable to an increased strength of the Ag layers with decreasing layer thickness, giving rise to hardening effects [28], and the consequently reduced possibility for stress relaxation. During heating, these tensile stresses decrease because of the higher average thermal expansion coefficient of the film compared to the substrate, and due to stress relaxation as a result of defect annihilation [13,14]. Above the deposition temperature T_D, the slope of the BSTM curve changes, and the behavior seems to be determined by the bilayer thickness. The coating with Λ = 300 nm

shows an increase in tensile stresses above T_D, after reaching a zero stress level. For the multilayer with Λ = 75 nm, there is a further decrease in stresses above T_D until it reaches a value close to zero at about 380°C. The BSTM heating curve of the multilayer with Λ = 150 nm lies between the two other curves, and the biaxial stresses remain constant at ~100 MPa from T_D up to 400°C. Annealing up to 500°C (Fig. 6) shows that the biaxial stresses of both coatings, with Λ = 75 nm and Λ = 300 nm, reach a plateau at approximately 380°C, which is unaffected by a further increase of annealing temperature up to 500°C.

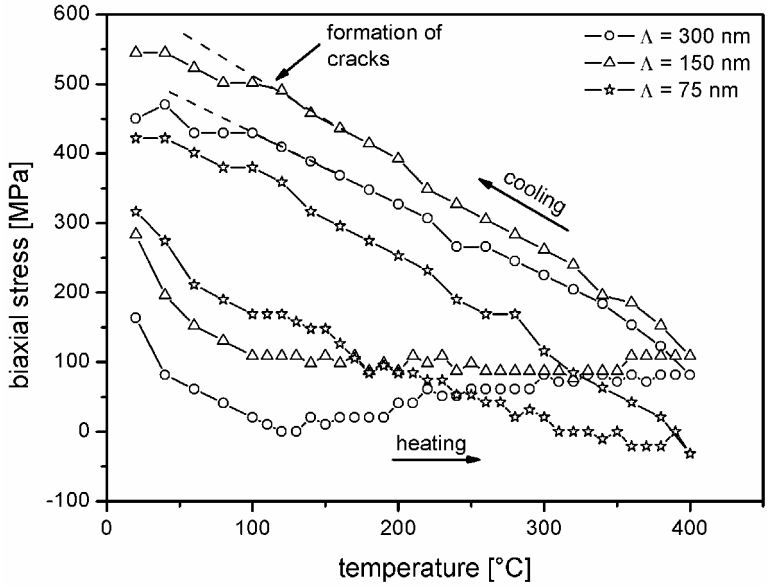

Fig. 5. BSTM cycles from room temperature up to 400°C of TiN/Ag multilayer films grown at 150°C on Si (100) substrates with different bilayer thickness Λ.

The change in slope of the BSTM curve above deposition temperature is related to the observed densification of the Ag interlayers, resulting in shrinkage and, consequently, tensile stresses. Because the thicker Ag layers show higher porosity compared to thinner layers, as stated in section 3.1, the induced total tensile stresses in the multilayer with Λ = 300 nm are higher than for coatings with lower Λ and even increase slightly with further increase of annealing temperature (cf. Fig. 6). For the multilayer with Λ = 75 nm, which has lower porosity and higher strength, densification of the Ag layer induces only a slight decrease in the slope of the BSTM curve till a constant stress level is reached.

The biaxial stresses of all multilayers reach a plateau at about 380°C. This phenomenon should be related to the fact that any further stresses which appear above this temperature are relieved by plastic deformation of the Ag interlayers. The slightly compressive stress

level of the multilayer with Λ = 75 nm could be attributed to the high strength and low porosity of the Ag interlayer, and the thus higher contribution of compressive stress of the TiN layers [15] to the total stress.

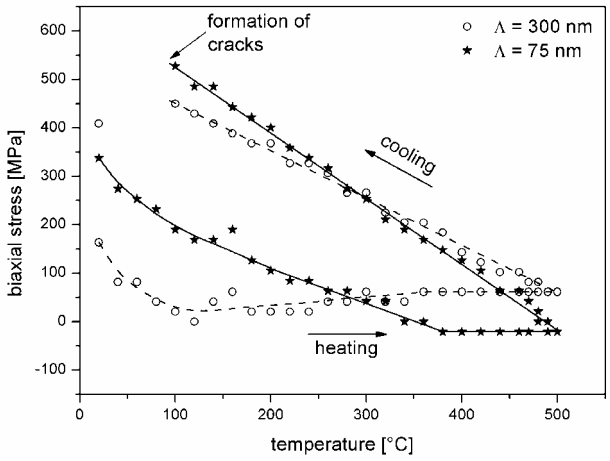

Fig. 6. BSTM cycles from room temperature up to 500°C of TiN/Ag multilayer films grown at 150°C on Si (100) substrates with different bilayer thickness Λ.

During cooling, the BSTM curves show a linear thermo-elastic behavior until 100°C with Λ–dependant slopes, with steeper slopes the lower Λ is (see Figs. 5 and 6). The linear thermo-elastic behavior originates from the now densified coating structure. Differences in slope of the cooling segments result from changes in the elastic modulus caused by the initially different porosities of the Ag layers and by the improved strength and thus less pronounced stress relaxation with decreasing Λ [28, 29]. For temperatures below 100°C, micro-cracks are formed and governing the BSTM curves.

4. Conclusions

Within this work, correlations between film structure and stress development during thermal cycling were described for sputtered TiN/Ag multilayer films of different bilayer thickness Λ. SEM and TEM investigations revealed a porous nature of the Ag layers with droplet-shaped crystallites corresponding in size to the layer thickness, where layer porosity and consequently also coating roughness increase with increasing Λ.

Above a critical annealing temperature sintering takes place, yielding densification of the Ag layers. The more pronounced this densification is, the more tensile stresses are induced

affecting the slope of the biaxial stress temperature curves above deposition temperature. Biaxial stresses of all coatings investigated reach a plateau at about 380°C, since any further stress which appears above this temperature is relieved by plastic deformation of the Ag interlayers. After densification, coatings exhibit a linear thermo-elastic behavior during cooling. The sintering of the Ag layers is overlapped by recovery effects within the TiN layers, but the determining factor in the stress-temperature behavior of TiN/Ag multilayer coatings is the densification of the Ag layers.

Acknowledgement

This work was financially supported by the Austrian NANO Initiative via a grant from the Austrian Science Fund FWF (project N401-NAN). The authors would like to thank Stefan Massl for the SEM investigations.

References

[1] F. Spaepen, Acta Mater. 48 (2000) 31

[2] U. Helmersson, B.O. Johansson, J.-E. Sundgren, H.T.G. Hentzell, P. Billgren, J. Vac. Sci. Technol. A 3 (1985) 308.

[3] G.S. Kim, S.Y. Lee, J.H. Hahn, B.Y. Lee, J.G. Han, J.H. Lee, S.Y. Lee, Surf. Coat. Technol. 171 (2003) 83.

[4] J.H. Huang, C.H. Ma, H. Chen, Surf. Coat. Technol. 200 (2006) 5937.

[5] J.H. Huang, C.H. Ma, H. Chen, Surf. Coat. Technol. 201 (2006) 3199.

[6] T.K. Schmidt, T.J. Balk, G. Dehm, E. Arzt, Scripta Mater. 50 (2004) 733.

[7] A. Misra, H. Kung, T.E. Mitchell, M. Nastasi, J. Mater. Res. 15 (2000) 756.

[8] M.A. Phillips, B.M. Clemens, W.D. Nix, Acta Mater. 51 (2003) 3171.

[9] E. Bemporad, M. Sebastiani, C. Pecchio, S. De Rossi, Surf. Coat. Technol. 201 (2006) 2155.

[10] M.J. Cordill, N.R. Moody, D.F. Bahr, Acta Mater. 53 (2005) 2555.

[11] J.D. Verhoeven, Fundamentals of Physical Metallurgy, Wiley, New York, 1975

[12] M. Bielawski, Surf. Coat. Technol. 200 (2006) 3987.

[13] C. Mitterer, P.H. Mayrhofer, J. Musil, Vacuum 71 (2003) 279.

[14] P.H. Mayrhofer, F. Kunc, J. Musil, C. Mitterer, Thin Solid Films 415 (2002) 151.

[15] H. Köstenbauer, G.A. Fontalvo, M. Kapp, J. Keckes, C. Mitterer, Surf. Coat. Technol 201 (2007) 4777.

[16] J.D. Wilcock, D.S. Campbell, Thin Solid Films 3 (1969) 3.

[17] Y.Y.Tse, D. Babonneau, A. Michel, G. Abadias, Surf. Coat. Technol. 180-181 (2004) 470.

[18] G.B. Harris, Phil. Mag. 43 (1952) 113.

[19] D. Dobrev, Thin Solid Films 92 (1982) 41.

[20] J.E. Greene, J.-E. Sundgren, L. Hultman, I. Petrov, D.B. Bergstrom, Appl. Phys. Lett. 67 (1995) 2928.

[21] C. Mitterer, P.H. Mayrhofer, E. Kelesoglu, R. Wiedemann, H. Oettel, Z. Metallkde. 90 (1999) 602.

[22] I. Petrov, P.B. Barna, L. Hultman, J.E. Greene, J. Vac. Sci. Technol. A 21 (2003) 117.

[23] B.E. Warren; X-ray diffraction, Dover Publications, New York, 1990.

[24] R. Delhez, Th.H. de Keijser, E.J. Mittemeijer, Z. Fresenius Anal. Chem. 312 (1982) 1.

[25] J.A. Thornton, J. Vac. Sci. Technol. 11 (1974) 5072.

[26] R. Messier, A.P. Giri, R.A. Roy, J. Vac. Sci. Technol. A 2 (1984) 500.

[27] P.B. Barna, in: L. Eckertová, T. Ruzicka (Eds.), Diagnostics and Applications of Thin Films, Institute of Physics Publishing, Bristol, 1992, p. 295.

[28] E. Arzt, Acta Mater. 46 (1998) 5611

[29] J.S. Koehler, Phys. Rev. B 2 (1970) 547.

Paper III

Structure, stresses and stress relaxation of TiN/Ag nanocomposite films

H. Köstenbauer, G.A. Fontalvo, C. Mitterer, G. Hlawacek, C. Teichert, J. Keckes

Journal of Nanoscience and Nanotechnology, accepted Manuscript

Structure, stresses and stress relaxation of TiN/Ag nanocomposite films

H. Köstenbauer [a,b], G. A. Fontalvo [a], C. Mitterer [a], G. Hlawacek [c], C. Teichert [c], J. Keckes [b,d]

[a] *Department of Physical Metallurgy and Materials Testing, University of Leoben, A-8700 Leoben, Austria*

[b] *Department of Materials Physics, University of Leoben, A-8700 Leoben, Austria*

[c] *Institute of Physics, University of Leoben, A-8700 Leoben, Austria*

[d] *Erich Schmid Institute of Materials Science, Austrian Academy of Sciences, A-8700 Leoben, Austria*

Abstract

Morphology, structure and thermal behavior of magnetron sputtered TiN/Ag nanocomposite thin films deposited at 150°C with an Ag content in the range of 7 to 45 at.% were characterized. The films were thermally cycled and the relationship between Ag content, film structure and stress development is analyzed. The results indicate that the residual stresses in as-deposited films and the behavior during heating are determined by the film structure and the plastic deformation of the Ag phase. The increasing plastic deformation with increasing Ag content causes significant changes in the stress-temperature behavior. While films with low Ag content show a plateau in compressive stress from deposition temperature up to 280°C followed by stress relaxation, films with higher Ag content exhibit a zero stress level from deposition temperature up to the maximum annealing temperature. During cooling, all films exhibit linear thermo-elastic behavior, where the slope of the stress-temperature curves also depends on the Ag content.

Keywords: Sputtering; Silver; Titanium nitride; Nanocomposite; Stress relaxation

1. Introduction

Understanding residual stresses in hard multiphase coatings is a pre-requisite for stress engineering and could be a powerful tool to increase the lifetime of wear-protecting coatings on e.g. tools or engineering components. Residual stresses are composed of an

intrinsic part resulting from growth defects and a thermal part caused by the mismatch of the thermal expansion coefficients of the different phases in the coating and between coating and substrate[1].

The combination of a soft and a hard material is frequently used to improve coating performance. For example, soft metallic interlayers can be used to increase adhesion, and thus, lifetime of a wear-resistant coating[2]. There, an essential parameter is the plasticity of the metallic phase [3]. It has been also shown that a low fraction of a metallic component which segregates at the grain boundaries of a nitride can be used to realize hard and superhard coatings[4] like ZrN/Cu[5,6] or TiN/Cu[7-9]. Furthermore, high amounts of a soft metallic phase can be used to improve tribological properties for room temperature as well as high temperature applications. For this purpose, preferably Au and Ag have been suggested in combination with oxides[10-12], nitrides[13-15] and carbides[16] to reduce friction and/or wear. The addition of a soft phase offers also the possibility to improve coating toughness by influencing e.g. stresses and structure[17-20]. Not only residual stresses are of vital importance for high-temperature applications of wear-resistant coatings but also stress relaxation due to defect annihilation (often referred to as recovery[21]), in particular for hard nitrides, and plastic deformation as well as recrystallisation of the metal at elevated temperatures.

A few investigations have been published on stress relaxation of hard coatings[22-25], but only very limited information exists about stress relaxation in hard nitride / soft metal nanocomposite coatings at elevated temperatures as function of metal content. Thus, it is the aim of this work to investigate the effect of the metal content of magnetron sputtered TiN/Ag nanocomposite films on structure and residual stresses as well as stress relaxation at elevated temperatures.

2. Experimental details

TiN/Ag nanocomposite films were deposited onto 300 µm thick Si (100) substrates which were ultrasonically pre-cleaned in acetone and ethanol and plasma etched before deposition. The total thickness of the films was kept constant at about 3 µm. The layers were deposited by unbalanced DC reactive magnetron sputtering from one Ag and two Ti targets (∅ 50.8×6.35 mm), all three focused to the substrate holder, in an $Ar+N_2$ atmosphere. The Ag content in the film was varied by changing the sputtering power at the

Ag target. Six different Ag target power settings were chosen to deposit films with about 7, 15, 22, 30, 38 and 45 at.% Ag. The substrates were positioned at a distance of 7 cm from the center of the target cluster and rotated with a speed of approximately 10 rpm during deposition to obtain uniform films. The substrate temperature and the total pressure were 150°C and 0.25 Pa, respectively. All films were deposited at floating potential. To improve adhesion, a 50 nm thick TiN interlayer was deposited at a temperature of 450°C directly after substrate etching. Then, the substrates were cooled down to 150°C to deposit the nanocomposite without excessive Ag diffusion.

The films were characterized using atomic force microscopy (AFM) with conventional Si-tips in tapping mode, scanning electron microscopy (SEM), transmission electron microscopy (TEM) and scanning transmission electron microscopy (STEM) of cross-sections, energy-dispersive X-ray (EDX) analysis, X-ray diffraction (XRD) in Bragg-Brentano geometry using Cu Kα radiation and biaxial stress-temperature measurements (BSTM). During BSTM, the films were subjected to a thermal cycle from 25 to 450°C in vacuum ($p \leq 10^{-3}$ Pa) at a heating and cooling rate of 5 K min^{-1}. Two parallel laser beams were used to measure the variation of the substrate curvature during annealing. The biaxial film stress was calculated from the substrate-curvature radius using the modified Stoney equation[26].

3. Results and discussion

3.1 Film structure

Figs. 1a and b show representative AFM images of samples containing 7 and 45 at.% Ag, respectively. They allow for comparing qualitatively the morphology of the two different films. On both surfaces, small round structures of rather uniform size and shape are visible. Statistical surface roughness analysis yields a quantitative description of the surface morphology. The height-height correlation function (HHCF) allows to characterize surfaces not only by their vertical roughness but also in the lateral direction[27,28]. The root mean square (rms) roughness of the film containing 7 at.% Ag is 4.7 ± 0.2 nm. This is significantly lower than for the film containing 45 at.% Ag with an rms-roughness of 7.6 ± 0.6 nm. The lateral correlation length which is a measure for the lateral height undulations is for 7 at.% Ag film slightly larger (60 ± 4 nm) than for the 45 at.% Ag film (54 ± 5 nm).[29] Obviously, the film containing 45 at.% of Ag is rougher than the one with a lower

silver content of 7 at.% although the lateral feature size is slightly smaller. This corresponds well with the impression the SEM images yield of the surfaces of the film with 7 at.% Ag (Fig. 1c) and 45 at.% Ag (Fig. 1d). A watershed algorithm[30] was used to measure the grain size from the AFM data. The average grain radius obtained from a Gaussian fit to the grain radius distribution of four individual images is 50 ± 20 nm for the film containing 7 at.% Ag and 30 ± 20 nm for the 45 at.% Ag film. These values are in good agreement with the results obtained from the HHCF, as the smoother surface exhibits larger grains.

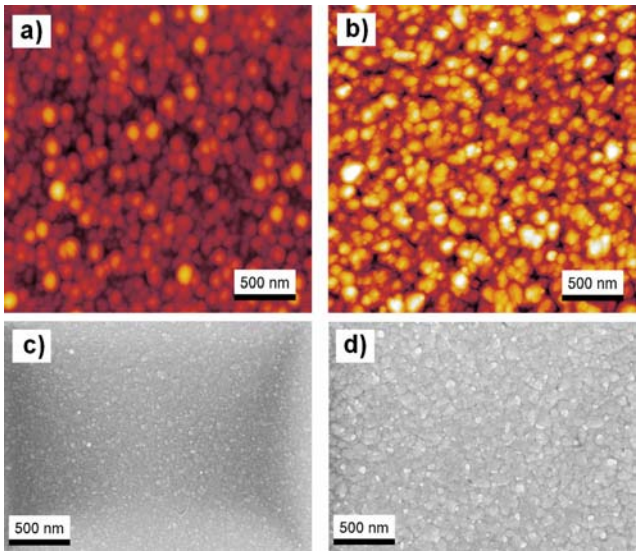

Fig. 1. AFM images of the surface of TiN/Ag nanocomposite films with a) 7 at.% Ag and b) 45 at.% Ag (z-scale 40 nm). Corresponding SEM micrographs of the surface: c) 7 at.% Ag, d) 45 at.%.

Fig. 2 shows XRD patterns of the TiN/Ag films with different Ag contents deposited on Si (100) substrates. The TiN and Ag peaks of the different orientations overlap and are increasingly shifted from the TiN towards the Ag standard position with increasing Ag content. Despite the overlapping peaks, a dual-phase structure with separated TiN and Ag phases is formed, as evidenced by the insert in Fig. 2 for the film with 15 at.% Ag. The broadening of the (111) diffraction peaks, expressed by the integral breadth β, was used to calculate the size of the coherently diffracting domains $\langle D \rangle$ in the films[31,32]. The parameter $\langle D \rangle$ corresponds to the average length of crystalline domains in the direction of the diffraction vector and represents the crystalline regions possessing no planar defects[32].

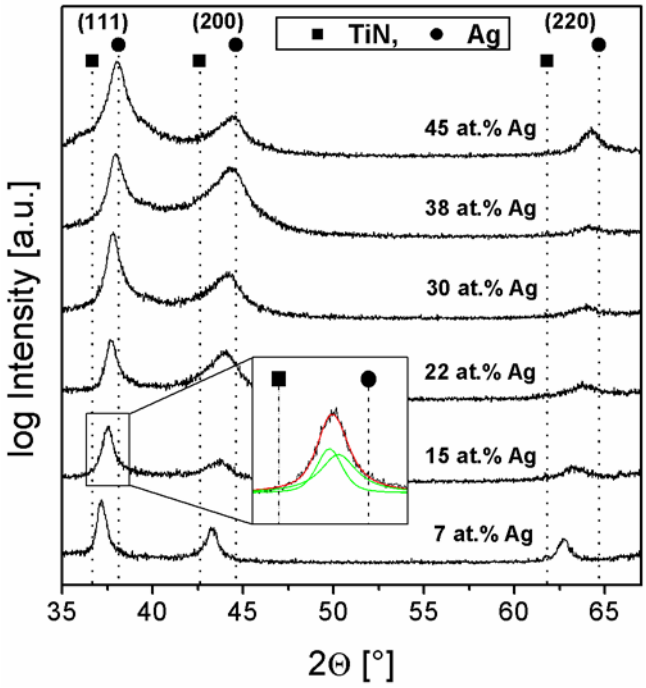

Fig. 2. XRD patterns of TiN/Ag nanocomposite films with increasing Ag content on Si (100) substrates.

The results in Fig. 3 indicate that for all films with an Ag content exceeding 7 at.% Ag, a domain size <*D*> of ~6 nm is obtained, whereas the film with 7 at.% Ag yields a significantly higher value of ~20 nm. During annealing at 350°C, the domain size of all samples does not change significantly.

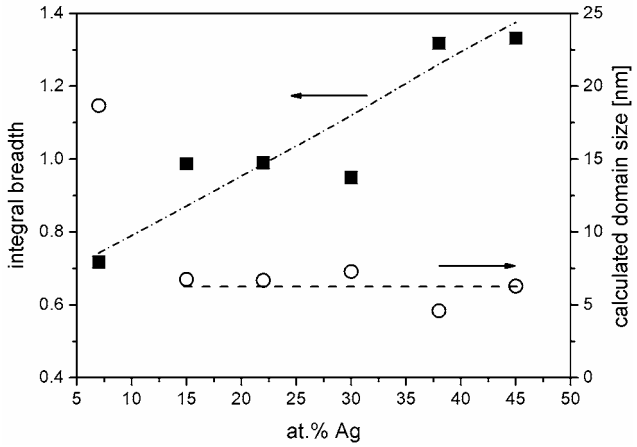

Fig. 3. Integral breadth β of (111) reflections of the Ag phase obtained from TiN/Ag nanocomposites deposited on Si (100) substrates vs. Ag content.

To shine more light onto the film structure, TEM investigations were conducted on cross-sections of the films with 7 at.% and 45 at.% Ag. Fig. 4a shows the HAADF (high-angle

annular dark field) STEM micrograph (Z-contrast) of the film with 45 at.% Ag. This film exhibits a columnar structure with a column width of ~100 nm. Bright spots can be seen inside the columns with diameters of ~30 nm down to ~3 nm representing Ag particles as confirmed by EDX measurements. These Ag particles are also present on the surface[11,12] and they predominantly influence the quantitative data obtained by AFM data. This is the reason for the significant difference between the grain size obtained by AFM and the column width measured by STEM. At higher magnification (Fig. 4b), a layered structure with a layer distance of ~4 nm can be observed inside the columns. This structure consists of Ag-poor and Ag-rich layers, as confirmed by EDX measurements, which are the result of the sample rotation during deposition.

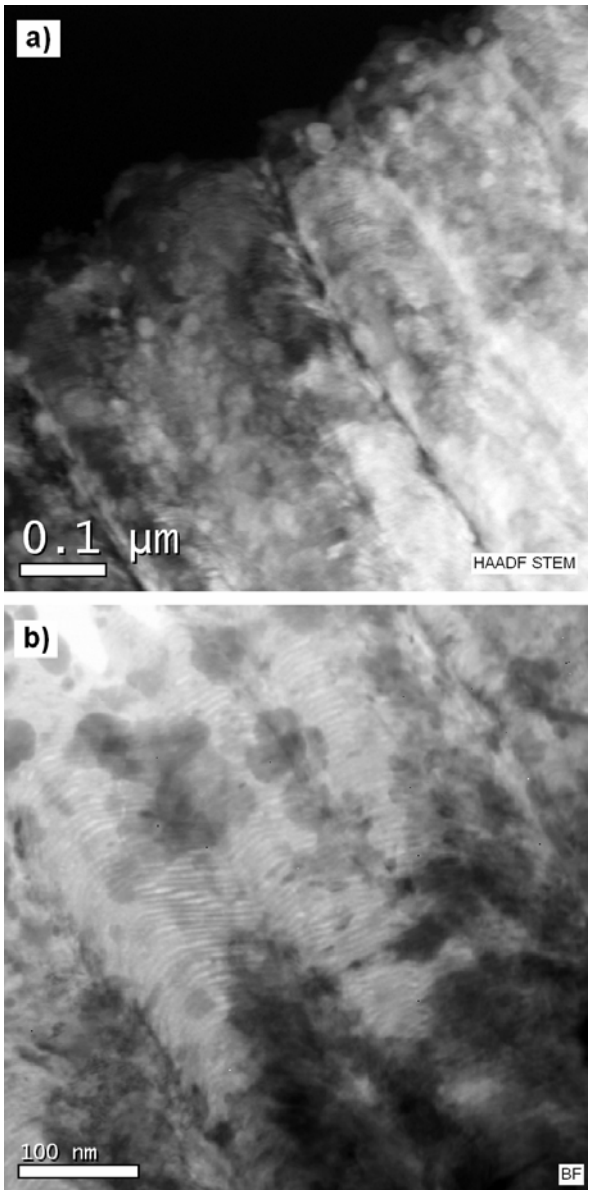

Fig. 4. TEM micrographs of the film with 45 at.% Ag. a) HAADF STEM micrograph, b) TEM bright-field micrograph with higher magnification.

Fig. 5a shows the HAADF STEM micrograph of the film with 7 at.% Ag. This film exhibits also a columnar structure with a column width of ~80 nm, which roughly corresponds to the grain size obtained by AFM measurements. Inside the columns, again Ag particles with diameters of ~50 nm down to ~3 nm can be seen.

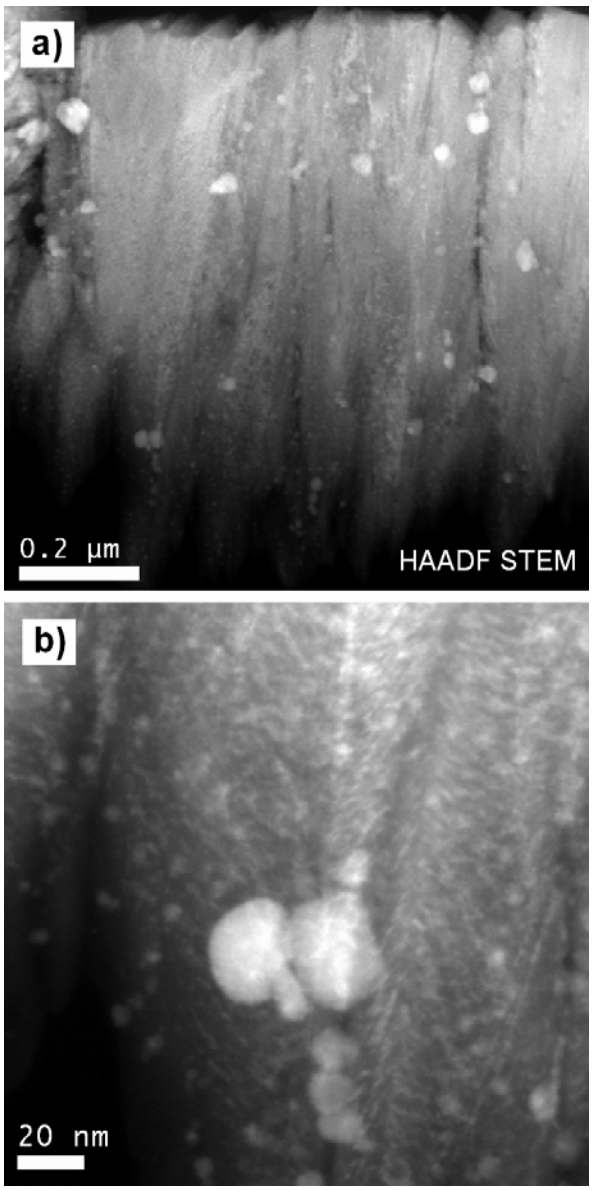

Fig. 5. TEM micrographs of the film with 7 at.% Ag. a) HAADF STEM micrograph, b) HAADF STEM micrograph with higher magnification.

At higher magnification (Fig. 5b), only a slight indication of a layered structure like in the film with 45 at.% Ag is visible. In this case, the Ag-rich layers are not continuous and very thin. The absence of continuous layers and the concentration of the Ag in the observed

particles are assumed to be the reason for the significantly higher domain size obtained by XRD measurements. For higher Ag contents, the obtained domain size corresponds well to the investigated layer thickness within the columns. It can be assumed that the continuous Ag-rich layers are the reason for the small domain size calculated for higher Ag contents. It has to be mentioned that in the case of the films investigated, none of the methods (AFM and XRD) gives accurate values for the grain size due to the complex dual-phase film structure.

3.2 Stress-temperature behavior

In a previous investigation it has been shown that TiN films exhibit a linear thermo-elastic behavior during heating up to ~50°C above deposition temperature[25]. Thus, it should be mentioned that the 50 nm thick TiN interlayer has a small contribution of compressive stress to the overall stress measured during a BSTM cycle. However, this contribution is overruled by the stresses originated from the nanocomposite where additional measurements showed no significant differences in the stress-temperature behavior of films with and without interlayer.

Fig. 6 shows BSTM curves for the films with 7 and 45 at.% Ag deposited on Si (100) substrates. All films investigated show tensile stresses in the as-deposited state which are obviously an effect of the high thermal expansion coefficient of Ag and the columnar film growth. These tensile stresses in the as-deposited state decrease with increasing Ag content. While the films with 7, 15 and 22 at.% Ag show tensile stresses of ~250 MPa ± 20 MPa, the films with 30, 38 and 45 at.% Ag exhibit tensile stresses of ~130 MPa ± 20 MPa. It can be assumed that the strength of the films decreases with increasing Ag content. Thus, the soft Ag phase underlies already plastic deformation during cooling down from deposition temperature. During heating, the tensile stresses decrease because of the higher average thermal expansion coefficient of the film compared to the substrate, and due to stress relaxation as a result of defect annihilation[23,24]. Above the deposition temperature, the slope of the BSTM curve changes and the behavior seems to be determined by the soft Ag phase. The film with 45 at.% Ag reaches a zero stress level which remains constant up to the maximum temperature investigated. This should be related to the fact that any further stress which appears above the deposition temperature is relieved by plastic deformation of the Ag phase. For the film with 7 at.% Ag, there is a plateau in the stress-temperature curve at ~-50 MPa from deposition temperature up to ~280°C. This is due to

the not sufficiently high Ag content in the film to relieve all stresses by plastic deformation. Above this temperature, the stress increases from its compressive plateau to a tensile stress of ~30 MPa. This feature in the BSTM curve is related to stress relaxation due to defect annihilation as could be observed for pure TiN films[25]. The BSTM heating curve of the films with 15 and 22 at.% Ag show the same behavior and almost the same stress level as the film with 7 at.% Ag. Likewise, films with 30 and 38 at.% Ag show curve shapes and stress levels comparable to the film with 45 at.% Ag. This split into two groups of films can be related to stress relaxation by plastic deformation of the Ag phase (resulting in a plateau of the stress level in the BSTM curve) for films with high Ag content, while for films with lower Ag content the release of thermally induced stresses is insufficient and thus an increase in stresses is visible in the BSTM curve.

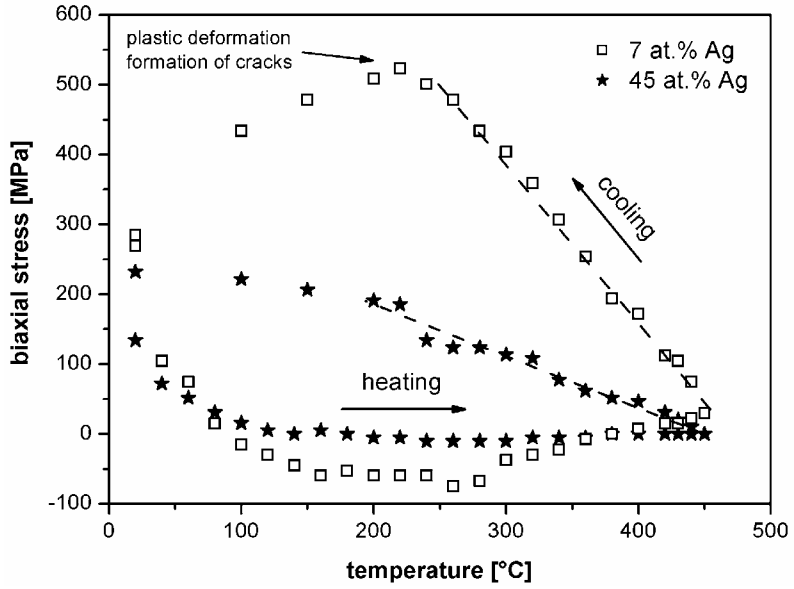

Fig. 6. BSTM cycles from room temperature up to 450°C of TiN/Ag nanocomposite films with different Ag content grown at 150°C on Si (100) substrates.

During cooling, the BSTM curves show a linear thermo-elastic behavior down to 200°C with Ag content dependent slopes, where the slopes are steeper the lower the Ag content is. The differences in the slope of the cooling segments result from thermally-induced structural changes with varying Ag content, and consequently, changes in the elastic modulus and the coefficient of thermal expansion. For temperatures below 200°C, plastic deformation for high Ag contents and the formation of micro-cracks for lower Ag contents govern the BSTM curves.

4. Conclusions

Within this work, correlations between film structure and stress development during thermal cycling were described for sputtered TiN/Ag nanocomposite films with different Ag contents. Scanning electron microscopy, atomic force microscopy and transmission electron microscopy investigations revealed a columnar structure of the film with 7 at.% Ag with Ag crystallites of 3 to 50 nm size inside. For the film with 45 at.% Ag also a columnar structure was found with slightly smaller, 3 to 30 nm, Ag particles. Additionally, a layered structure of the columns was observed which originates from the sample rotation during deposition.

During annealing, films with high Ag contents show a zero stress level from deposition temperature up to the maximum annealing temperature due to stress relieve by plastic deformation of the Ag phase. Due to their higher strength, films with lower Ag contents show a slightly compressive stress plateau above deposition temperature. However, when a critical annealing temperature is reached, the stress changes from compressive to slightly tensile. This change in slope of the stress-temperature curve is mainly related to recovery of the TiN phase. Recovery of TiN is also present in the films containing more Ag but is overruled by plastic deformation of the soft Ag phase.

Acknowledgement

This work was financially supported by the Austrian NANO Initiative via a grant from the Austrian Science Fund FWF (project N401-NAN). The authors would like to thank D. Kiener for the SEM investigations, as well as T. Klünsner for his support with AFM measurements.

References

1. F. Spaepen, Acta Mater. 48, 31 (2000)

2. G.S. Kim, S.Y. Lee, J.H. Hahn, B.Y. Lee, J.G. Han, J.H. Lee and S.Y. Lee, Surf. Coat. Technol. 171, 83 (2003)

3. M.J. Cordill, N.R. Moody and D.F. Bahr, Acta Mater. 53, 2555 (2005)

4. J. Musil, Surf. Coat. Technol. 125, 322 (2000)

5. J. Musil, P. Zeman, H. Hruby and P.H. Mayrhofer, Surf. Coat. Technol. 120-121, 179 (1999)

6. P. Zeman, R. Cerstvy, P.H. Mayrhofer, C. Mitterer and J. Musil, Mater. Sci. Eng. A289, 189 (2000)

7. K.P. Andreasen, T. Jensen, J.H. Petersen, J. Chevallier, J. Bottiger and N. Schell, Surf. Coat. Technol. 182, 268 (2004)

8. H.S. Myung, H.M. Lee, L.R. Shaginyan and J.G. Han, Surf. Coat. Technol. 163-164, 591 (2003)

9. Z.G. Lee, S. Miyake, M. Kumagai, H. Saito and Y. Muramatsu, Surf. Coat. Technol. 183, 62 (2004)

10. A.A. Voevodin, J.J. Hu, T.A. Fitz and J.S. Zabinski, Surf. Coat. Technol. 146-147, 351 (2001)

11. C. Muratore, J.J. Hu and A.A. Voevodin, Thin Solid Films 515, 3638 (2007)

12. J.J. Hu, C. Muratore and A.A. Voevodin, Compos. Sci. Technol. 67, 336 (2007)

13. C.P. Mulligan and D. Gall, Surf. Coat. Technol. 200, 1495 (2005)

14. K.J. Ma, C.L. Chao, D.S. Liu, Y.T. Chen and M.B. Shieh, J. Mater. Process. Technol. 127, 182 (2002)

15. K. Abourayak, S. Fayeulle, L. Vincent, C. Ribeiro, A. Cavaleiro and M.T. Vieira, Surf. Coat. Technol. 80, 171 (1996)

16. J.L. Endrino, J.J. Nainaparampil and J.E. Krzanowski, Scripta Mater. 47, 613 (2002)

17. M. Jirout and J. Musil, Surf. Coat. Technol. 200, 6792 (2006)

18. J. Musil and M. Jirout, Surf. Coat. Technol. 201, 5148 (2007)

19. S. Zhang, D. Sun, Y. Fu and H. Du, Surf. Coat. Technol. 198, 2 (2005)

20. S. Zhang, D. Sun, Y. Fu, Y.T. Pei and J.Th.M. De Hosson, Surf. Coat. Technol. 200, 1530 (2005)

21. J.D. Verhoeven, *Fundamentals of Physical Metallurgy*, Wiley, New York (1975)

22. M. Bielawski, Surf. Coat. Technol. 200, 3987 (2006)

23. C. Mitterer, P.H. Mayrhofer and J. Musil, Vacuum 71, 279 (2003)

24. P.H. Mayrhofer, F. Kunc, J. Musil and C. Mitterer, Thin Solid Films 415, 151 (2002)

25. H. Köstenbauer, G.A. Fontalvo, M. Kapp, J. Keckes and C. Mitterer, Surf. Coat. Technol 201, 4777 (2007)

26. J.D. Wilcock, D.S. Campbell, Thin Solid Films 3, 3 (1969)

27. Y. Zhao, G. Wang and T. Lu, in *Experimental Methods in the Physical Science, Characterization of amorphous and crystalline rough surface: principles and applications* edited R. Celotta and T. Lucatorto, Academic Press, San Diego (2001)

28. C. Teichert, Phys. Rep. 365, 335 (2002)

29. For completeness we also calculated the Hurst parameter which indicates how "jagged" the surface is. The obtained values of 0.95 ± 0.3 for the 7 at.% Ag film and 1.0±0.005 for the 45 at.% Ag film show no significant difference.

30. P. Klapetek, I. Ohlidal, D. Franta, A. Montaigne-Ramil, A. Bonanni, D. Stifter and H. Sitter, Acta Phys. Slov. 53, 223 (2003)

31. B.E. Warren; *X-ray diffraction*, Dover Publications, New York (1990)

32. R. Delhez, Th.H. de Keijser, E.J. Mittemeijer and Z. Fresenius, Anal. Chem. 312, 1 (1982)

Paper IV

Tribological Properties of TiN/Ag Nanocomposite Coatings

H. Köstenbauer, G.A. Fontalvo, C. Mitterer, J. Keckes

Tribology Letters 30 (2008) 53

Tribological Properties of TiN/Ag Nanocomposite Coatings

H. Köstenbauer [a,b], G. A. Fontalvo [a], C. Mitterer [a], J. Keckes [b]

[a] *Department of Physical Metallurgy and Materials Testing, University of Leoben, A-8700 Leoben, Austria*

[b] *Department of Materials Physics, University of Leoben, A-8700 Leoben, Austria*

Abstract

Morphology, structure and tribological behavior of magnetron co-sputtered TiN/Ag nanocomposite coatings deposited at 150°C with an Ag content in the range of 7 to 45 at.% were characterized. The coatings show a columnar structure with embedded Ag crystallites of 3 to 50 nm in diameter, where the columns are characterized by a layered structure with Ag-poor and Ag-rich layers. These layers originate from sample rotation during deposition, where the layer thickness increases with increasing Ag content. These Ag layers become continuous over a critical Ag content. At room temperature the friction coefficient is determined by the film structure, whereas friction and wear at high temperature depend on segregation of Ag to the surface.

Keywords: Nitrides; Silver; Self lubricating composites; Wear-resistant coatings.

1 Introduction

Transition metal nitride hard coatings are widely used due to their wear, corrosion and oxidation resistance. However, the friction coefficient of most of these coatings, e.g. TiN or CrN, is fairly high and the tribological effectiveness, especially at elevated temperatures, is insufficient [1]. In recent years, several investigations have been published which deal with new concepts for friction and/or wear reduction of hard coatings. One possibility to reduce friction is to form nanocomposite or superlattice structures which combine solid lubricants like graphite, DLC, MoS_2 or WS_2 with hard phases [2-6]. The incorporation of elements, like V, which are able to form lubricious oxides on the surface during high temperature exposure, can also lead to enhanced tribological properties [7-9]. However, these oxides are only formed under certain environmental conditions, i.e. oxygen containing atmosphere and elevated temperature. In addition to these lubricious oxides,

combining a soft metal phase with a hard compound has been reported as a promising approach to improve coating performance. These soft metal phases give rise to improved tribological properties over a wide temperature range due to their low shear strength. For this purpose, preferably Au and Ag, due to their chemical inertness, are used in combination with oxides [10-13], nitrides [6,14-16] and carbides [17], where reduction of friction and/or wear have been reported. The addition of a soft metal phase into a hard coating offers also the possibility to improve coating toughness by influencing e.g. intrinsic stresses and structure [18-22]. In previous investigations, it was found that the addition of Ag to transition metal nitride coatings only reduces the friction coefficient at room temperature (RT) when a relatively high Ag content is used [14-16]. For high Ag contents, Endrino et al. reported about a considerably reduced friction coefficient in vacuum also for the systems WC/Ag and TiC/Ag [17]. Also by adding Au to yttria-stabilized zirconia, a strong decrease of the friction coefficient with increasing Au content was obtained at RT [10]. However, only very limited information is available about the tribological behavior of such composites consisting of a soft metal phase embedded in a hard coating at elevated temperatures. The aim of the present work is thus to investigate the influence of the Ag content on the tribological response of a TiN/Ag composite film at RT and elevated temperatures.

2 Experimental details

TiN/Ag nanocomposite films were deposited onto Si (100) sheets ($7 \times 20 \times 0.3$ mm^3) and high-speed steel discs (DIN 1.3343, AISI M2) with 30 mm diameter and 10 mm height, which were previously quenched and tempered to a hardness of 65 HRC. The substrates were ultrasonically pre-cleaned in acetone and ethanol and plasma etched before deposition. The total thickness of the coatings was kept constant at about 3 µm. The layers were deposited by unbalanced DC reactive magnetron co-sputtering in an Ar+N_2 atmosphere from one Ag and two Ti targets (∅ 50.8 × 6.35 mm), all three focused to the substrate holder. The Ag content in the film was varied by changing the sputtering power at the Ag target. Six different Ag target power settings were chosen to deposit films with about 7, 15, 22, 30, 38 and 45 at.% Ag. The substrates were positioned at a distance of 7 cm from the center of the target cluster and rotated with a speed of approximately 10 rpm during deposition to obtain uniform chemical composition of the films. The substrate temperature and the total pressure were 150°C and 0.25 Pa, respectively. All films were

deposited at floating potential. To improve adhesion, a 50 nm thick TiN interlayer was deposited at a temperature of 450°C directly after substrate etching. Then, the substrates were cooled down to 150°C to deposit the nanocomposite without excessive Ag diffusion [23].

The films were characterized using atomic force microscopy (AFM) (Digital Instruments Nanoscope IIIa) with conventional Si-tips in tapping mode according to the procedure described in [24], scanning electron microscopy (SEM) (Zeiss EVO 50, acceleration voltage, 20 kV), energy-dispersive X-ray (EDX) analysis, X-ray diffraction (XRD) (Siemens D500) in Bragg-Brentano geometry using Cu Kα radiation, transmission electron microscopy (TEM) and scanning transmission electron microscopy (STEM) of cross-sections. The atomic percentages presented here are calculated by [Ag]/([Ag]+2[Ti]) without considering impurities which corresponds to [Ag]/([Ag]+[Ti]+[N]) assuming that the TiN is nearly stoichiometric. The samples for TEM investigations were prepared using standard preparation method with final Ar ion milling at 4kV (angle 4°/6°) and were conducted with a FEI TECNAI TF20, field emission gun, 200kV microscope. The coating hardness was determined by nanoindentation (UMIS II) using a Berkovich indenter before and after high-temperature tribometer tests. After calibrating the device, hardness measurements were conducted at maximum loads between 2 and 50 mN with 2 mN steps. The values of film hardness H were then plotted against the penetration depth h_t, and only those values which belong to a plateau in the values of H, where no influence of the substrate can be guaranteed, were taken for calculating the average hardness of the film.

Dry sliding experiments were performed at RT, 200, 300, and 500 °C in ambient air using a high-temperature ball-on-disc tribometer (CSM THT) with alumina balls of 6 mm diameter as counterpart. The relative humidity was between 30 and 40 % for all tests. Sliding speed and normal load were kept constant at 0.1 m/s and 1 N. The radius of the wear track was 7 mm and the sliding distance 100 m. The wear tracks were investigated using a white-light profilometer (Veeco NT1000) and SEM. Additionally, the white-light profilometer was used to measure the sample roughness.

3 Results

3.1 Coating microstructure and surface topography

Fig. 1 shows XRD patterns of the nanocomposite coatings with 7, 15, 22, 30, 38 and 45 at.% Ag deposited on Si (100) substrates. The Ag contents given in this work correspond to the averaged Ag concentration in the films as described above. The TiN and Ag peaks of the different orientations are overlapping, and they gradually shift from the TiN towards the Ag standard position with increasing Ag content in the coating. Co-deposition of Ti and Ag results in the formation of a dual-phase structure containing the face-centered cubic (fcc) TiN and fcc Ag phase. XRD line broadening analysis was used to calculate the coherently diffracting domain size [25,26]. For this purpose, two Pseudo-Voigt functions, one for TiN (111) and one for Ag (111), were fitted to the overlapping (111) peaks (cf. insert in Fig. 1). The results indicate a size of coherently diffracting domains in the as-deposited state of 15-30 nm of the TiN phase in all coatings. The domain size of the Ag phase is 20 nm for the coating with 7 at.% Ag and 6 nm for all coatings with higher Ag content. During annealing at 300°C, the domain size of all samples does not change significantly.

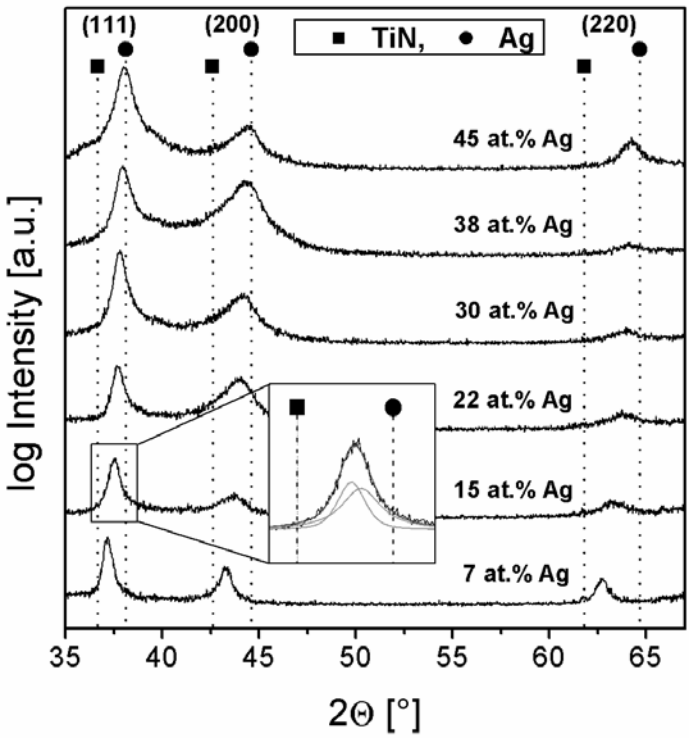

Fig. 1 XRD patterns of TiN/Ag nanocomposite films with increasing Ag content on silicon substrates.

To shed more light onto the film structure, TEM investigations were conducted on cross-sections of the films with 7 and 45 at.% Ag. Fig. 2a and 2b show the HAADF (high-angle annular dark field) STEM micrographs (Z-contrast) of the coating with 7 at.% Ag. The coating exhibits a columnar structure with a column width of ~80 nm (Fig. 2a). Inside the columns bright spots can be seen which represent embedded Ag domains as confirmed by EDX. At higher magnification (Fig. 2b), a range of particle sizes with diameters of 50 nm down to ~3 nm exist [23].

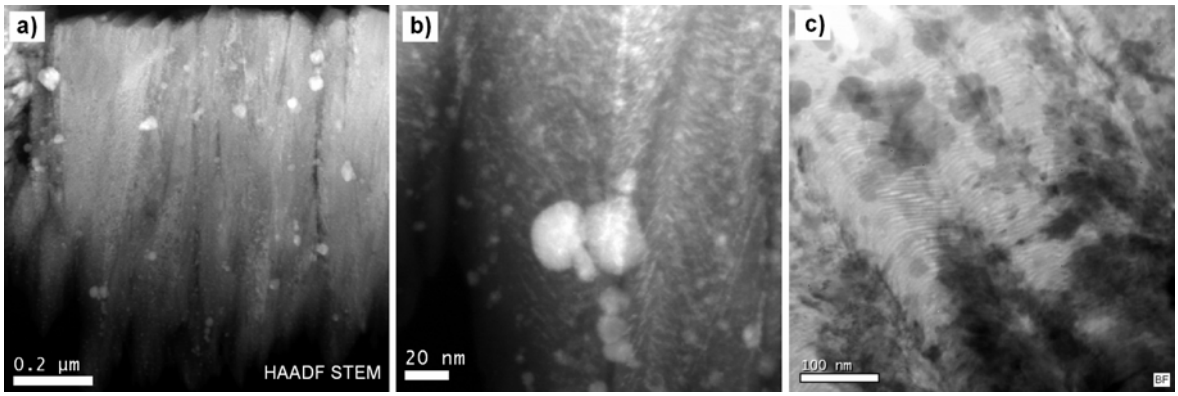

Fig. 2 (a) HAADF STEM micrograph of the coating with 7 at.% Ag; (b) HAADF STEM micrograph of the coating with 7 at.% Ag with higher magnification; (c) BF TEM micrograph of the coating with 45 at.% Ag.

Fig. 2c shows the BF (bright field) TEM micrograph of the film with 45 at.% Ag which exhibits also a columnar structure with a column width of ~100 nm. Dark spots can be seen inside the columns with diameters of ~30 nm down to ~3 nm [23] representing Ag domains, and a layered structure with a layer distance of ~4 nm can be observed inside the columns. This structure consists of Ag-poor and Ag-rich layers as confirmed by EDX; their formation is the result of sample rotation during deposition since the samples undergo during rotation plasma regions with higher (near the Ag target) and lower Ag contents. It should be noted that the Ag-rich layers seem to get thicker the higher the Ag content in the coating is. The layer distance and thickness corresponds well to the Ag domain size calculated for all films with higher Ag contents than 7 at.%. It can be assumed that continuous Ag-rich layers are formed for Ag contents higher than 7 at.%, and are the reason for the small domain size calculated for higher Ag contents. It should be noted that no clear correlation between size of the Ag particles and the Ag content of the coating could be found.

Measurements conducted with the white light profilometer indicated an increase in roughness with increasing Ag content. For a more accurate result, AFM measurements were conducted on the samples with the lowest and the highest Ag content. The root mean square (rms) roughness of the film containing 7 at.% Ag is 4.7 ± 0.2 nm, as obtained by AFM. This is lower than for the film containing 45 at.% Ag with an rms-roughness of 7.6 ± 0.6 nm. This roughness variation is not expected to play a significant role in the tribological behavior of the coatings.

3.2 Mechanical and tribological properties

As-deposited coatings with 0, 7 and 15 at.% Ag show the same hardness of 15 GPa and a slightly decreasing Young's Modulus from 330±20 over 300±15 to 280±10 GPa, respectively. The coatings with 22, 30, 38 and 45 at.% Ag show decreasing hardness values of 12, 10, 9 and 8 GPa and a Young's Modulus of 220±10, 200±15, 190±20 and 170±15 GPa, respectively. The low hardness of the unalloyed TiN coating is related to the low deposition temperature of 150°C which prevents the formation of a dense structure [27]. After tribological testing at 300°C, the hardness of the coatings does not change significantly. Hardness measurements on the coatings tested at 500°C were not possible due to the Ag segregation on the surface during the test [13,14].

Figure 3 shows the mean friction coefficient of TiN coatings with 0, 7, 22, and 45 at.% Ag sliding against alumina balls in ambient air at different temperatures.

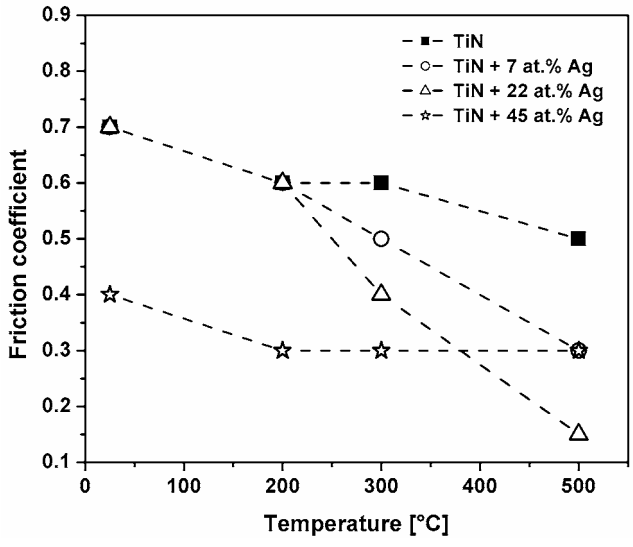

Fig. 3 Temperature dependence of the friction coefficient for TiN and TiN + Ag coatings measured against alumina balls.

After a short running-in period, the coatings with 0, 7, and 22 at.% Ag show the same steady-state friction coefficient of 0.7 at RT and 0.6 at 200°C. Above this temperature, a strong temperature and Ag content dependent variation of the friction coefficient can be observed. The friction coefficient for TiN decreases slightly from 0.6 at 200°C and 300°C to 0.5 at 500°C which might be related to the onset of surface oxidation and ongoing softening of the coating [7,28]. The incorporation of 7 at.% Ag results in a stronger decrease of the friction coefficient with increasing temperature to about 0.3 at the maximum temperature of 500°C. The coating containing 22 at.% Ag shows the strongest decrease from 0.6 at 200°C to 0.4 at 300°C and 0.15 at 500°C. For the coating with the highest Ag content (45 at.%), the slope of friction vs. temperature behavior is significantly different. This coating exhibits a lower friction coefficient of 0.4 at RT and a constant value of 0.3 in the temperature range between 200°C and 500°C. The coatings with 30 and 38 at.% Ag, not shown in Fig. 3, exhibit the same values of friction coefficients as the coating with 45 at.% Ag at RT, 200 and 300°C. At 500°C, the friction coefficient of the coating with 38 at.% Ag differ from those of the coatings with 30 and 45 at.% Ag. This might be connected to an early failure of the coating which yields a higher friction coefficient and considerable scattering due to the interaction of wear debris with both surfaces in contact.

Figure 4 shows the 2D profiles of the wear tracks after ball-on-disc tests at RT, 300°C, and 500°C for the coatings with 7, 22, 30 and 45 at.% Ag, respectively. The coating with 7 at.% Ag (Fig. 4a) shows abrasive wear at RT which is evidenced by plows in the wear track. This wear track is comparable to the wear track of unalloyed TiN tested under the same conditions [7]. Increasing the testing temperature to 300°C results in a decreasing depth of the wear track (see Fig. 4a), where a further increase of the testing temperature to 500°C leads to a further decrease in the depth of the wear track and an increase in the amount of transfer material.

The coating with 22 at.% Ag (Fig. 4b) shows also abrasive wear at RT but the wear track is about two times broader than the wear track of the coating with 7 at.% Ag. This may be related to the deteriorating mechanical properties, in particular the coating hardness, due to the higher Ag content. For a testing temperature of 300°C, there is less wear visible for the coating with 22 at.% Ag compared to the coating with 7 at.% Ag. At the highest testing temperature of 500°C, no wear is visible.

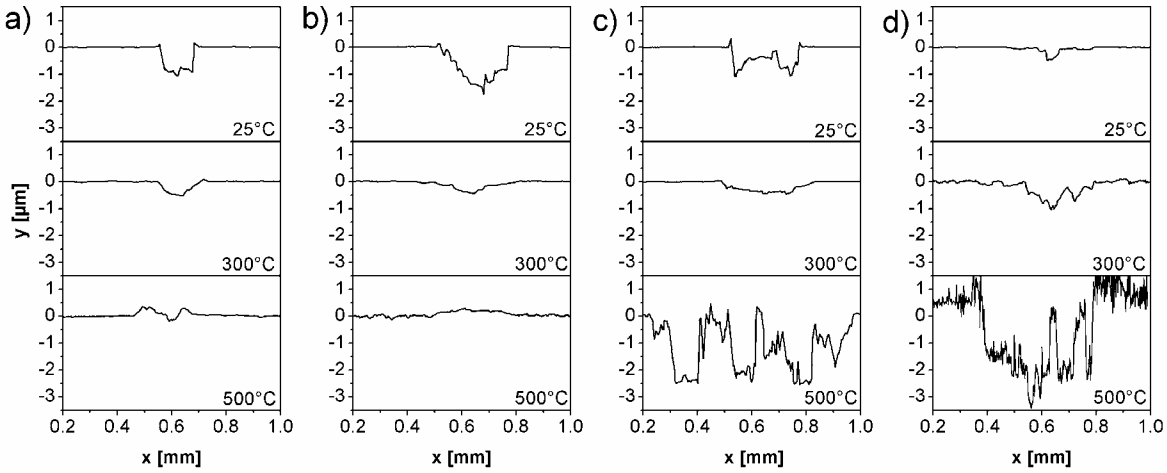

Fig. 4 The 2D cross-sections of the wear tracks of the coatings with (a) 7 at.% Ag, (b) 22 at.% Ag, (c) 30 at.% Ag and (d) 45 at.% Ag.

For the coating with 30 at.% Ag, wear decreases compared to the coating with 22 at.% Ag and small amounts of transfer material are visible at RT (see Fig. 4c). In contrast, the wear track after the test at 300°C is broader and slightly deeper than those of the 22 at.% Ag coating. This deteriorated wear behavior originates from the worsened mechanical properties due to the high amount of Ag and the concomitant softening of the coating at higher temperatures. Consequently, increasing the testing temperature to 500°C results in failure of the coating with a lot of transfer material in the wear track as visible in Fig. 4c.

For the highest Ag content (45 at.%), only a small amount of abrasive wear and transfer material are visible at RT (see Fig. 4d). The wear track after the test at 300°C is very broad and the coating is partly worn through (as confirmed by SEM and EDX). The increase of the testing temperature to 500°C results in a total failure of the coating. The coating with 38 at.% Ag shows a very similar wear to the coating with 45 at.% Ag for all testing temperatures, and is thus not shown in Fig. 4.

Fig. 5 shows representative backscattered electron SEM micrographs of the coatings after RT tests. For the coating with 7 at.% Ag (Fig. 5a), no differences between unaffected coating surface and wear track are visible. A small amount of transferred material can be seen on both sides of the wear track (see dark spots in Fig. 5a). The TiN + 22 at.% Ag coating looks similar to the sample with 7 at.% Ag. For the higher Ag containing coatings with 30, 38 and 45 at.%, higher amounts of transfer material are visible. A representative micrograph of the coating with 45 at.% Ag is shown in Fig. 5b where the dark grey areas

represent the transfer material, but also smaller particles can be seen in the middle of the wear track. The wear track is wider than those of the other coatings.

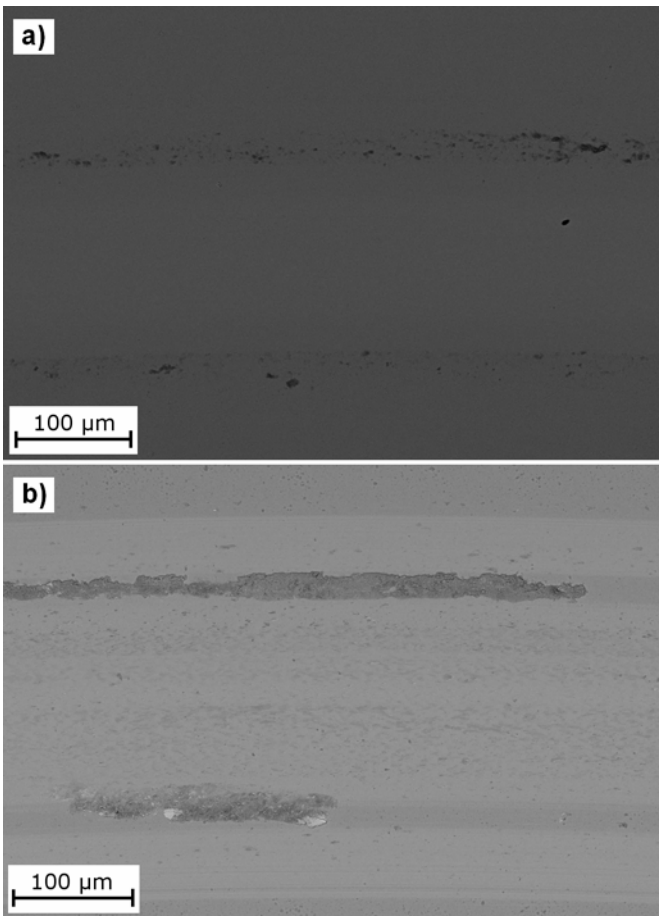

Fig. 5 SEM micrographs of the wear tracks after RT tests of the coatings with a) 7 at.% Ag and b) 45 at.% Ag.

The results of the SEM investigations of the wear tracks after the tribological tests at 500°C are summarized in Fig. 6. A slightly higher amount of transfer material is visible for the coating with 7 at.% Ag (Fig. 6a) compared to the RT sample. Additionally, bright spots can be seen at the coating surface representing Ag particles formed by out-diffusion [13]. In case of the coating with 22 at.% Ag (Fig. 6b), there are much more Ag particles visible at the surface outside the wear track. In the center of the wear track, white areas can be observed which correspond to the tribologically induced formation of a continuous Ag layer. The discontinuous dark area in the middle of the white Ag tribolayer results from partial removal of the Ag layer by the alumina ball.

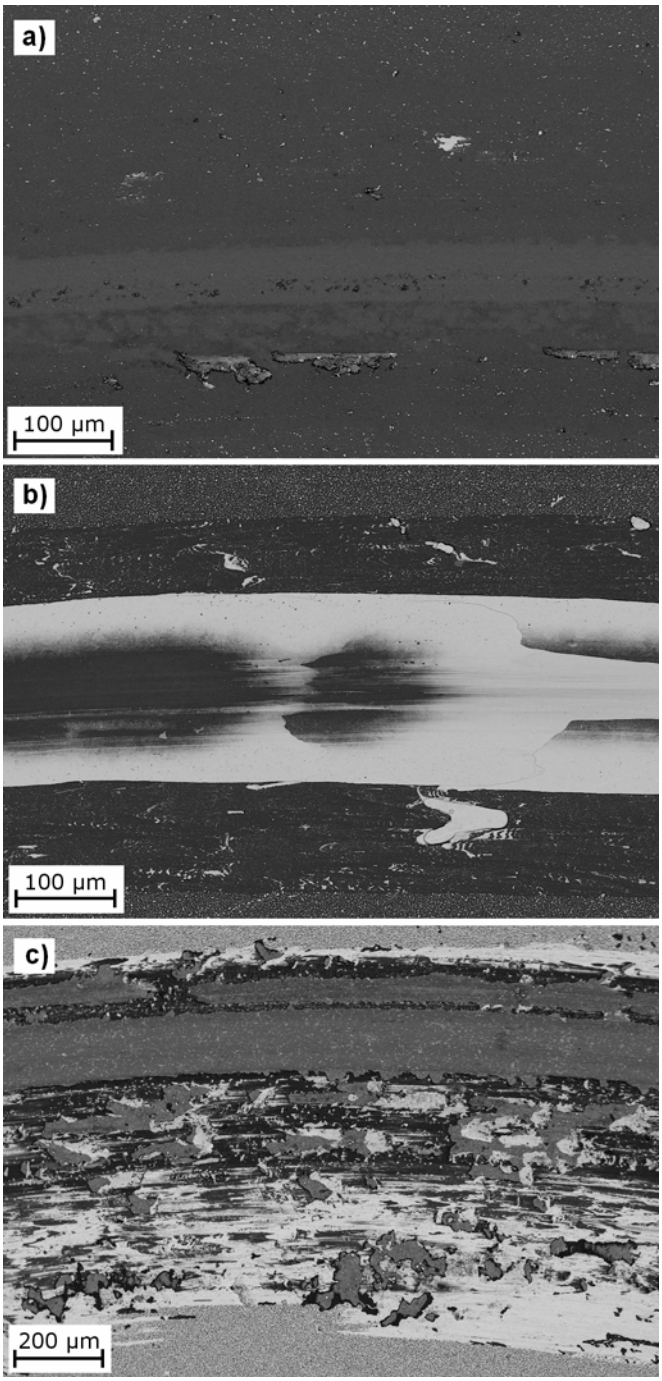

Fig. 6 SEM micrographs of the wear tracks of the coatings with a) 7 at.% Ag, b) 22 at.% Ag, and c) 45 at.% Ag after ball-on-disc testing at 500°C.

As indicated above, coating failure occurs for the coating with 45 at.% Ag during high-temperature testing. There, white, grey and black areas can be observed in the wear track (see Fig. 6c). The white areas correspond again to the Ag tribo-layer. In contrast to the wear track of the coating with 22 at.% Ag, there is no evidence of a continuous coverage of the wear track by Ag. Oxidized particles have been back transferred to the wear track,

which can bee seen in the form of black areas. Furthermore, complete failure of the coating is evidenced by the dark grey areas indicating the carbides of the high-speed steel substrate [29]. The wear tracks of the samples with 30 and 38 at.% Ag do not evidence any continuous Ag tribolayer, and that of the sample with 38 at.% Ag is very similar to the coating with 45 at.% Ag. In the case of the coating with 30 at.% Ag it looks like wear debris, consisting of oxidized TiN and Ag, have been mixed and back-transferred to the coating.

4 Discussion

All TiN-Ag coatings synthesized by co-sputtering from Ti and Ag targets exhibit a columnar structure with slightly different column widths. Ag is mainly concentrated in small domains within the columns as well as in Ag-rich layers which originate from sample rotation during film growth. These layers are not continuous for the 7 at.% Ag coating. In our previous work [23] it has been concluded that at least an average Ag concentration of 15 at.% is needed to form a continuous Ag-rich layer. There, the thickness of the Ag-rich layers increases with increasing Ag content while the thickness of the Ag-poor layers remains nearly constant. At RT, the tribological behavior of the coatings is mainly determined by their mechanical properties. Both wear and friction can be seen as energy dissipating processes. In the case of a harder material sliding against a softer ductile material (like in the present case), energy is dissipated when it comes to wear by elastic and plastic deformation of the soft material, the latter been evidenced by plows and wear debris formed due to microcutting. The elastic part is determined by the Young's modulus of the softer material, the plastic part by its hardness (or better, its yield strength). In case of our coatings, both Young's modulus and hardness decrease with increasing Ag content. A lower Young's modulus yields a higher energy dissipation by elastic deformation, and consequently, less energy has to be dissipated by plastic deformation. The energy dissipated by elastic deformation should increase with increasing Ag content. However, for the coatings with 7 at.% and 22 at.% Ag energy dissipation by plastic deformation seems to be still determinant for both coatings, and thus, the softer coating shows higher wear. In case of higher Ag content in the coatings, a significant amount of energy might be dissipated by elastic deformation, such that plastic deformation do not play a significant role, and thus, wear constantly decreases despite the decreasing hardness with increasing Ag content. Therefore the coating with 45 at.% Ag exhibits the lowest value for both,

hardness and wear. Considering the model of velocity accommodation in friction according to Berthier et al. [30], velocity should be accommodated by, among other mechanisms, shearing of the bodies in contact. Now considering the layered structure of the coatings, it can be presumed that shearing of the Ag-rich layers is easier. This mechanism should be more efficient for the coating with 45 at.% Ag, and consequently it shows the lowest friction coefficient at RT. Even after a third body (i.e., back-transferred material at RT) is formed, shearing of the coating seems still to be relevant. Following these considerations, the lower hardness and layered structure of the sample with 22 at.% Ag should also result in a lower friction coefficient than that of TiN and TiN with 7 at.% Ag. However, the higher wear of this coating is accompanied by a higher amount of wear debris, and the friction coefficient increases due to the interaction of wear debris with both surfaces in contact. In case of the coating with 7 at.% Ag, shearing is more difficult due to the discontinuous and thinner Ag-rich layers, which leads to a friction coefficient similiar to TiN. The coatings with 30 and 38 at.% Ag show a similar behaviour to the coating with 45 at.% Ag. The mechanical softening of the coating with increasing Ag content promotes the reduction of friction by shearing. It might be presumed that a critical point has been reached at 30% Ag where friction is mainly determined by the elastic behavior of the coatings, while for coatings with a lower content, friction is determined mainly by the interaction of wear debris with both surfaces in contact.

TiN shows usually a lower friction coefficient and higher wear as temperature increases due to softening of the coating and the onset of surface oxidation [7,28]. In the case of Ag-alloyed TiN coatings, Ag atoms start to segregate to the surface of the coating once a critical temperature is reached, which seems to be between 200 and 300°C, forming bigger particles. These particles act as a third body which can be sheared easily, and thus, friction decreases with increasing Ag content. Moreover, also wear decreases, as more particles are formed which prevent contact between the ball and the coating surface. Ag segregation is promoted by higher temperatures, and thus, both friction and wear decrease with increasing temperature. Here again, the samples with 30, 38 and 45 at.% Ag show a different behavior because of their low hardness. Thus, severe wear and ultimately coating failure occurs. Additionally, friction is not reduced with increasing temperature as the formed Ag particles do not provide a sustainable and efficient tribolayer for preventing contact between ball and coating surface.

5 Conclusions

Within this work, correlations between film structure, Ag content and tribological properties were described for sputtered TiN/Ag nanocomposite films. Transmission electron microscopy investigations revealed a columnar structure of all films with embedded Ag crystallites of 3 to 50 nm in diameter, and a layered structure of the columns with Ag-poor and Ag-rich layers, originating from sample rotation during deposition. With increasing Ag content, the thickness of the Ag-rich layers increases while that of the Ag-poor layers remains constant. Likewise, hardness decreases from 15 GPa for the TiN coating to 8 GPa at 45 at.% Ag. At room temperature, wear increases with increasing Ag content due to the concomitant softening of the coatings. However, coatings with very high Ag content show low wear presumably due to increased elasticity of the coating and energy dissipation by elasto-plastic deformation during the tribological test. Friction seems to be determined by shearing of the coatings for Ag contents higher than 30 at% and by the interaction of wear debris with the surface in contact for lower Ag contents. At elevated temperatures, Ag segregates to the surface acting as a solid lubricant which reduces friction and wear, particularly when a continuous Ag tribolayer is formed.

Finally, it can be concluded that the Ag content in TiN/Ag nanocomposites has to be adjusted properly according to the application temperature, since higher Ag contents give better performance at low temperatures, but the loss in mechanical stability of the coatings with higher Ag contents is disadvantageous at higher temperatures.

Acknowledgement

This work was financially supported by the Austrian NANO Initiative via a grant from the Austrian Science Fund FWF (project N401-NAN). The authors would like to thank Prof. C. Teichert, Dr. G. Hlawacek and T. Klünsner for their support with AFM measurements.

References

1. Polcar, T., Kubart, T., Novak, R., Kopecky, L., Siroky, P.: Comparison of tribological behavior of TiN, TiCN and CrN at elevated temperatures. Surf Coat Technol 193, 192-199 (2005)

2. Derflinger, V., Brändle, H., Zimmermann, H.: New hard/lubricant coating for dry machining. Surf Coat Technol 113, 286-292 (1999)

3. Voevodin, A.A., O`Neill, J.P., Zabinski, J.S.: Nanocomposite tribological coatings for aerospace applications. Surf Coat Technol 116-119, 36-45 (1999)

4. Carrera, S., Salas, O., Moore, J.J., Woolverton, A., Sutter, E.: Performance of CrN/MoS_2 (Ti) coatings for high wear low friction applications. Surf Coat Technol 167, 25-32 (2003)

5. Hirvonen, J.-P., Koskinen, J., Jervis, J.R., Nastasi, M.: Present progress in the development of low friction coatings. Surf Coat Technol 80, 139-150 (1996)

6. Ma, K.J., Chao, C.L., Liu, D.S., Chen, Y.T., Shieh, M.B.: Friction and wear behaviour of TiN/Au, TiN/MoS_2 and TiN/TiCN/a-C:H coatings. J Mater Proc Technol 127, 182-186 (2002)

7. Fateh, N., Fontalvo, G.A., Gassner, G., Mitterer, C.: Influence of high-temperature oxide formation on the tribological behaviour of TiN and VN coatings. Wear 262, 1152-1158 (2007)

8. Gassner, G., Mayrhofer, P.H., Kutschej, K., Mitterer, C., Kathrein, M.: A new low friction concept for high temperatures: lubricious oxide formation on sputtered VN coatings. Tribol Lett 17, 751-756 (2004)

9. Kutschej, K., Mayrhofer, P.H., Kathrein, M., Polcik, P., Mitterer, C.: A new low-friction concept for $Ti_{1-x}Al_xN$ base coatings in high-temperature applications. Surf Coat Technol 188-189, 358-363 (2004)

10. Voevodin, A.A., Hu, J.J., Fitz, T.A., Zabinski, J.S.: Tribological properties of adaptive nanocomposite coatings made of yttria stabilized zirconia and gold. Surf Coat Technol 146-147, 351-356 (2001)

11. Muratore, C., Voevodin, A.A., Hu, J.J., Zabinski, J.S.: Tribology of adaptive nanocomposite yttria-stabilized zirconia coatings containing silver and molybdenum from 25 to 700°C. Wear 261, 797-805 (2006)

12. Muratore, C., Hu, J.J., Voevodin, A.A.: Adaptive nanocomposite coatings with a titanium nitride diffusion barrier mask for high-temperature tribological applications. Thin Solid Films 515, 3638-3643 (2007)

13. Hu, J.J., Muratore, C., Voevodin, A.A.: Silver diffusion and high-temperature lubrication mechanisms of YSZ-Ag-Mo based nanocomposite coatings. Compos Sci Technol 67, 336-347 (2007)

14. Mulligan, C.P., Gall, D.: CrN-Ag self-lubricating hard coatings. Surf Coat Technol 200, 1495-1500 (2005)

15. Kutschej, K., Mitterer, C., Mulligan, C.P., Gall, D.: High-temperature tribological behavior of CrN-Ag self-lubricating coatings. Adv Eng Mater 11, 1125-1129 (2006)

16. Abourayak, K., Fayeulle, S., Vincent, L., Ribeiro, C., Cavaleiro, A., Vieira, M.T.: Tribological behaviour at elevated temperatures of thin physical vapour deposited coatings. Surf Coat Technol 80, 171-175 (1996)

17. Endrino, J.L., Nainaparampil, J.J., Krzanowski, J.E.: Magnetron sputter deposition of WC-Ag and TiC-Ag coatings and their frictional properties in vacuum environments. Scripta Mater 47, 613-618 (2002)

18. Jirout, M., Musil, J.: Effect of addition of Cu into ZrO_x film on its properties. Surf Coat Technol 200, 6792-6800 (2006)

19. Musil, J., Jirout, M.: Toughness of hard nanostructured ceramic thin films. Surf Coat Technol 201, 5148-5152 (2007)

20. Zhang, S., Sun, D., Fu, Y., Du, H.: Toughening of hard nanostructural thin films: a critical review. Surf Coat Technol 198, 2-8 (2005)

21. Zhang, S., Sun, D., Fu, Y., Pei, Y.T., De Hosson, J.Th.M.: Ni-toughened nc-TiN/a-SiN_x nanocomposite thin films. Surf Coat Technol 200, 1530-1534 (2005)

22. Voevodin, A.A., Zabinski, J.S.: Supertough wear-resistant coatings with “chameleon” surface adaptation. Thin Solid Films 370, 223-231 (2000)

23. Köstenbauer, H., Fontalvo, G.A., Mitterer, C., Hlawacek, G., Teichert, C., Keckes, J.: Structure, stresses and stress relaxation of TiN/Ag nanocomposite films. J Nanosci Nanotechnol, accepted

24. Teichert, C.: Self-organization of nanostructures in semiconductor heteroepitaxy. Phys Rep 365, 335-432 (2002)

25. Warren, B.E.: X-ray diffraction, Dover Publications, New York (1990)

26. Delhez R., de Keijser Th.H., Mittemeijer E.J.: Determination of crystallite size and lattice distortions through X-ray diffraction line profile analysis - Recipes, methods and comments. Fresenius Z Anal Chem 312, 1 (1982)

27. Petrov, I., Barna, P.B., Hultman, L., Greene, J.E.: Microstructural evolution during film growth. J. Vac. Sci. Technol. A 21, 117-128 (2003)

28. Mayrhofer, P.H., Hörling, A., Karlsson, L., Sjölen, J., Larsson, T., Mitterer, C., Hultman, L.: Self-organized nanostructures in the Ti-Al-N system. Appl Phys Lett 83, 2051-2094 (2003)

29. Fontalvo, G.A., Humer, R., Mitterer, C., Sammt, K., Schemmel, I.: Microstructural aspects determining the adhesive wear of tool steels. Wear 260, 1028-1034 (2006).

30. Berthier, Y., Godet, M., Brendle, M.: Velocity accommodation in friction. Tribol Trans 32, 490-496 (1989)

Paper V

Structure, stresses and stress relaxation of TiN/Cu multilayer and nanocomposite coatings

H. Köstenbauer, A. M. Hofer, G. A. Fontalvo, J. Keckes, C. Mitterer

Submitted for publication

Structure, stresses and stress relaxation of TiN/Cu multilayer and nanocomposite coatings

H. Köstenbauer [a,b], A. M. Hofer [a,b], G. A. Fontalvo [a], J. Keckes [b,c], C. Mitterer [a]

[a] *Department of Physical Metallurgy and Materials Testing, University of Leoben, A-8700 Leoben, Austria*

[b] *Department of Materials Physics, University of Leoben, A-8700 Leoben, Austria*

[c] *Erich Schmid Institute of Materials Science, Austrian Academy of Sciences, A-8700 Leoben, Austria*

Abstract

Magnetron sputtered TiN/Cu multilayer thin films with a bilayer thickness Λ in the range of 100-800 nm as well as nanocomposite films with a Cu content up to 30 at.% were characterized to investigate the effect of adding a soft metal to a hard nitride phase on residual stresses, structure and thermal behavior. All nanocomposite films exhibit small domain sizes for Cu between 5 and 20 nm dependent on the Cu content. In contrast, the multilayer coatings show a strong correlation between domain size of Cu and bilayer thickness. To investigate the relationship between film structure and stress development, the films were thermally cycled in vacuum from room temperature up to a maximum temperature of 650°C. All stress-temperature curves show significant changes during heating and linear thermo-elastic behavior during cooling. Plastic deformation of the metal phase and stress relaxation of both components are the reason for the changes during heating and the determining factors for the stress temperature behavior in multilayer as well as nanocomposite arrangements.

Keywords: Copper; Titanium nitride; Multilayer; Nanocomposite; Stress

1. Introduction

The understanding of residual stresses is of major importance to increase the lifetime of wear-protecting coatings on e.g. tools or engineering components. These could enable to engineer coating stresses and consequently to optimize coating behaviour in application. Residual stresses are composed of an intrinsic part resulting from growth defects and a

thermal part caused by the mismatch of thermal expansion coefficients of coating and substrate [1]. Due to the fact that most of these coatings are exposed to higher temperatures during operation, not only the stresses but also the stress relaxation due to defect annihilation plays an important role [2,3]. In a previous work we investigated thickness-dependent stresses in TiN, and correlated them with stress relaxation and a thickness-dependent gradient in point defect density [3]. Literature reports that the addition of a soft metal phase to a hard coating in multilayer or nanocomposite arrangements can improve coating properties, e.g. hardness [4-6], toughness [7,8] or friction and wear [9-11]. Recently, we used TiN/Ag as a model system to investigate stresses and stress relaxation in multilayer [12] as well as nanocomposite coatings [13]. Ag offers beneficial properties like its chemical inertness which is necessary when using a reactive atmosphere during deposition to ensure that Ag is present as pure metal in the coating, e.g. to act as solid lubricant [14]. However, the high surface mobility of Ag atoms, which results in liquid-like coalescence [15] and clustering [12,13] , results in some difficulties. Due to this inherent property, the surface roughness of the multilayers increases with layer thickness [12,16], and the initial porosity in the multilayer as well as the nanocomposite leads to sintering effects during annealing, all of which influence the stress development significantly [12,13]. To minimize those problems and their effect on stress and stress relaxation, Cu with its lower surface mobility was chosen for this work.

2. Experimental details

TiN/Cu multilayer and nanocomposite films were deposited by unbalanced DC magnetron sputtering onto Si (100) substrates with thicknesses of 200 and 300 µm, respectively. The substrates were ultrasonically pre-cleaned in acetone and ethanol and plasma etched using an Ar plasma before deposition. The total thickness of the multilayer was kept constant at ~800 nm, while the bilayer thickness Λ varied from 100 to 800 nm, with the ratio of Cu to TiN layer thickness held constant at about 1:1. The layers were deposited by sputtering from one Cu and two Ti targets (∅ 50.8×6.35 mm^3) in Ar in case of Cu and in Ar+N_2 in case of TiN. To improve adhesion, a 20 nm thick TiN interlayer in case of the multilayers and a 50 nm thick TiN interlayer in case of the nanocomposites were deposited directly after substrate etching. For the multilayers, the layer sequence started then with a Cu layer and ended with a TiN top layer. The nanocomposite films were reactively co-sputtered from one Cu and two Ti targets in Ar+N_2 and the composition was varied by changing the

sputtering power at the Cu target. The film thickness was kept constant at ~3 µm. Six different Cu target power settings were chosen to deposit films with about 7, 14, 19, 24, 28 and 30 at.% Cu. The substrates were positioned at a distance of 7 cm from the centre of the target cluster and rotated with a speed of approximately 20 rpm during deposition to obtain uniform films. The substrate temperature T_D and the total pressure were 350°C and 0.25 Pa, respectively. All nanocomposite coatings were deposited at a bias voltage of -50 V whereas for the multilayer coatings a bias voltage of -80 V was used.

The films were characterized using scanning electron microscopy (SEM), X-ray diffraction (XRD) in Bragg-Brentano geometry using Cu Kα radiation, biaxial stress temperature measurements (BSTM) and nanoindentation. During BSTM, the films were subjected to a thermal cycle from 25 to 650°C in vacuum ($p \leq 10^{-3}$ Pa) at a heating and cooling rate of 5 K min^{-1}. Two parallel laser beams were used to measure the variation of the substrate curvature during annealing. The biaxial film stress was calculated from the substrate-curvature radius using the modified Stoney equation [17]. Nanoindentation was done for the thicker nanocomposite coatings by a UMIS II system using a Berkovich indenter. After calibrating the device, 20 indents were made at a load of 15 mN, corresponding to an indentation depth of ~10% of the coating thickness. For the multilayer films, reliable hardness measurements are prevented by the lower overall thickness of the coatings and of the single-layers.

3. Results and discussion

3.1 Film structure

Fig. 1 shows XRD patterns for (a) the multilayer and (b) the nanocomposite coatings on Si (100) substrates. In case of the multilayer coatings (Fig. 1a), the TiN (200) and Cu (111) peaks are slightly overlapping but nevertheless clearly separated. With decreasing bilayer thickness Λ, the intensity of the peaks decreases and the broadening increases indicating a refinement in structure. No significant peak shift from the standard positions is visible. For the TiN/Cu nanocomposite coatings (Fig. 1b), there is no clear separation of the TiN (200) and the Cu (111) peak visible for Cu contents below 19 at.%. Above 19 at.% Cu, the peaks start to get separated where for both the Cu and TiN reflections again no significant peak shift from the standard positions is seen. This is probably an indication of the presence of the Cu and TiN phase with no significant mutual solubility.

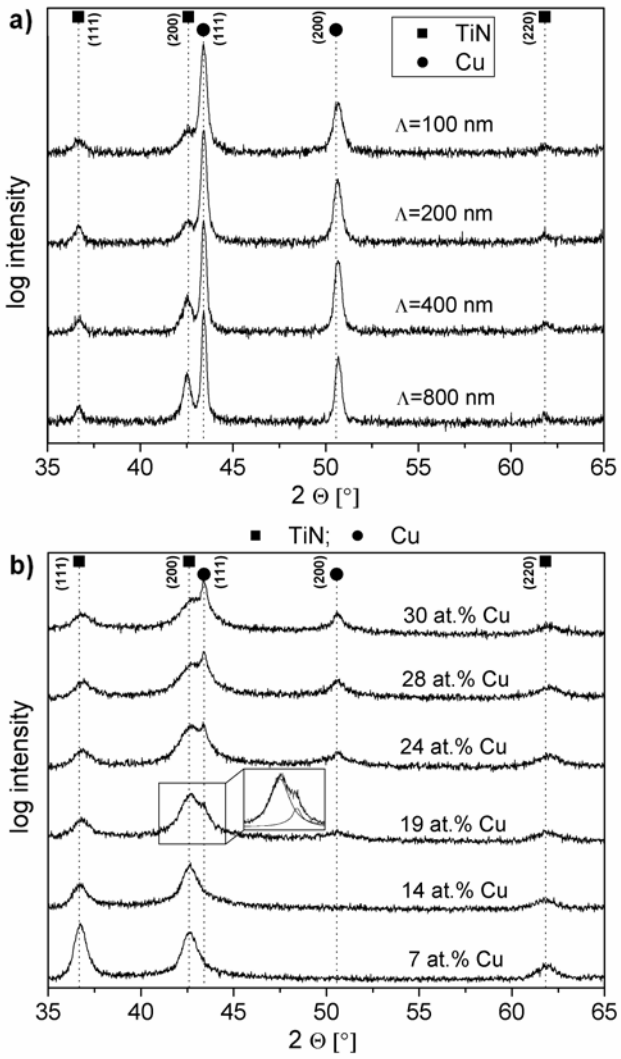

Fig. 1. XRD patterns of (a) TiN/Cu multilayer films with different bilayer thickness Λ and (b) TiN/Cu nanocomposite films with increasing Cu content on Si (100) substrates.

The evolution of peaks from lower to higher Cu contents suggests that also below 19 at.% Cu, two separate phases and no solid solution is formed. With increasing Cu content, the intensity of the Cu peaks increases. Likewise, the intensity of the TiN peaks decreases at increasing peak broadening, which suggests a structural refinement of the TiN phase. Additionally, a change in the preferred orientation of TiN from (111) to (200) with increasing Cu content can be seen. This change is most evident when increasing the Cu content from 7 at.% to 14 at.% Cu in the coating. For higher Cu contents, the (200) peak becomes the major peak for the TiN phase. It may be assumed that the change in orientation is due to a structural correlation between the TiN and Cu phases. Öztürk et al. observed a similar change in preferred orientation from TiN (220) towards TiN (200) by adding ~13 at.% Cu to TiN [18]. A structural correlation between TiN and Cu was also

reported for TiN/Cu multilayers with bilayer thicknesses of only a few nm [16]. The (200) surface of TiN shows a low lattice mismatch of less than 2 % compared to Cu (111). Thus, coherent or semi-coherent interfaces between Cu and TiN could then be formed.

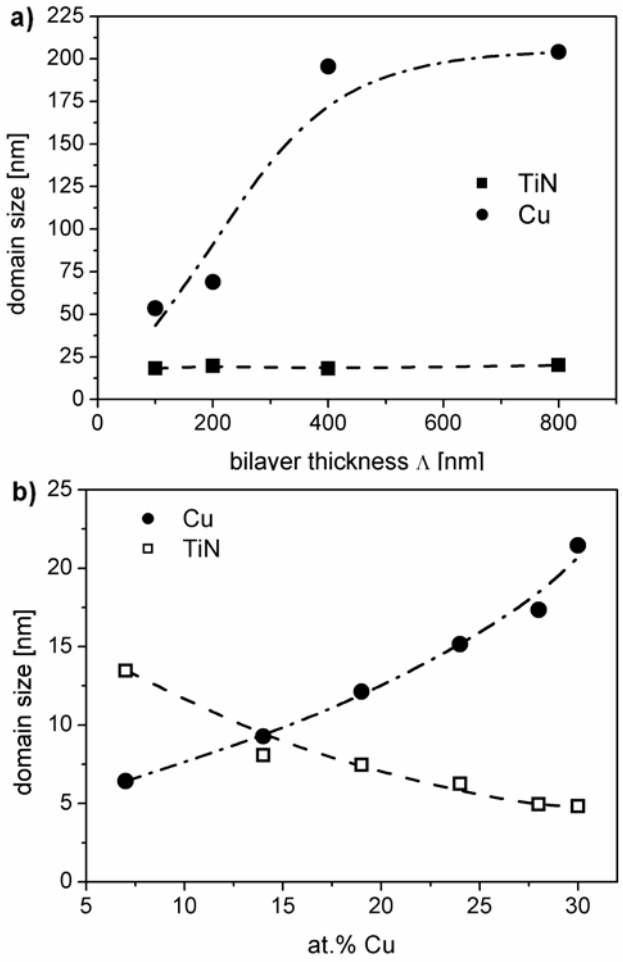

Fig. 2. Domain sizes calculated from the integral breadth of (a) the TiN and Cu (111) diffraction peaks obtained from the TiN/Cu multilayer films vs. bilayer thickness Λ and (b) the TiN (200) and Cu (111) diffraction peaks obtained from the TiN/Cu nanocomposite films vs. Cu content. All films deposited on Si (100) substrates.

The broadening of the (111) and (200) peaks, expressed by the integral breadth β, was used to calculate the size of the coherently diffracting domains $\langle D \rangle$ in the films [19,20]. The parameter $\langle D \rangle$ corresponds to the average length of crystalline domains in the direction of the diffraction vector and represents the crystalline regions possessing no planar defects [20]. The results in Fig. 2a show that $\langle D \rangle$ of Cu increases from 55 to 200 nm with increasing bilayer thickness, whereas $\langle D \rangle$ for TiN is nearly constant at ~20 nm. In the

case of the TiN/Cu nanocomposite coatings, two Pseudo-Voigt functions, one for TiN (200) and one for Cu (111), were fitted to the overlapping peaks to calculate the domain sizes as shown in the insert in Fig. 1b for the coating with 19 at.% Cu. The results for both domain sizes, TiN (200) and Cu (111), are shown in Fig. 2b. The decrease of the domain size of TiN from 13 to 5 nm confirms a refinement in structure, where on the other hand the Cu domain size increases from 7 to 22 nm with increasing Cu content.

3.2 Mechanical properties and film stresses

Results of the BSTM cycles for multilayer films with different bilayer thickness Λ deposited on Si (100) and measured to a maximum temperature of 650°C are shown in Fig. 3. All films investigated show total tensile stresses in the as-deposited state which is an effect of the high thermal expansion coefficient of the Cu constrained between the TiN layers. The coatings with Λ = 200, 400 and 800 nm show similar tensile stresses of ~140 MPa in the as-deposited state, while they are ~210 MPa for the coating with Λ = 100 nm. This could be attributed to an increased strength of the thinnest Cu layers due to thin film hardening effects [21], and the consequently reduced possibility for stress relaxation. During heating, these tensile stresses decrease because of the higher average thermal expansion coefficient of the film compared to the substrate, and due to stress relaxation as a result of defect annihilation [2,3]. Above a temperature of ~300°C, the curves are reaching a plateau and keep a constant stress level up to the maximum annealing temperature. This might be related to increased plastic deformation in the Cu layers relieving all further stresses which appear in the coating. Significant changes in the slopes during heating dependent on Λ could not be found, indicating that there is no significant difference in the initial porosity of the films contrary the system TiN/Ag [12].

During cooling, the BSTM curves for the coatings with Λ = 400 and 800 nm exhibit a linear thermo-elastic behaviour down to 350°C. Below this temperature, the slope decreases, presumably due to the onset of plastic deformation of the Cu layers under tensile stress. The coatings with Λ = 200 and 100 nm show linear thermo-elastic behaviour down to room temperature. No indication of plastic deformation or the formation of cracks in the coating can be seen. This can presumably be related to hardening effects with decreasing Λ [21], which additionally explains the increasing tensile stresses with decreasing Λ after the annealing experiment.

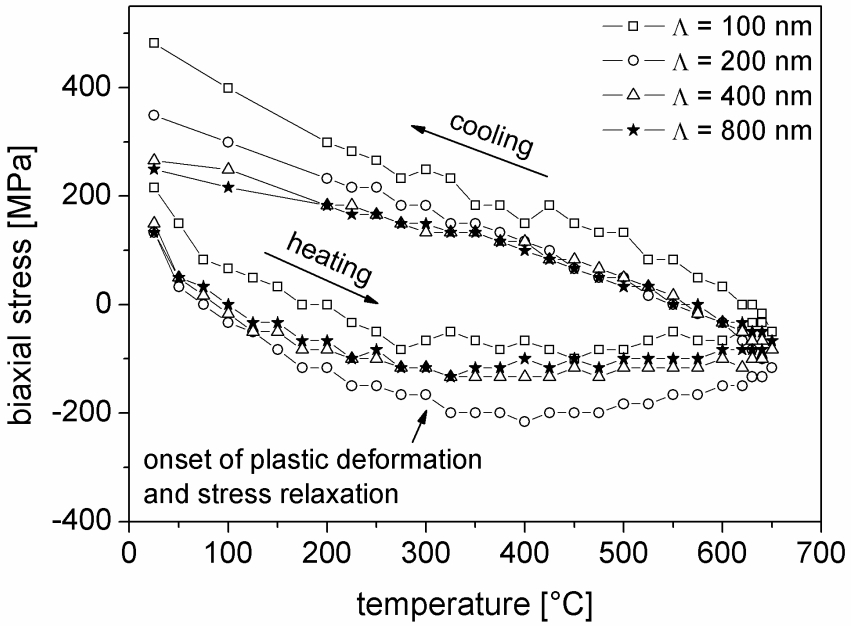

Fig. 3. BSTM cycles from room temperature up to 650°C of TiN/Cu multilayer films with different bilayer thickness Λ grown at 350°C on Si (100) substrates.

Fig. 4 shows BSTM curves for the nanocomposite films with 7, 14, 19 and 28 at.% Cu deposited on Si (100) substrates. All films investigated, except the coating with 14 at.% Cu, show tensile stresses in the as-deposited state which are – as already discussed for the multilayers - a consequence of the high thermal expansion coefficient of Cu. These tensile stresses in the as-deposited state increase with increasing Cu content. In contrast, the coating with 14 at.% Cu shows high compressive stress of ~-750 MPa. This might be related to the increased strength and hardness of a fully percolated nanocomposite structure with TiN nanocrystals of 5-10 nm grain size (see Fig. 2b) surrounded by a thin Cu grain boundary phase, as described by Veprek and Reiprich [22] and Patscheider et al. [23]. The hardness of the nanocomposite coatings show a significant drop between 14 and 19 at.% Cu. For 7 and 14 at.% Cu, relatively high hardness values of 24 and 21 GPa, respectively, were obtained, which might be related to hindered grain boundary sliding due to the fully percolated nanocomposite structure. However, the coating with 19 at.% Cu shows a significantly lower hardness of 10 GPa, where the increasing grain size of the Cu domains as shown in Fig 2b allows grain boundary sliding. The hardness values for Cu contents above 19 at.% are not presented here because of the large scatter due to the high roughness of the coatings. However, it is conceivable that for these high Cu contents the hardness remains in the 10 GPa range or even decreases further with increasing Cu content.

The nanocomposite structure of the coating with 14 at.% Cu is assumed to lead to less stress relieve by plastic deformation during the deposition process and thus, compressive stresses are still present in the as-deposited state. In addition, for coatings with Cu contents of 14 at.% and higher the observed growth correlation between the TiN and the Cu phase may contribute by formation of coherency stresses to the overall stress. However, if the Cu content exceeds a certain value, the stresses are relieved by plastic deformation of the Cu phase, which seems to be valid for the coatings with a Cu content of 19 at.% and higher. Therefore, tensile stresses originating from thermal expansion are dominating in the as-deposited state for high Cu contents.

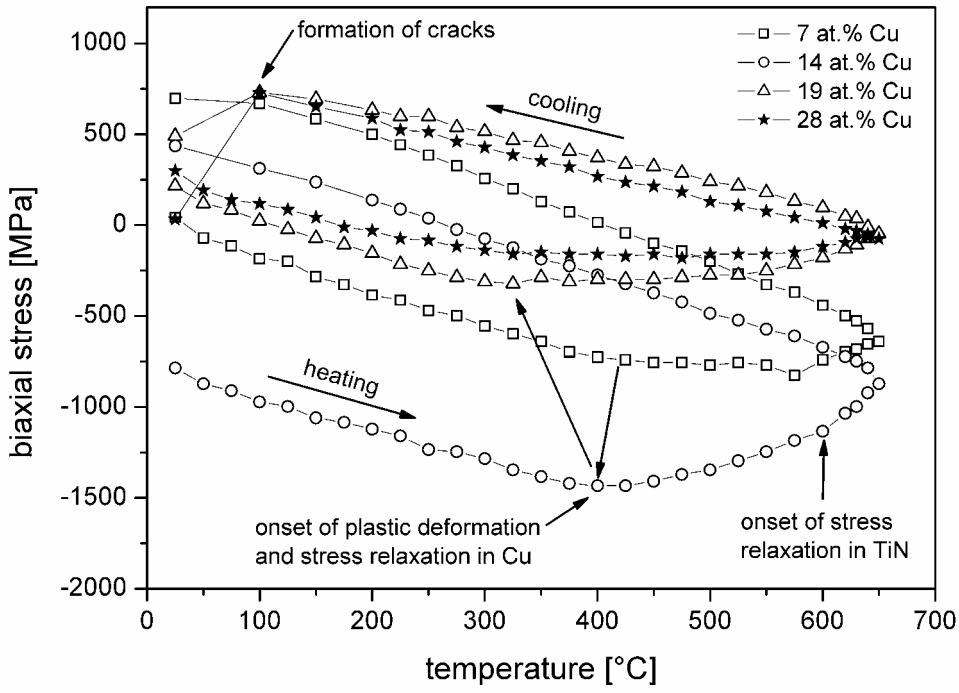

Fig. 4. BSTM cycles from room temperature up to 650°C of TiN/Cu nanocomposite films with different Cu content grown at 350°C on Si (100) substrates.

During heating, the tensile stresses decrease and compressive stresses increase because of the higher average thermal expansion coefficient of the film compared to the substrate. After reaching a certain temperature, the slopes of the BSTM curves decrease, where the amount of the observed changes depends on the Cu content. The coating with 7 at.% Cu shows a plateau in compressive stresses of ~-750 MPa. This plateau may be related to the yield strength of the composite at a given temperature. All further stresses which appear are relived by plastic deformation and stress relaxation in the Cu phase [12]. The compressive stresses of the coating with 14 at.% Cu, which are with -1400 MPa

significantly higher than those of the 7 at.% Cu coating, decrease with increasing temperature above 400°C. This is assumed to be related to the higher driving force for stress relaxation [2] because of the higher stress compared to the 7 at% Cu coating. A further increase in Cu content to values of 19 at.% and higher leads again to a plateau in stresses, like in the case for the coating with 7 at.% Cu. This plateau of low compressive stresses is related to the low strength of the coatings when exceeding a certain Cu content as described above. Consequently, the stress value of the plateau decreases with increasing Cu content as can be seen in Fig. 4. The onset temperature of plastic deformation and stress relaxation in the Cu phase decreases from ~410°C for the coating with 7 at.% Cu to ~400°C for the coating with 14 at.% Cu and to ~330°C for the coatings with high Cu contents as indicated by arrows in Fig. 4. Since the onset temperature decreases with increasing Cu content, the amount of Cu is the determining factor for the onset of stress relaxation and plastic deformation. However, it seems that these onset temperatures are not significantly affected by the significantly higher stresses in the coating with 14 at.% Cu. At ~600°C, a further change in slope of the BSTM curves can be seen which is most pronounced for the coating with 14 at.% Cu. This feature in the BSTM curve is related to the onset of stress relaxation due to defect annihilation in the TiN phase, as could be observed for single-phase TiN films [3]. The films with 24 and 30 at.% Cu show curve shapes and stress levels comparable to the films with 19 and 28 at.% Cu.

During cooling, the BSTM curves show linear thermo-elastic behaviour down to 100°C. The slopes of the cooling segments depend on the Cu content, where the slopes are steeper the lower the Cu content is. These differences are assumed to result from changes in elastic properties and thermal expansion with varying chemical composition. For temperatures below 100°C, the formation of micro-cracks and probably plastic deformation due to high tensile stresses govern the BSTM curves.

5. Conclusions

Within this work, correlations between film structure and stress development during thermal cycling were studied for sputtered TiN/Cu multilayer and nanocomposite films. X-ray diffraction analysis of the multilayer coatings reveals a significant increase in Cu domain size with increasing bilayer periodicity Λ, whereas the domain size of the TiN phase stays constant. In the case of nanocomposite coatings, a dual-phase structure

consisting of TiN and Cu phases forms. The Cu domain size increases with increasing Cu content while the domain size of TiN decreases. Additionally, a change in the preferred growth orientation of TiN for Cu contents between 7 and 14 at.% Cu and indications for a structural correlation between the two phases could be found.

All coatings show total tensile stresses in the as-deposited state which is an effect of the high thermal expansion coefficient of Cu compared to TiN. During annealing of the coatings, compressive stresses increase and reach a plateau due to stress relieve by plastic deformation of the Cu phase. At ~600°C, the onset of stress relaxation in TiN causes a second change in slope of the stress-temperature curve. During cooling, all coatings exhibit linear thermo-elastic behaviour where the slopes are steeper the lower Λ or the Cu content, respectively, is. The onset of plastic deformation and stress relaxation also depends on the Λ and Cu content . In case that a high-strength dual-phase nanocomposite structure is formed, compressive stresses in the as-deposited state occur and no plateau is reached during annealing.

Finally, the results obtained indicate that coating stresses and stress evolution during thermal cycling can be tailored by adding Cu to a TiN hard coating, giving rise to a reduction of thermal stresses due to plastic deformation in the metal phase.

Acknowledgement

This work was financially supported by the Austrian NANO Initiative via a grant from the Austrian Science Fund FWF (project N401-NAN).

References

[1] F. Spaepen, Acta Mater. 48 (2000) 31.

[2] P.H. Mayrhofer, C. Mitterer, L. Hultman, H. Clemens, Progr. Mater. Sci. 51 (2006) 1032.

[3] H. Köstenbauer, G.A. Fontalvo, M. Kapp, J. Keckes, C. Mitterer, Surf. Coat. Technol. 201 (2007) 4777.

[4] J. Musil, P. Zeman, H. Hruby, P.H. Mayrhofer, Surf. Coat. Technol. 120-121 (1999) 179.

[5] J.G. Han, H.S. Myung, H.M. Lee, L.R. Shaginyan, Surf. Coat. Technol. 174-175 (2003) 738.

[6] H.S. Myung, H.M. Lee, L.R. Shaginyan, J.G. Han, Surf. Coat. Technol. 163-164 (2003) 591.

[7] J. Musil, M. Jirout, Surf. Coat. Technol. 201 (2007) 5148.

[8] S. Zhang, D. Sun, Y. Fu, H. Du, Surf. Coat. Technol. 198 (2005) 2.

[9] K. Kutschej, C. Mitterer, C.P.Mulligan, D. Gall, Adv. Eng. Mater. 11 (2006) 1125.

[10] C. Muratore, J.J. Hu, A.A. Voevodin, Thin Solid Films 515 (2007) 3638.

[11] E. Bemporad, M. Sebastiani, C. Pecchio, S. De Rossi, Surf. Coat. Technol 201 (2006) 2155.

[12] H. Köstenbauer, G.A. Fontalvo, J. Keckes, C. Mitterer, Thin Solid Films, 516 (2008) 1920.

[13] H. Köstenbauer, G.A. Fontalvo, C. Mitterer, G. Hlawacek, C. Teichert, J. Keckes, J. Nanosci. Nanotechnol., accepted.

[14] H. Köstenbauer, G.A. Fontalvo, C. Mitterer, J. Keckes, Tribol. Lett. 30 (2008) 53.

[15] P.B. Barna, in L. Eckertová, T. Ruzicka (Eds.), Diagnostics and Applications of Thin Films, Institute of Physics Publishing, Bristol, 1992, p. 295.

[16] Y.Y. Tse, D. Babonneau, A. Michel, G. Abadias, Surf. Coat. Technol. 180-181 (2004) 470.

[17] J.D. Wilcock, D.S. Campbell, Thin Solid Films 3 (1969) 3.

[18] A. Öztürk, K.V. Ezirmik, K. Kazmanli, M. Ürgen, O.L. Eryilmaz, A. Erdemir, Tribol. Int. 41 (2008) 49.

[19] B.E. Warren, X-ray diffraction, Dover Publications, New York, 1990.

[20] R. Delhez, Th.H. de Keijser, E.J. Mittemeijer, Z. Fresenius Anal. Chem. 312 (1982) 1.

[21] E. Arzt, Acta Mater. 46 (1998) 5611.

[22] S. Veprek, S. Reiprich, Thin Solid Films 268 (1995) 64.

[23] J. Patscheider, T. Zehnder, M. Diserens, Surf. Coat. Technol. 146-147 (2001) 201.